SPATIOTEMPORAL DYNAMICS OF A PHOTOREFRACTIVE PHASE-CONJUGATE RESONATOR

by

Daniel R. Korwan

Dissertation submitted to the Faculty of the
Virginia Polytechnic Institute and State University
in partial fulfillment of the requirements for the degree of

DOCTOR OF PHILOSOPHY

in

Physics

APPROVED:

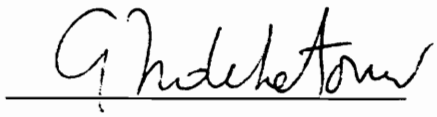

Prof. Guy Indebetouw, Chairman

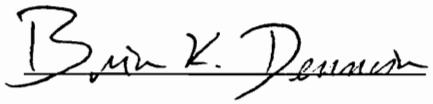

Prof. B. K. Dennison

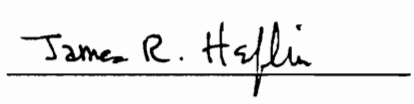

Prof. J. R. Heflin

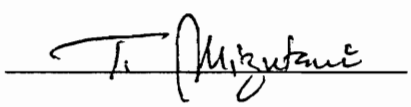

Prof. T. Mizutani

Prof. R. Zallen

April, 1996
Blacksburg, Virginia

Key Words: Photorefractives, Phase-Conjugation, Nonlinear optics

SPATIOTEMPORAL DYNAMICS OF A PHOTOREFRACTIVE PHASE-CONJUGATE RESONATOR

by

Daniel R. Korwan

Committee Chairman: Prof. Guy Indebetouw

Department of Physics

(ABSTRACT)

The spatiotemporal dynamics of a photorefractive phase-conjugate resonator (PPCR) is studied both experimentally and analytically. The resonator is a confocal cavity bounded by a dielectric mirror and a phase-conjugate mirror in a four wave mixing geometry. The effect of the Bragg mismatch, which is caused by the misalignment of the pump fields, is experimentally shown to break the cylindrical symmetry of the system and to increase the speed of the dynamics. By studying the first non stationary state at a cavity Fresnel number of F≈2.0, the effect of the transverse component of the mismatch is shown to add a transverse phase to the wavefront of the phase-conjugate field, leading to the periodic nucleation of a pair of phase defects.

A model of this state is developed in terms of the competition of a few transverse patterns. The model is experimentally verified using a holographic optical correlator designed to identify the modes presumed by the model.

The dynamics are also studied using a Karhunen-Loève decomposition in which the eigenvectors of the covariance matrix are calculated. The covariance matrix is obtained from the transverse intensity fluctuations of the cavity field and the eigenvectors are interpreted as the active cavity modes of the resonator. The results of the application of this experimental method to the F≈2.0 state match those obtained by the correlator. This demonstrates its validity as a useful tool for studying the system. Application of the

decomposition to states at higher F reveal that aperiodic and periodic states can have very similar active mode structures.

An analytical model of the PPCR is then developed using a plane wave decomposition of the cavity field and the material variables contained in Kukhtarev's equations. Numerical simulations using the model demonstrate its accuracy. In addition, the different effects of the longitudinal and transverse components of the Bragg mismatch on the dynamics and defect nucleation are revealed. The relevant assumptions involved in the development of the model are discussed in detail.

Acknowledgements

Well now that this dissertation is nearing completion, it is time to look back with appreciation on all of the people who have made it possible. There are many who have contributed to this work in one form or another, and it is rather odd that only now I find the time to thank them. There are a few who I would especially like to extend my gratitude.

First I want to thank my advisor Dr. Guy Indebetouw who was the single most motivating factor in exploring the many paths that eventually led to this work. He encouraged me to work out my ideas no matter how ridiculous they seemed and provided me with the financial support necessary to do it. I am also very grateful for the special effort he has given me in the actual writing of this work.

I give many thanks to Dr. Brian K. Dennison, Dr. Tetsuro Mizutani, Dr. J. Randy Heflin and Dr. Richard Zallen for not only serving on my thesis committee, but for teaching me physics and providing me with career advice. I would especially like to thank Dr. Heflin for much of my general knowledge of nonlinear optics.

Of course this work would not be possible without all of the somewhat diverse, often peculiar, but always entertaining group of human beings who have floated in out of Blacksburg during my stay here. There are far too many of you to list on a single page, so I will only glorify a special few of your names in print. In no particular order the ones I want to pay tribute to are: Charles Moller for his knowledge of quantum mechanics, Bing Shen for being nugga, Calvin Doss who could always find a way to piss you off, Scott Massie- "red neck makes good", Jerry G. (yeah, yeah, yeah...), and Mark Mattson because the Redskins beat the Cowboys twice last season. As those of you in the know can see, I have indeed left out many.

I also want to thank the National Aeronautics and Space Administration at Langley for a research assistantship and Philip Morris Corp. for a graduate fellowship. Their financial support has led to the research presented in this dissertation, in four technical publications and at two conferences.

Finally, and most of all, I thank Dr. Sharon W. Flinder for everything she has ever meant and will mean to me.

Daniel R. Korwan

April 10, 1996

Table of Contents

List of Figures

Chapter 1

Introduction

1.1 Transverse nonlinear optics: overview

The nonlinear interaction of light with matter is a process in which light alters the properties of the medium in which it travels and as a consequence the properties of the light change. The field of nonlinear optics is the study of the many different effects that can occur in such processes. The origins of this field can be traced back to 1960 with the invention of the ruby laser [1] which produced intense, coherent, and monochromatic light, necessities for the observation of most nonlinear phenomena. Although the laser is inherently a nonlinear device, the experimental demonstration of second harmonic generation in 1961 [2], in which light at a certain frequency is converted into light at twice the original frequency, is considered the first nonlinear optical experiment. At approximately the same time, other nonlinear processes such as two photon absorption were successfully demonstrated [3] and theoretical formalisms soon followed [4,5].

Many of these early experiments were understood solely on the basis of easily understandable models that included only the variation of the light's field distribution along the direction of propagation. However, as early as 1963 the operation of lasers was shown to spontaneously produce complicated spatially and temporally varying patterns [6,7], but these patterns were considered too difficult to explain or control. In fact these effects were (and generally still are) considered to be undesirable and were therefore suppressed by placing apertures inside the resonant cavity of the laser thereby limiting the transverse spatial content of the field to a single Guassian profile.

It was some years before attempts were made to exploit any transverse nonlinear effects for useful purposes. For example, soliton propagation and self focusing and trapping of optical beams were studied as early as the early 1970's [8,9], but are only now being recognized as having useful applications.

Today the field of transverse nonlinear optics has grown enormous, partly due to the interest in the nonlinear dynamics and pattern formation in all physical systems [10,11] and partly due to the potential for tailoring transverse effects toward a variety of practical applications. In 1975 Haken showed the analogy between the Lorenz equations describing Benard convection in fluids and the equations describing the single mode laser [12], and in 1983 chaos in a laser was experimentally verified [13]. Thus the connection between other nonlinear physical systems and nonlinear optical systems was established. The importance of this lies in the relative ease in which optical systems can be studied, which is in direct contrast to turbulent fluid flows for example. Measurements of the intensity of optical systems can be easily performed and in a well controlled environment. Soon many fully three dimensional studies of a variety of nonlinear optical systems were conducted and the field of nonlinear transverse optics established. On the other hand, practical applications, although generally in their early stages, have been proposed in fields such as optical storage, optical switching, optical processing, associative recall, and beam guiding [14-17].

1.2 The photorefractive effect

In the mid to late 1960's a particular nonlinear process was observed that later became known as the photorefractive effect [18]. The earliest observations were in $LiNbO_3$ and $LiTaO_3$ crystals and were thought to be deleterious to the operation of some

nonlinear devices [19-21]. Soon however, attempts were made to put the effect to use in image processing and storage [22]. This occurred because the photorefractive effect is a physical mechanism whereby real time refractive index variations or holograms [23] can be written into ferroelectric crystals using only low intensity cw lasers. Until this became known, similar effects using the relatively small third order optical susceptibility could only be realized using high intensity pulsed lasers.

Concurrent to new developments that were occurring toward the exploitation of the effect, several theoretical formulations were being proposed. The models derived by Feinberg [24] and Kukhtarev [25] have proven to accurately describe the complexities of the interaction, although Kukhtarev's transport model is predominately used in most work today. The physical mechanism described by both models is essentially the same. Light interacts with the photorefractive medium and causes charge carriers to migrate so that an electric field is created by the charge separation. This space charge field then modifies the refractive index of the medium via the linear electrooptic effect (Pockel's effect). In the next section the effect will be formally derived for the case of two wave mixing using Kukhtarev's equations. Then its relationship to four wave mixing and phase conjugation will be described.

1.2.1 Two wave mixing

The photorefractive effect is most easily understood in terms of photorefractive two mode coupling. A detailed analysis of the photorefractive effect is presented in reference [26] and a detailed analysis of wave coupling in thick gratings is presented in reference [27]. As shown in figure 1.1 the process starts with the interference of two coherent light waves inside the photorefractive medium. Although waves of different

frequencies may be used, the waves considered here have the same frequency so that a stationary interference pattern develops. In regions of high intensity, charge carriers (represented by electrons here) are excited out of occupied donor sites into the conduction band. These charges will then tend to migrate to regions of low intensity via diffusion, drift in an applied electric field, or the photovoltaic effect and will once again be trapped by unoccupied donor sites. The excitation and retrapping of charges will continue so that in the steady state, regions of high intensity gain a net positive charge while regions of low intensity gain a net negative charge. This oscillatory charge distribution creates what is commonly referred to as a space charge field. The space charge field then interacts with the medium via the electrooptic effect in order to modify its refractive index. Since the refractive index variation follows the variation of the space charge field, a refractive index grating is formed. Once the grating has formed the light waves may exchange energy and/or phase depending on the process responsible for charge migration. It has been shown that in diffusion dominated materials (e.g. $BaTiO_3$, used in this work) the refractive index grating is shifted by a quarter period from the interference pattern. The size of this shift maximizes the energy transfer between the two waves and minimizes the phase transfer.

A theoretical analysis describing the interaction of the fields with the medium starts with the source free Maxwell's equations,

$$\nabla \times \vec{H} = \frac{\partial \vec{D}}{\partial t}$$

$$\nabla \times \vec{E} = -\frac{\partial \vec{B}}{\partial t} = -\mu_0 \frac{\partial \vec{H}}{\partial t}$$

$$\nabla \cdot \vec{D} = 0$$

$$\nabla \cdot \vec{B} = 0, \qquad (1.1)$$

where $\vec{H}$, $\vec{B}$, $\vec{D}$, and $\vec{E}$ are the magnetic field, magnetic flux density (displacement), electric displacement, and electric field respectively. Typically $\vec{B} = \mu_0 \vec{H}$ at optical frequencies and $\vec{D} = \varepsilon_0 \vec{E} + \vec{P}$, where μ_0, ε_0, and $\vec{P}$ are the magnetic permeability of vacuum, the electric permittivity of vacuum and the electric polarization respectively. In order to describe second order nonlinear effects, the polarization is expanded up to second order in the applied electric field so that [28],

$$D_i = \varepsilon_0 \sum_j \left[\delta_{ij} + \chi_{ij} + \sum_k \chi_{ijk} E_k \right] E_j . \tag{1.2}$$

The first two terms in this expansion represent the linear refractive index of the medium and the third term is responsible for the linear electrooptic effect and sum/difference-frequency generation. In the case of the linear electrooptic effect where $E_k(\omega = 0)$ is a static applied electric field, the second order nonlinear susceptibility is conventionally expressed in terms of the electrooptic tensor. This tensor describes the change of the index ellipsoid of the medium due to the presence of the applied field. Therefore eq. 1.2 can be rewritten in the form

$$\vec{D} = \varepsilon_0 \vec{\varepsilon} \cdot \vec{E} - \varepsilon_0 \vec{\varepsilon} \cdot (\vec{R} \cdot \vec{E}_a) \cdot (\vec{\varepsilon} \cdot \vec{E}), \tag{1.3}$$

where $\vec{R}$ is the electrooptic tensor, $\vec{E}_a$ is the applied field, and $\vec{\varepsilon}$ is the permittivity tensor of the medium. In the case of the photorefractive effect, $\vec{E}_a$ is considered to be the space charge field plus possibly an additional externally applied field, which in our case we set equal to zero. It should be noted that the nonlinearity arising in this case comes from the fact that the space charge field is ultimately created by the optical fields propagating in the medium.

Using Maxwell's equations we obtain the nonlinear wave equation in the standard way [22]

$$\nabla^2\vec{E} - \mu_0 \frac{\partial^2 \vec{D}}{\partial t^2} = 0. \tag{1.4}$$

To see how the fields propagate we take the total electric field in the medium to be the sum of the propagating fields,

$$\vec{E}(\vec{r},t) = \tfrac{1}{2}\left(\hat{e}_1 E_1(\vec{r},t)e^{i\vec{k}_1\cdot\vec{r}} + \hat{e}_2 E_2(\vec{r},t)e^{i\vec{k}_2\cdot\vec{r}}\right)e^{-i\omega t} + \text{c.c.}, \tag{1.5}$$

and the space charge field as

$$E_a(\vec{r},t) = \tfrac{1}{2}\hat{k}_g E_{sc}(\vec{r},t)e^{i\vec{k}_g\cdot\vec{r}} + \text{c.c.}, \tag{1.6}$$

where c.c. stands for the complex conjugates of the preceding terms. E_{sc}, E_1, and E_2 are slowly varying functions of space and time, and since the space charge field variation follows the interference pattern of the optical fields, its wave vector is chosen to take the form $\vec{k}_g = \vec{k}_1 - \vec{k}_2$. Assuming the incident fields are eigenmodes of the medium (i.e. $\vec{\vec{\varepsilon}}$) and that the grating produces only a small change in the refractive index, substitution of eqs. 1.5 and 1.6 into eq. 1.4 yields the following coupled differential equations,

$$\hat{k}_1 \cdot \nabla E_1 + \frac{i\omega}{2n_1 c}\hat{e}_1^* \cdot \vec{\vec{\varepsilon}}(\vec{\vec{R}}\cdot\hat{k}_g)\cdot\vec{\vec{\varepsilon}}\cdot\hat{e}_2 E_{sc}^* E_2 = 0$$

$$\hat{k}_2 \cdot \nabla E_2 + \frac{i\omega}{2n_2 c}\hat{e}_2^* \cdot \vec{\vec{\varepsilon}}(\vec{\vec{R}}\cdot\hat{k}_g)\cdot\vec{\vec{\varepsilon}}\cdot\hat{e}_1 E_{sc} E_1 = 0, \tag{1.7}$$

where n_1 and n_2 are the average refractive indices seen by each field. The derivation of eq. 1.7 involves a large amount of algebra and is not shown here. The general procedure is to separate the equation by equating terms with the same exponent (i.e. phase matching) and then performing an inner product on each using the appropriate polarization vector. Use has been made of the slowly varying envelope approximation. The adiabatic approximation is also used in which the temporal derivatives are ignored. The exact expression of E_{sc} will be formally derived in the next section and the adiabatic approximation will be further elucidated.

The physical interpretation of the preceding derivation becomes more transparent when the nonlinearity is considered as simply a refractive index change and the propagating fields do not change polarization states. In this case the wave equation is written

$$\nabla^2 E(\vec{r},t) - (\varepsilon_0 \mu_0 n_b^2 + 2\varepsilon_0 \mu_0 n_b \Delta n(\vec{r},t)) \frac{\partial^2 E(\vec{r},t)}{\partial t^2} = 0, \tag{1.8}$$

where n_b is the average refractive index acting on the fields and $\Delta n(\vec{r},t)$ represents the change of the index due to the nonlinearity.

Let each of the fields be plane waves with the same polarization so that the total field now takes the form

$$E(\vec{r},t) = \tfrac{1}{2}\left(A_1(z,t)e^{i\vec{k}_1\cdot\vec{r}} + A_2(z,t)e^{i\vec{k}_2\cdot\vec{r}}\right)e^{-i\omega t} + c.c., \tag{1.9}$$

and the change in the refractive index takes the form

$$\Delta n(\vec{r},t) = \tfrac{1}{2}\eta(z,t)e^{i\vec{k}_g\cdot\vec{r}} + c.c., \tag{1.10}$$

where A_1, A_2 and η are slowly varying functions in time and along the general direction of propagation, which is chosen as the z direction. This choice for the field amplitudes imposes that the interaction occurs primarily along the direction of propagation. Performing a similar derivation as before, we obtain the simpler form of equations 1.7,

$$\cos\theta_1 \frac{\partial A_1(z,t)}{\partial z} - \frac{i\omega}{2c}\eta^*(z,t)A_2(z,t) = 0$$

$$\cos\theta_2 \frac{\partial A_2(z,t)}{\partial z} - \frac{i\omega}{2c}\eta(z,t)A_1(z,t) = 0, \tag{1.11}$$

where θ_1 and θ_2 are the angles that the fields make with the z axis. The change in refractive index may now be related back to the second terms in eq. 1.7 by remembering that the change in the index ellipsoid due to the electrooptic effect can be written

$$r_{eff}E_a = \Delta\left(\frac{1}{n_b^2}\right) \approx \frac{-2\Delta n}{n_b^3},$$

or after some rearrangement

$$\eta(z,t) = \frac{n_b^3 r_{eff} E_{sc}(z,t)}{2}, \tag{1.12}$$

where the amplitude of the space charge field is now also assumed to slowly vary only in the z direction as prescribed by the choice of the fields in equation 1.9. r_{eff} is called the "effective electrooptic coefficient" and must be obtained from vectorial analysis of the electro-optic tensor. Comparison of eqs. 1.7, 1.11 and 1.12 shows that the effective electrooptic coefficient is given by

$$r_{eff}^{i} = \frac{1}{n_i^4}\hat{e}_i^* \cdot \vec{\varepsilon}(\vec{R}\cdot\hat{k}_g)\cdot\vec{\varepsilon}\cdot\hat{e}_j, \tag{1.13}$$

where the i and j indices denote the two different fields.

The relatively simple equations 1.11-1.12 are now all that is necessary to describe the propagation of the fields involved in two wave mixing interactions in photorefractive media, provided one remembers that the amplitude of the index grating must now be obtained using r_{eff}, as given by equation 1.13, and E_{sc}. A derivation of E_{sc} in terms of the properties of the specific photorefractive medium is given in the next section.

1.2.2 Kukhtarev's equations

As previously alluded to, the photorefractive process starts when spatially non uniform light illuminates a photorefractive medium. Charge carriers are excited from donor sites into the conduction band. The mobile charges can then migrate in the medium due to an externally applied field, diffusion, or the photovoltaic effect and get re-

trapped at unoccupied donor sites. Since the light is non uniform, the probability for re-exciting trapped charges in regions of relative dark intensity is not as high as in regions of bright intensity and a non uniform distribution of charges will develop. The spatial imbalance of charges creates a spatially modulated electric field and since the medium is electrooptic, there will be a corresponding modulation in its refractive index.

This process is described by Kukhtarev's transport equations [25], which relates the charge excitation and retrapping mechanisms to the migration of the charges. The ultimate goal of these equations is to derive an expression for the space charge field E_{sc} in terms of the physical parameters of the medium, so that the field equations, 1.7 or 1.11, provide a complete description of the photorefractive effect. The derivation presented here assumes that the charge carriers are electrons although they can be any combination of electrons or holes.

The four equations are given by the following and described below:

$$\vec{J}(\vec{r},t) = e\mu n(\vec{r},t)\vec{E}_a(\vec{r},t) + K_B T\mu \nabla n(\vec{r},t), \tag{1.14}$$

$$\frac{\partial N_D^+(\vec{r},t)}{\partial t} = (\beta + SI(\vec{r},t))(N_D - N_D^+(\vec{r},t)) - \gamma_R n(\vec{r},t) N_D^+(\vec{r},t), \tag{1.15}$$

$$\nabla \cdot (\vec{E}_a(\vec{r},t)) = -\frac{e}{\varepsilon_0 \varepsilon}(n(\vec{r},t) + N_A - N_D^+(\vec{r},t)), \tag{1.16}$$

$$e\frac{\partial N_D^+(\vec{r},t)}{\partial t} = e\frac{\partial n(\vec{r},t)}{\partial t} - \nabla \cdot \vec{J}(\vec{r},t), \tag{1.17}$$

Equation 1.14 describes the current density $\vec{J}$ in the crystal that arises due to the mobile charge carriers with density n. The first term in the right hand side represents drift in an applied electric field $\vec{E}_a$ and the second term diffusion. The anisotropic photovoltaic term is ignored since it is negligible in our medium, $BaTiO_3$ [29]. Equation 1.15 is the rate equation and it describes the excitations of the charges. N_D is the total number density of

donor sites, $N_D^+(\vec{r},t)$ is the number density of ionized donors, and $n(\vec{r},t)$ is the number density of charge carriers. The first term on the right hand side describes the optical and thermal ionization rates and the second term describes the recombination rate. The thermal rate is very small compared to the ionization rate at the optical intensities used in this work and is henceforth ignored. Equation 1.16 and 1.17 are the Poisson equation and the continuity equation respectively. N_A is the total number density of acceptor sites, which ensures that there are a large number of unoccupied donor sites. The constants are given by:

β = thermal generation rate (β<<SI for our intensities),

γ_R = recombination coefficient,

-e = electron charge,

μ = electron mobility,

T = temperature,

K_B = Boltzmann's constant,

ε = unperturbed dielectric constant,

S = photoionization cross-section.

Equations 1.14-1.16 are difficult to reduce to a single expression for the evolution of the space charge field due to the products of the dependent variables. Kukhtarev used a perturbative approach to solve them where each of the variables is expanded into a Fourier series using the wave vector of the grating. The zero order terms of the equation are spatial and temporal averages of the variables and the higher order terms are assumed to represent increasingly small modulations of these averages. When the series are inserted into the equations, terms that are the products of these small modulations can then be neglected thereby linearizing the equations. The solution proceeds as follows.

First the variables are expanded in series:

$$I(\vec{r},t) = I_0 + \tfrac{1}{2}\{I_1(z,t)e^{i\vec{k}_g\cdot\vec{r}} + c.c.\}$$

$$n(\vec{r},t) = n_0 + \tfrac{1}{2}\{n_1(z,t)e^{i\vec{k}_g\cdot\vec{r}} + c.c.\}$$

$$N_D^+(\vec{r},t) = N_{D0}^+ + \tfrac{1}{2}\{N_{D1}^+(z,t)e^{i\vec{k}_g\cdot\vec{r}} + c.c.\}$$

$$E_a(\vec{r},t) = E_0 + \tfrac{1}{2}\{E_{sc}(z,t)e^{i\vec{k}_g\cdot\vec{r}} + c.c.\}, \qquad (1.18)$$

where I_0, n_0 and N_{D0}^+ are the spatial and temporal averages of the variables and E_0 is an externally applied field which is equal to zero in all cases considered in this work. Second and higher order terms are ignored under the assumption that they are increasingly small and will therefore have little effect on the solution. Similar to equation 1.9, the small first order coefficients are considered to slowly vary only along the direction of the propagation of the fields and in time with the majority of the total first order spatial variation in the direction of the grating vector. $E_{sc}(z,t)$ is the resulting space charge field due to the charge separation and $I_1(z,t) = A_1(z,t)A_2^*(z,t)$ is a term produced by the interference of the fields. I_1 must be much smaller than the average intensity, $I_0(z,t) = A_1(z,t)A_1^*(z,t) + A_2(z,t)A_2^*(z,t)$, in order for the above assumptions to be accurate.

Substituting equations 1.18 into equations 1.14-1.17, neglecting terms that are second order in the perturbation amplitudes, using the slowly varying envelope approximation, and making use of the fact that terms similar to $\hat{z}\cdot\hat{k}_g\frac{\partial E_{sc}}{\partial z}$ are small, we obtain,

$$n_0 = \frac{SI_0(N_D - N_{D0}^+)}{\gamma_R N_{D0}^+}$$

$$N_{D0}^+ + n_0 - N_A = 0$$

$$\frac{\partial n_1}{\partial t} = \frac{\partial N_{D1}^+}{\partial t} + \mu n_0 i k_g E_{sc} - \frac{\mu K_B T}{e} k_g^2 n_1$$

$$\frac{\partial N_{DI}^{+}}{\partial t} = SI_I(N_D - N_{D0}^{+}) - SI_0 N_{DI}^{+} - \gamma_R n_0 N_{DI}^{+} - \gamma_R N_{D0}^{+} n_I$$

$$ik_g E_{sc} = \frac{-e}{\varepsilon_0 \varepsilon}(n_I - N_{DI}^{+}), \qquad (1.19)$$

The first two terms in equation 1.19 are obtained by equating the zero order coefficients in the expansion and the last three terms are obtained by equating the first order coefficients.

Manipulating these expressions in order to get a single equation for the space charge field yields

$$\frac{\partial^2 E_{sc}}{\partial t^2} + \frac{\partial E_{sc}}{\partial t}\left[\frac{1}{\tau_{die}} + \frac{1}{\tau_D} + \frac{1}{\tau_{Re}} + \frac{1}{\tau_{Ie}}\right] + E_{sc}\left[\frac{1}{\tau_{Re}\tau_{die}} + \frac{1}{\tau_{Ie}}\left(\frac{1}{\tau_D} + \frac{1}{\tau_{die}}\right)\right] = \frac{ieS(N_A - N_D)I_I}{\tau_D k_g \varepsilon_0 \varepsilon}, \qquad (1.20)$$

where the characteristic time scales of the medium and their orders of magnitude in typical inorganic photorefractive materials are,

$$\tau_{die} = \text{ dielectric relaxation time } \equiv \frac{\varepsilon_0 \varepsilon}{e\mu n_0} \approx 10^{-3}\text{s}$$

$$\tau_{Re} = \text{ electron recombination time } \equiv (\gamma N_A)^{-1} \approx 10^{-9}\text{s}$$

$$\tau_D = \text{ diffusion time } \equiv \frac{e}{k_g^2 K_B T \mu} \approx 10^{-9}\text{s}$$

$$\tau_{Ie} = \text{ production + ion-recombination times } \equiv (SI_0 + \gamma n_0)^{-1} \approx 10^{-3}\text{s}. \qquad (1.21)$$

Equation 1.20 may be reduced further by making use of the size of the relative time scales, noting again that E_{sc} varies slowly in time, and that in $BaTiO_3$ $N_D \approx 10^{19}\text{cm}^{-1} >> N_A \approx 10^{16}\text{cm}^{-1} >> n_0 \approx 10^{13}\text{cm}^{-1}$. The final expression for the space charge field is then approximately given by

$$\frac{\partial E_{sc}(z,t)}{\partial t}\tau + E_{sc}(z,t) = -i\frac{I_1(z,t)}{I_0(z,t)}\frac{E_D}{1+E_D/E_Q}, \tag{1.22}$$

where the characteristic time scale of the photorefractive process is

$$\tau = \tau_{die}\left[\frac{1+\tau_{Re}/\tau_D}{1+E_D/E_Q}\right], \tag{1.23}$$

and the characteristic fields are

$$E_D = \frac{k_g K_B T}{e}$$

$$E_Q = \frac{eN_A}{\varepsilon_0 \varepsilon k_g}. \tag{1.24}$$

E_Q is the value of the space charge field for maximum charge separation equal to the period of the intensity and E_D is the diffusion field.

τ is typically on the order of seconds for $BaTiO_3$ and for intensities on the order of $4W/cm^2$. This means that the build up and erasure time of the index grating is much slower than the transit time of the fields in the medium. This allows one to drop temporal derivatives in the field equations (equations 1.7 or 1.11) because the field is assumed to instantaneously follow the temporal change in the grating, an approximation referred to earlier as the adiabatic approximation.

1.2.3 Phase conjugation and four wave mixing

Phase conjugation is a process in which a traveling wave is acted upon in such a way as to produce a time reversed replica of the original wave. In other words if an image bearing optical field traveling along the z axis has the form $E_1(\vec{r},t) = \frac{1}{2}A_1(\vec{r},t)e^{i(kz-\varpi t)} + c.c.$, then its phase conjugate replica will have the form

$E_{pc}(\vec{r},t) = \frac{1}{2}A_1^*(\vec{r},t)e^{i(-kz-\varpi t)} + c.c..$ A very important direct consequence of phase conjugation is the process known as phase healing or image restoration. As demonstrated in figure 1.2 a distorted image can be recovered by using the phase conjugate wave of the image and passing it once more through the distortion. This will become important in the next section when phase conjugate resonators are discussed.

Phase conjugate waves can be produced using different processes. Phase conjugation by stimulated Brillouin scattering in which the phase conjugate wave is produced by a traveling acoustic wave via the electrostrictive effect, was first demonstrated in 1972 [30]. Yariv and Pepper [31] in 1977 showed how phase conjugation could be achieved using four wave mixing in third order media, and in 1979 Huignard [32] demonstrated it using four wave mixing in a photorefractive medium.

Photorefractive four wave mixing is an interaction between four fields that occurs in much the same manner as the two wave mixing process just described. The general interaction is shown in figure 1.3 and is viewed in the following way. Two fields interfere to form a refractive index grating and one of the other two will then scatter off the grating into the direction of the fourth. The process is symmetric in that if fields 1 and 4 in figure 1.3 form a grating on which 2 and 3 will scatter then the opposite is also true. The actual transfer of energy between the fields is dependent on the material parameters.

The configuration shown in figure 1.3 is called the transmission grating geometry, although other configurations are possible. In the reflection geometry for example, the grating is formed by the interference of 1 and 3 (or 2 and 4). These different configurations can be suppressed by an appropriate choice of the geometry used in a particular medium or by the preferential enhancement of one grating by the application of an external electric field.

Phase conjugation comes about in this interaction because the Bragg condition must be satisfied. The Bragg condition is a result of conservation of momentum, which requires that field 1 (3) must counter propagate with respect to field 2 (4). Typically in experiments, only three fields are initially present. For figure 1.3 this would correspond to two relatively intense pump fields (1 and 2) and a weaker probe field (4). The process then spontaneously produces a signal field (3), which is the exact phase conjugate of 4 due to the Bragg condition.

1.3 Photorefractive phase-conjugate resonator (PPCR)

In general, optical resonators are devices which contain an amplifying medium and an optical cavity to provide feedback into the medium. The cavity is arranged in either a closed loop or bounded linear configuration. Energy is transferred to the medium causing electronic excitations that relax and emit radiation. The cavity is tuned so that its resonant conditions are satisfied by the emitted radiation and coherent oscillation builds up.

Photorefractive phase-conjugate resonators (PPCR) are a particular class of optical resonators where a cavity mirror is replaced by a phase conjugate mirror (PCM) in a photorefractive four wave mixing geometry. The advantages of such a device will be explained in the next section. The first use of a PPCR was to correct distortions in a laser cavity [33]. In that work the PCM was used as a passive device, which means that energy was transferred to the cavity by exciting a lasing medium that in turn excites the four wave mixing process in the PCM.

In this work, an active PPCR is studied in which not only does the PCM act as a phase conjugator, but is also used as the amplifying medium. The resonator, as shown in

figure 1.4, is bounded by a photorefractive phase conjugate mirror and a dielectric mirror. A lens is place in the center of the cavity at a distance of one focal length from each mirror. Circular apertures are placed next to each mirror in order to control the transverse size of the oscillating cavity field. This particular choice of cavity geometry is chosen for its relative simplicity and facility in which the transverse confinement of the cavity can be controlled. The PCM is optically pumped using the 514nm line of an argon ion laser which is isolated from the cavity by a Faraday rotator. The pumps have extraordinary polarization in order to make use of the large electrooptic coefficient of $BaTiO_3$. Each pump has a power of 35mW with a beam diameter at the crystal of about 3mm. The focal length of the lens is 16cm and the planar cavity mirror is 95% reflecting with a dielectric coating. The pump field 1 and cavity field (3 and 4) make an angle of 53° and 13° with respect to the normal of the crystal face (crystal axis).

1.3.1 Control parameters

When the pumps are strong enough to overcome the cavity losses (i.e. the threshold condition), oscillation will build up in the cavity due to the feedback produced by the dielectric mirror. In this situation the four wave mixing process in the crystal may be viewed in relation to figure 1.2 by considering the pump fields as equivalent to fields 1 and 2, and the cavity fields as equivalent to fields 3 and 4.

Above threshold the oscillating field has been shown to exhibit interesting spatiotemporal dynamics in the plane transverse to the cavity axis [34-36]. In general, the dynamics of the transverse patterns is characterized by the motion of "phase defects" or phase singularities in the optical field. The number of these vortices, as they are also

called, varies and their motion can be periodic, quasiperiodic, and chaotic depending on the two control parameters of the system.

The first control parameter is the cavity Fresnel number defined by $F=D_1D_2/\lambda f$, where $D_{1,2}$ are the diameters of the apertures placed in the cavity, λ is the laser wavelength, and f is the focal length of the intracavity lens (see fig. 1.4). The Fresnel number is a measure of the amount of transverse confinement of the cavity. It may also be viewed as the number of Fresnel zones or speckles diffracted by one aperture and enclosed by the other. In this sense one can think about it in terms of the amount of transverse spatial information the cavity can support.

There seems to be two ranges of Fresnel numbers leading to different types of behaviors [37]. At modest Fresnel numbers ($F \leq 10$) the cavity boundaries control the transverse length scales and thus the spatial complexity of the cavity field. This is a domain of interest for engineering applications since it may be possible to achieve pattern selection or switching by manipulation of the cavity boundary conditions. At higher Fresnel numbers, material diffusion may determine the dominant length scale and other scalings prevail.

While the Fresnel number is related purely to the geometry of the cavity, the other control parameter is related to the four wave mixing process and is termed the Bragg mismatch. It is a measure of the departure from the Bragg condition and is produced by an angular tilt or mismatch between the normally counterpropagating pump fields, as shown in figure 1.5. Generally, a relatively large mismatch will destroy the four wave mixing process since destructive interference will inhibit the formation of the phase conjugate field. However, for small values of the mismatch the phase-conjugate reflectivity, defined as the ratio of the amplitude of the signal field to that of the probe field, has been shown to increase with respect to a process where there is no mismatch

[38]. Chaotic oscillations have been observed in the phase-conjugate field for small particular values of the mismatch [39]. The study of the effect of the Bragg mismatch on the dynamics of the system and how it relates to the feedback from the cavity and the cavity geometry is one primary concern of this work.

1.4 Motivation

There are two separate motivating factors for the study of a PPCR. By taking advantage of its inherent gain, phase healing, and feedback mechanisms it may be possible to use it to implement novel image processing and storage schemes. Other work using nonlinear optical resonators in storage and processing applications has already exploited these properties to some extent [40,41,16,17]. Until now however, the PPCR is not fully understood in terms of the physical mechanisms that drive the dynamics. Therefore a full characterization of the dynamics of the system and the development of a satisfactory physical model of it are the necessary preliminary steps leading to its control and possible practical utilization.

This work is also driven by the fact that the PPCR is an ideal system for studying the more fundamental aspects of transverse nonlinear phenomena. So far, most experimental work in continuous (as opposed to arrays for example) spatiotemporal dynamical systems has been done on fluid flows and, in optics, lasers. However, comparison between theoretical predictions and experimental observations on laser systems has proven to be difficult due to their high speed dynamics [42,43]. In PPCRs, dynamics similar to those observed in other optical oscillators such as lasers are also observed, however they occur on a much slower time scale. This occurs despite the

different gain mechanisms involved and therefore the question of the universality of the dynamical phenomena in all spatially extended optical systems is of interest.

The slow speed of the dynamics then becomes important because it allows the system to be conveniently studied using existing hardware (e.g. CCD arrays). Therefore intensive experimental studies may be performed on this system and, assuming the universality of the phenomena is true, the results can be used to understand the faster systems. At the very least this system can be used to test the effectiveness of new experimental techniques used in the study of transverse nonlinear optical phenomena. With the assumption that it is difficult and more cost intensive to implement studies of the fast systems (e.g. the need for high speed detectors), it would be beneficial to test new studies first on the PPCR and then modify them for the faster systems.

Consequently, the aim of this work is two fold. First, we will demonstrate the validity of novel experimental techniques used to study spatiotemporal optical systems by applying them to the PPCR. Second, using the knowledge gained from this application, we will ultimately develop an analytical model that accurately depicts the observed dynamics.

1.5 Organization of dissertation

The dissertation is divide into three main sections. The first is presented in chapter two in which a model of the PPCR is formulated for the simplest non stationary state observed. The model assumes that the cavity field can be decomposed into a few cylindrically symmetric Gauss-Laguerre patterns that compete for the gain (i.e. energy transfer from the pumps) in the crystal. The model is studied using time series data as a function of the Bragg mismatch, and by using a holographic correlation technique. The

correlator optically measures the correlation between the Gauss Laguerre patterns and the cavity field. The results of the correlator will demonstrate that simple mode competition is an accurate model for this state despite the arbitrary assumption about the form of the modes. The drawbacks of this technique will be discussed in terms of its implementation to more complicated dynamical states.

In chapter three another experimental technique is presented: the Karhunen-Loève decomposition. The decomposition can greatly reduce the apparent uncharacterizable complexities of the spatiotemporal dynamics of the resonator by representing it as the temporal oscillations of a simplified set of spatial patterns. This is accomplished without resorting to the use of any particular physical knowledge of the photorefractive process or by making any arbitrary assumptions about the nature of the resonant modes. The decomposition is performed by taking discreet samples of the transverse cavity field in time and space by using a CCD array, and then processing this data using the Karhunen-Loève algorithm on a PC. Results of the application of the decomposition on the PPCR to the first non stationary state agree well with the results of the correlator. At higher Fresnel numbers, it reveals, among other things, that the symmetry of the characteristic patterns is inversely proportional to the Bragg mismatch. At the same time the temporal complexity of the oscillations of these patterns increases with the mismatch. Examples of these patterns and their oscillations at different values of the mismatch and Fresnel number are analyzed.

The third part of the dissertation includes an analytical model based on a plane wave decomposition of the wave equation and Kukhtarev's equation, which is derived in chapter four. With the inclusion of the vector Bragg mismatch, this is the first analytical model that accurately represents the dynamics at low Fresnel number. Relevant assumptions used in the derivation are discussed and the crucial roles played by the

transverse mismatch and the longitudinal mismatch is presented. For instance, the transverse component of the mismatch combined with the cavity geometry is shown to destabilize the stationary states, while the longitudinal component of the mismatch is responsible for aperiodic states.

In the final chapter an overall conclusion of the work is presented. Directions for possible future investigations are given.

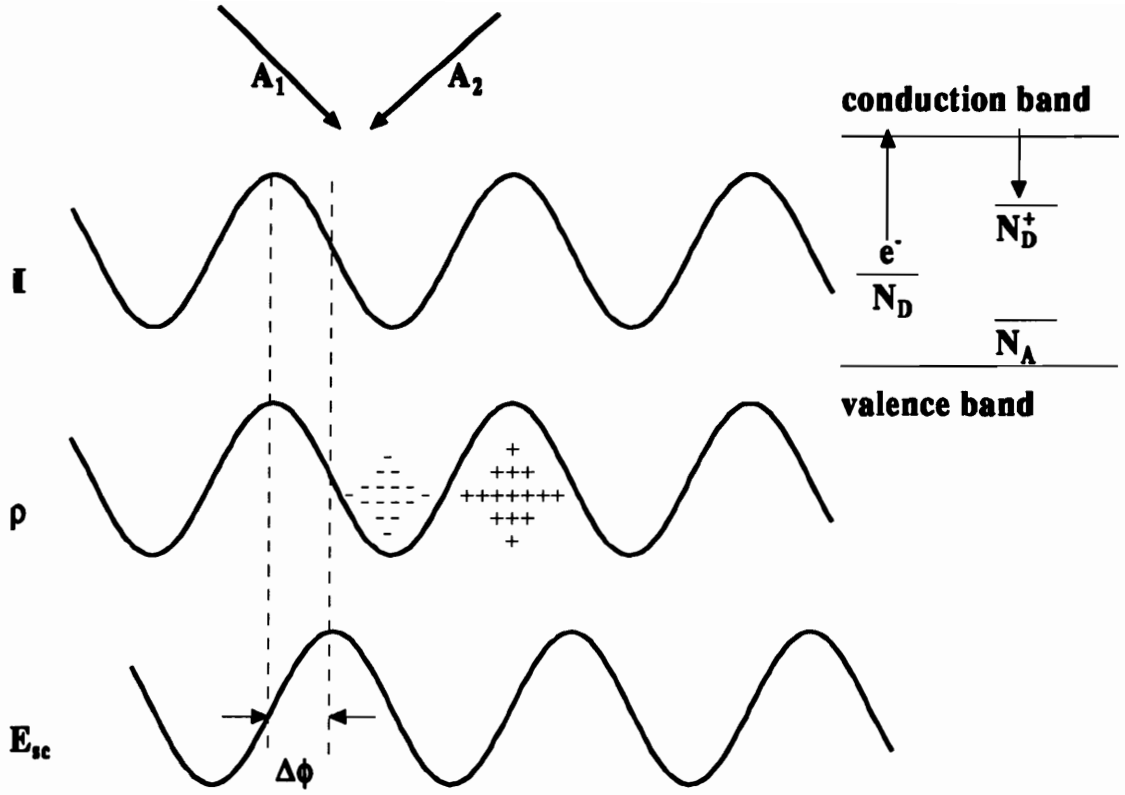

Figure 1.1: Photorefractive grating formation via two wave mixing. The interference pattern I leads to the charge distribution ρ by excitation, transport, and re-trapping of charge carriers (electrons). The charge separation creates a space charge field E_{sc} that is shifted from the interference pattern by an amount $\Delta\phi$ and causes a modulation of the refractive index through the linear electrooptic effect. Inset: Electron excitation from donor sites N_D in regions of high intensity and subsequent re-trapping at ionized donor sites N_D^+ in regions of low intensity. The existence a large number of acceptor sites N_A ensures the existence of many unoccupied donors.

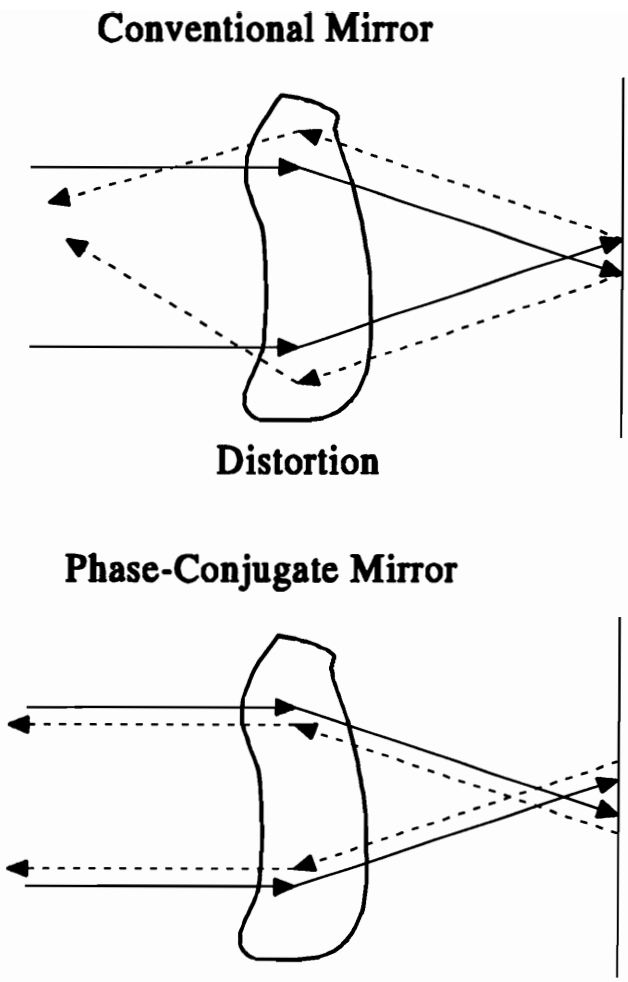

Figure 1.2: Image restoration using a phase-conjugate mirror. Fields propagating from the left in the figure are distorted (frosted glass, transparency, atmosphere etc.). They undergo a time reversed reflection from the phase-conjugate mirror (below) and "heal" themselves after a second propagation through the distortion.

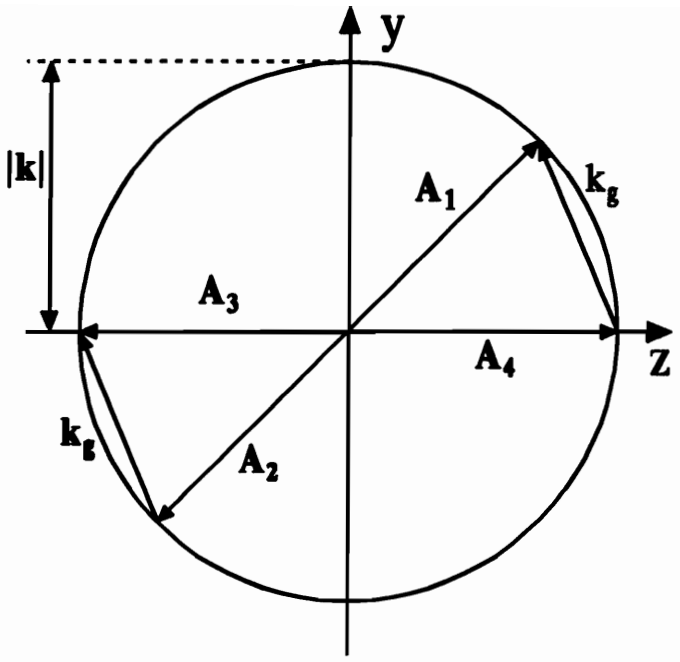

Figure 1.3: Degenerate four wave mixing in a transmission grating geometry. Fields 1 and 4 (2 and 3) form an index grating of wave vector k_g. Field 2 (4) then scatters from this grating in the direction of 3 (1). Thus field 3 (1) is the phase-conjugate field of 4 (2). The process shown here is degenerate in the sense that the all of the fields have the same wavelength so that $|k| = \frac{2\pi}{\lambda}$. Typically only three fields are initially present: two intense pumps (1 and 2) and a weak probe (4). The signal or phase-conjugate field (3) is created by the process.

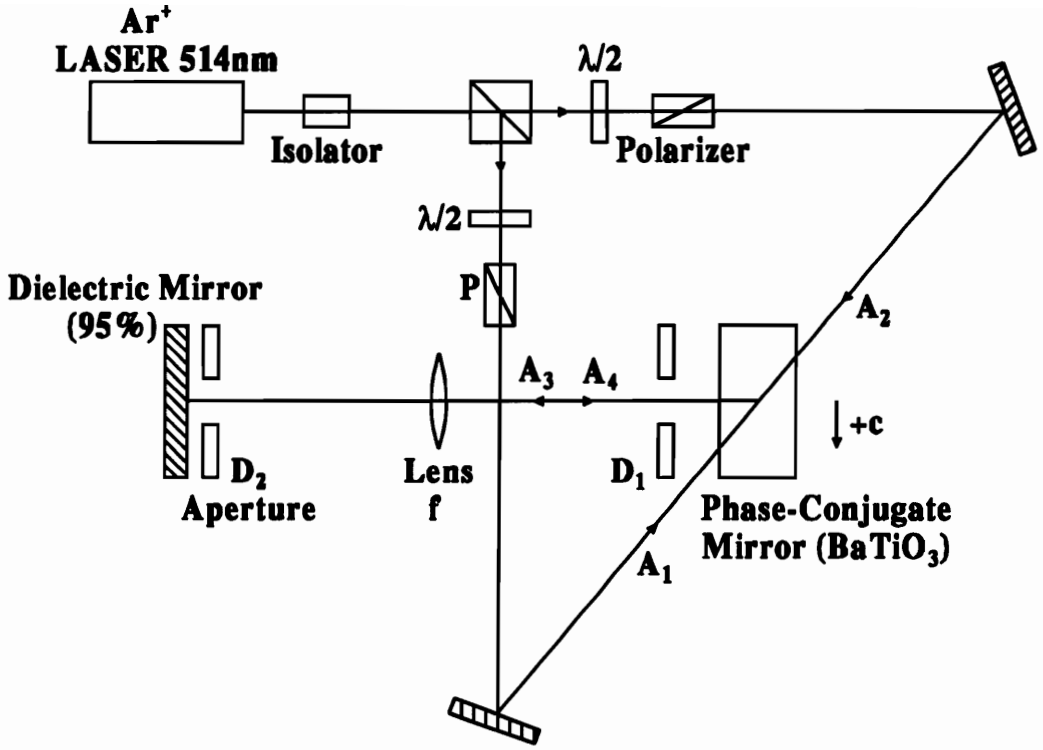

Figure 1.4: Photorefractive phase-conjugate resonator. A_1, A_2: pump fields from Ar^+ laser. A_3, A_4: cavity fields. D_1 D_2: circular apertures placed a distance of one focal length from the cavity lens (focal length 16cm). c: direction of crystal axis. $\lambda/2$: half wave plates used to vary the intensity of the pumps.

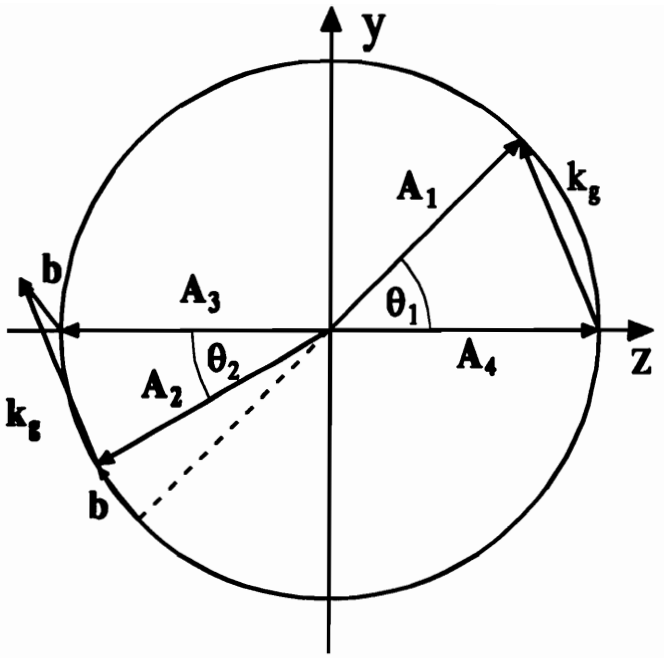

Figure 1.5: Off-Bragg degenerate four wave mixing in a transmission grating geometry. This is similar to figure 1.3 except that one of the pump fields (2) is tilted from a counterpropagating direction of the other (1). The Bragg condition is broken so that the phase-conjugate wave (3) aquires an extra phase (not shown). The parameter $\vec{b}$ is the "Bragg mismatch".

Chapter 2

Model of photorefractive phase-conjugate resonator at low Fresnel number

2.1 Introduction

In this chapter we start the investigation into the dynamics of the PPCR by studying the most simple non stationary state observed. At very low Fresnel numbers (F<2) the resonator field is in a spatially uniform, time independent state. At F~2 periodic phase breathing appears, and at F>2 and with a non vanishing phase mismatch a periodic state sets in. It is characterized by a pair phase defects or vortices of opposite charge that nucleate at the center of the pattern, repel each other along a straight line and disappear at the boundary. After this event, the structureless pattern narrows down rapidly and increases in intensity. It then slowly broadens with an intensity drop at the center until a new pair of vortices nucleates. Figure 2.1 is a snapshot interferogram of the cavity field just after the nucleation of the defects and figure 2.2 shows a sequence of snapshots over one full period of the motion. The full period of the motion occurs on the order of seconds to hundreds of seconds depending on the values of the mismatch and Fresnel number.

This state is important because it is simple to model the field amplitude mathematically. If this mathematical description is correct then one may gain some insight into a physical interpretation of the dynamics. From there one may be able to then predict the states of the system in the rest of parameter space.

The next part of this chapter contains experimental observations of this state as a function of the mismatch. In part three a model is derived that depicts the dynamics in terms of a competition of transverse modes. In part four a description of a holographic correlation technique that will be used to test the validity of the model is presented. The experimental results of the implementation of this technique is presented in section five. A summary of the chapter and concluding remarks regarding the drawbacks of the correlator are included in the final section.

2.2 Dynamics versus Bragg mismatch

The state was first studied by measuring the local intensity of the field in the resonant cavity. This was performed by imaging the field in the plane of aperture D_1 onto a photomultiplier tube that was masked by a pinhole placed close to the center of the nucleation site of the defects. Time series were collected over at least nine full periods of the motion with the resonator shown in figure 1.3 equipped with apertures D_1~430μm and D_2~488μm so that F~2.5. A momentum mismatch was introduced into the system by an angular shift of pump A_1 in both the horizontal (x) direction and vertical (y) direction. With respect to figure 1.4, this mismatch is approximately represented by the expression $n_b(\theta_1 - \theta_2)$ in the vertical direction and a similar expression in the horizontal direction. This parameter was scanned in both transverse dimensions and for all non-vanishing values a two-vortex splitting state was observed.

A typical set of results is shown in figure 2.3. The momentum mismatch was varied by scanning the incidence angle of the pump over a range of about 1mrad in both the horizontal (figure 2.3a) and vertical (figure 2.3b) directions. In each case, the two traces correspond to two different fixed angular offsets in the direction perpendicular to

the direction of the scanned mismatch. Outside the range shown, the oscillation vanishes as the resonator falls below threshold and the cavity field disappears.

Two major observations are obtained from this data. The first is that the defects repel each other and move along a line normal to the transverse component of the mismatch. Thus for example, a vertical transverse mismatch leads to defect motion along a horizontal line. Additionally, when the sign of the mismatch changes, the signs (see below) of the defects change as well.

The second observation is that the frequency of the motion increases as the mismatch increases as shown in figure 2.3. As the phase matching condition is approached, the frequency goes to zero, leading to a stationary output. This stationary state was found to be sensitive to external perturbations and exhibited random fluctuations on a long time scale. An explanation of these observations is given in the next section.

2.3 Mode competition model

So far there has been no formal definition of a phase defect or optical vortex. The first recorded observations and mathematical descriptions of these entities was given by Nye and Berry [44], and they were first observed in photorefractive oscillators by Arrechi in 1990 [45] and Liu and Indebetouw in 1992 [34]. A variety of terms such as dislocations and phase singularities are currently associated with them, but here we will denote them as phase defects or optical vortices, referring to the helical structure of the wavefront around the ones observed in our experiments.

Defects are characterized by two properties. First, both the real and imaginary parts of the field must vanish at the location of the defect so that the phase at this point is

indeterminate. Second, the variation of phase of the field on a closed loop around a single defect must be equal to a multiple of 2π,

i.e. $$\oint \vec{\nabla}\phi \cdot d\vec{l} = 2\pi m, \qquad m \text{ integer}$$

where ϕ is the phase of the field, m is the topological charge of the defect and $d\vec{l}$ is the closed loop around the defect. Furthermore, defects may have two distinct forms, pure edge and pure screw as shown in figures 2.4 and 2.5, or can be a mixture of the two.

The presence of the defects in the field of the state under study here provides clues then as to the nature of the field itself. A field amplitude with two vortices of opposite charge located at $(r,\theta) = (r_0(t),\theta_0)$ and $(r_0(t),\theta_0+\pi)$ may be written as,

$$V(r,\theta) \propto [re^{i\theta} - r_0(t)e^{i\theta_0}][re^{-i\theta} + r_0(t)e^{-i\theta_0}] = r^2 + 2ir_0(t)r\sin(\theta-\theta_0) - r_0^2, \qquad (2.1)$$

where the radial location of the vortices is given a time dependence in order to model their motion. For this to be a realistic field of the resonator, a field envelope (e.g. Gaussian) vanishing beyond the boundary of the aperture D_1 should appear explicitly in equation 2.1, but is neglected here since we are concerned with the vortex nature of the field. The distribution of equation 2.1 can be generalized to a sum of four competing patterns associated with Gauss-Laguerre functions, which are the typical eigenmodes of an empty cavity having cylindrical geometry,

$$V(r,\theta) \propto z_{00}(t) + z_{01}(t)re^{i\theta} + z_{0\bar{1}}(t)re^{-i\theta} + z_{10}(r^2-1). \qquad (2.2)$$

With the inclusion of the Gaussian field envelope, the 00 pattern has a simple Gaussian profile, the 01 or $0\bar{1}$ patterns have a spiraling phase structure of opposite helicity and vanish at the center, and the 10 pattern has a profile similar to the shape of a Mexican sombrero (for lack of a better description). For this to represent the field of equation 2.1, the coefficients z_{00} and z_{10} of the even patterns must be real and the two other coefficients must be locked in phase as $z_{0\bar{1}} = -z_{01}^*$. One may point out that in our physical system and

in the quasi steady-state limit resulting from the sluggishness of the medium, these conditions are actually dictated by the cavity geometry in which, after one round trip, the field is inverted and imaged onto itself at the aperture D_1 by the cavity lens. The presence of the locked modes is essential for the generation of nontrivial patterns with vortices in this system.

Given a non vanishing amplitude for the locked 01, $0\bar{1}$ modes, the nucleation of vortices in the field and their subsequent motion depend on the relative amplitude of the two modes with circular symmetry. In particular, the necessary condition for vortices' nucleation is $|z_{01}| = a_{01} > 0$ and $z_{10} = a_{10} > z_{00} = a_{00}$ (i.e.: the mode with quadratic radial structure must overcome the homogeneous mode).

The following scenario, compatible with the observations, describes a cycle of vortices' nucleation, motion and disappearance. The scenario is conveniently interpreted by making use of the above nucleation conditions and writing the expression for the field as

$$V(r,\theta)\alpha a_{00}(t) + ia_{01}(t) r\sin(\theta-\theta_0) + a_{10}(t)(r^2-1). \qquad (2.3)$$

(1) $a_{10} \approx 0$

Initially, the homogeneous solution ($a_{00} \neq 0$) prevails. Patterns with higher complexity are produced via the interaction of the medium nonlinearity and the cavity boundary conditions [46] and compete with the homogeneous solution. In this model two patterns are excited, one having radial structure with a π phase shift occurring at r=1 and amplitude a_{10}, and another with a π phase shift chosen along the line $r\cos(\theta-\theta_0) = 0$, which is close to the horizontal x-axis ($\theta_0 = 0$). This choice of the second excited pattern means that the Bragg mismatch must be in the vertical direction, thus adding a preferential phase or wavefront tilt in that direction and breaking the cylindrical symmetry of the system.

(2) $a_{00}/a_{10} > 1$

There are no vortices in the field but a phase gradient develops near the origin. The phase step along the line x=0 is

$$\Delta\phi = 2\tan^{-1}[(a_{01}/2a_{10})(a_{00}/a_{10}-1)^{-1/2}] \qquad (2.4)$$

and the distance between the two phase extrema is

$$\Delta y = 2(a_{00}/a_{10}-1)^{1/2}.$$

This is obtained by equating the derivative of the phase along the line x=0 to zero,

i.e. $$\frac{\partial}{\partial y}\tan^{-1}\left(\frac{a_{01}y}{a_{00}+a_{10}(y^2-1)}\right)=0.$$

Figure 2.6 shows a plot of the wavefront with its phase inhomogeneity near the origin.

(3) $a_{00}/a_{10} = 1$

As the higher order mode overcomes the homogeneous solution, $\Delta\phi \to \pi$ and $\Delta y \to 0$. Thus, the two phase extrema with a π phase difference collapse at the origin. Destructive interference occurs and the intensity vanishes at that point. Simultaneously, the wavefront tears locally and connects with the next wavefront, generating a pair of vortices of opposite charge.

(4) $0 < a_{00}/a_{10} < 1$

As a_{00}/a_{10} decreases, the two vortices repel each other along the zero line of the 01 mode. The position of the vortices are $r = (1-a_{00}/a_{10})^{1/2}$, $\theta = \theta_0 = 0$, $\theta_0 + \pi$, corresponding to the intersection of the zero lines of the real and imaginary parts of equation 2.3,

i.e. $r\sin\theta = y = 0$ and $a_{00} + a_{10}(r^2-1) = 0$.

Between the two vortices, each wavefront is connected with the next one. A plot of this wavefront is shown in figure 2.7. As a_{00}/a_{10} decreases further, the two vortices move further apart and eventually disappear beyond the boundary and the wavefront recovers its homogeneity.

The salient points of this scenario are the following. A phase instability precedes the nucleation of the vortices. Nucleation occurs only if higher order modes are sufficiently excited. A periodic repetition of this scenario implies a periodic energy exchange between the homogeneous mode and the mode with a radial π phase shift, as well as with the two locked modes with angular momenta ± 1.

2.4 Correlator Experiment

Several important features of this scenario were verified experimentally. The experiment consisted of measuring directly the overlap integral of the field $V(\vec{r},t)$ exiting the resonator with simple phase patterns $\phi_n(\vec{r})$ which can be associated with the modes appearing in the scenario. Here $\vec{r}$ just represents the transverse (x,y) coordinates. The setup sketched in figure 2.8 is a multichannel optical correlator in which the searched patterns are stored in different holograms or matched spatial filters [62]. The holograms have an amplitude transmittance of the form

$$1+\left|\phi_n(\vec{r})\right|^2+\phi_n(\vec{r})e^{i\frac{2\pi}{\lambda}\alpha x}+\phi_n^*(\vec{r})e^{-i\frac{2\pi}{\lambda}\alpha x}, \qquad (2.5)$$

where α represents the angle between the field $\phi_n(\vec{r})$ and a reference beam used to generate the hologram. After passing the cavity field V through the hologram, the wave diffracted at an angle $-\alpha$ has the form

$$\phi_n^*(\vec{r})e^{-i\frac{2\pi}{\lambda}\alpha x}V(\vec{r},t).$$

A lens is used to Fourier transform this field onto a detector located in the focal plane of the lens,

i.e. $$F\left[\phi_n^*(\vec{r})e^{-i\frac{2\pi}{\lambda}\alpha x}V(\vec{r},t)\right]$$

where the two dimensional Fourier transform is defined as

$$F[\phi(u,v)] = \tilde{\phi}(u,v) = \int \phi(x,y) e^{-i2\pi(ux+vy)}.$$

For a lens the spatial frequency of an image in its focal plane with coordinates (x',y') is given by

$$u = \frac{x'}{\lambda f} \text{ and } v = \frac{y'}{\lambda f}.$$

Thus after some algebra, the field at the detector can be shown to be proportional to,

$$\iint \tilde{\phi}_n^*(u' - u + \alpha/\lambda, v' - v)\tilde{V}(u', v', t)du'dv'. \quad (2.6)$$

By placing a pinhole at the point $u = \frac{\alpha}{\lambda}$, v=0 , corresponding to $x = f\alpha$, y=0, in front of the detector, the measured photocurrent is proportional to the overlap integral

$$\iint \tilde{\phi}_n^*(x', y')\tilde{V}(x', y')dx'dy'. \quad (2.7)$$

Furthermore, since ϕ_n is matched to one of the modes in $V(\vec{r}, t)$, the measured intensity at the detectors is given by

$$S_n(t) = |a_n(t)|^2, \quad (2.8)$$

where $a_n(t)$ is the coefficient corresponding to the mode in the expansion of $V(\vec{r}, t)$ that is matched by ϕ_n.

2.5 Results

For the experiment only the phase information was included in the holograms. Thus a certain level of cross talk is to be expected if the patterns are not orthogonal or if there is a size mismatch between the patterns and the cavity field. Some background will also be present because the pinholes have finite sizes.

The gain of the correlator's four channels, including detector gain and hologram efficiency, were adjusted to the same value to within approximately twenty percent. Four outputs could be recorded simultaneously. These were either four correlation amplitudes, three amplitudes and the local intensity at the center of the aperture A_1, or three amplitudes and the total power. The origins of time for two sets of data recorded sequentially were made coincident by matching the output of a particular channel recorded in both sets.

The patterns used are shown in figure 2.9. The first four (figure 2.9 a to d) are the patterns considered in the competition model. L_{00} has a homogeneous phase, L_{10} has a ring phase shifted by π, and L_{01} and $L_{0\bar{1}}$ have helical wavefronts with angular momenta $\pm$ 1 respectively. The orthogonality of the patterns was checked by measuring the correlation output of each one with a homogeneous cavity field obtained with a Fresnel number smaller than two. The correlation with the homogeneous pattern (2.9a) gave a maximum while the correlation with the three other patterns was zero (i.e. below the expected background). In addition, the four holograms were correlated in an external setup with a field having a helical wavefront. The correlation for three of the holograms was zero, and the hologram with angular momentum of the correct sign gave a maximum.

The correlation amplitudes of the holograms with the actual cavity field are shown in figure 2.10a and b. The first trace in figure 2.10a is the local intensity measured through a pinhole at the center of the field and shown as a reference. This is compared with the fluctuation of the total beam power in figure 2.10c. The second and third traces in figure 2.10a show that the amplitudes of the two modes with circular symmetry oscillate in quadrature (one is a maximum when the other is zero). This confirms that there is a periodic energy exchange between these two modes. The amplitude of the

mode with homogeneous phase drops to near zero when the amplitudes of the higher order mode and the mode with angular momentum (fourth trace in figure 2.10a) are high.

The pattern H_{01} in figure 2.9e has a π phase shift along the x-axis. Strong correlation is expected with this pattern if indeed L_{01} and $L_{0\bar{1}}$ are locked in phase opposition. This is clearly verified by the first three traces of figure 2.10b, which show the correlation coefficients of the two modes with angular momenta ± 1 and the pattern resulting from their phase locking.

The sixth pattern H_{20} in figure 2.9f is associated with a Hermite mode $x^2 - 0.5$. Replacing the symmetrical mode $r^2 - 1$ in equation 2.2 by this mode would also lead to the nucleation of two vortices, but the temporal evolution of the wavefront would be different from that described in the previous section. It was thus useful to check whether the optical correlator could make a distinction between the two possibilities. This is indeed the case. The fourth trace in figure 2.10b shows little correlation with the H_{20} mode. The measured signal is slightly above the background and oscillates in synchronism with the amplitude of the homogeneous mode. This crosstalk is presumably due to a lack of orthogonality of these two patterns.

Finally, two additional patterns shown in figure 2.9g and h were checked. H_{10} has a π phase shift along y and L_{02} has an angular momentum of two. The first pattern could result from the locking in phase (rather than in opposition) of the two modes with angular momenta ± 1 and the second pattern is expected to appear only in fields containing two or more pairs of vortices. As expected, the last two traces in figure 2.10b show no correlation with these patterns, confirming that they are not present in the beam.

2.6 Conclusion

In this chapter a detailed analysis of the first non stationary state was presented. Both the speed of the periodic dynamics and the direction of the defects' trajectories were shown to be controlled by the Bragg mismatch. In particular, as the mismatch increases the speed of the dynamics was shown to increase in a nonlinear manner and the direction of the trajectories was shown to be perpendicular to the direction of the mismatch. It was argued that this broken rotational symmetry of the homogeneous stationary state is due to the additional transverse phase induced by the broken symmetry in the four wave mixing process.

Additionally, a model based on the competition of a few simple spatial field patterns or modes was developed. The necessary patterns representing the observed dynamics are two rotationally symmetric modes and a single asymmetric mode. The asymmetry is produced by the additional transverse phase generated by the mismatch, which is equivalent to the two patterns with angular momenta ± 1 locking in phase opposition. A holographic correlator was constructed in order to confirm the validity of the model by optically measuring the correlation between the cavity field and a few simple spatial patterns representing the modes assumed to participate in the competition. These were stored in phase holograms and matched the patterns of the model. The results showed that the two symmetric patterns oscillate in phase quadrature and the asymmetric mode follows the symmetric pattern that contains a π phase shift. This result fully confirms the presumed model. In addition, different modes that could lead to similar dynamics were checked using the correlator and found not to be present in the cavity field.

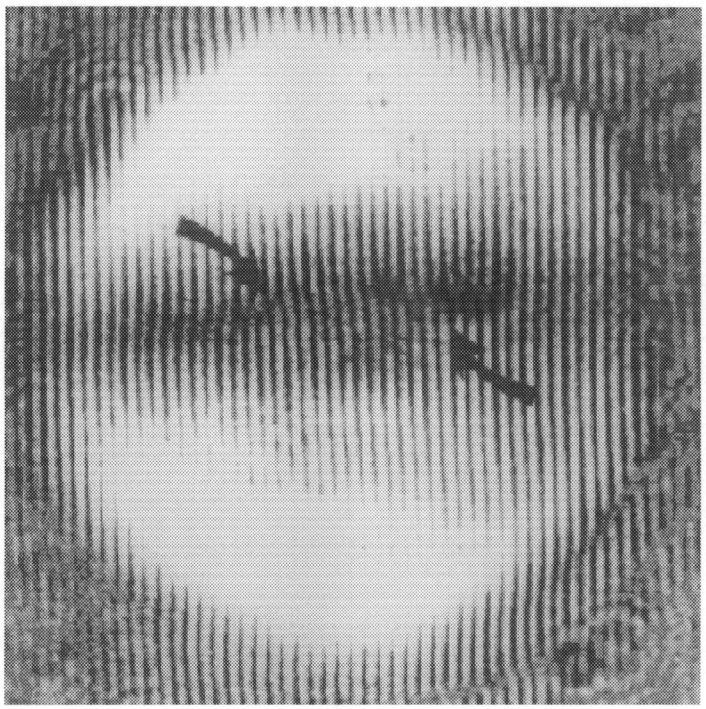

Figure 2.1: Snapshot interferogram of the cavity field at F≈2.0. The interference of the field with a tilted plane wave reveals two phase defects of opposite charge highlighted by the arrows.

Despite the success of the application of the correlator to this simple state, its utility remains doubtful at higher Fresnel numbers where the dynamics are spatially more complicated. This increased complexity means that a greater number of patterns must be tested as the Fresnel number is increased. Therefore many holograms must be constructed in order to test for the presence and temporal behavior of these patterns. This means that the stationarity of the system becomes an issue since it is only practical to test a few patterns at a time. Also the complexity of the holograms increases for more complicated patterns and, while it was a simple matter to construct simple spatially orthogonal holograms for the simple state, it may prove more difficult to produce the more detailed holograms and accurately match them to the cavity modes for a more complex dynamics. In addition, it is likely that this difficulty will lead to decreased spatial orthogonality between the holograms and therefore crosstalk between the cavity modes and the individual holograms will yield spurious correlation amplitudes.

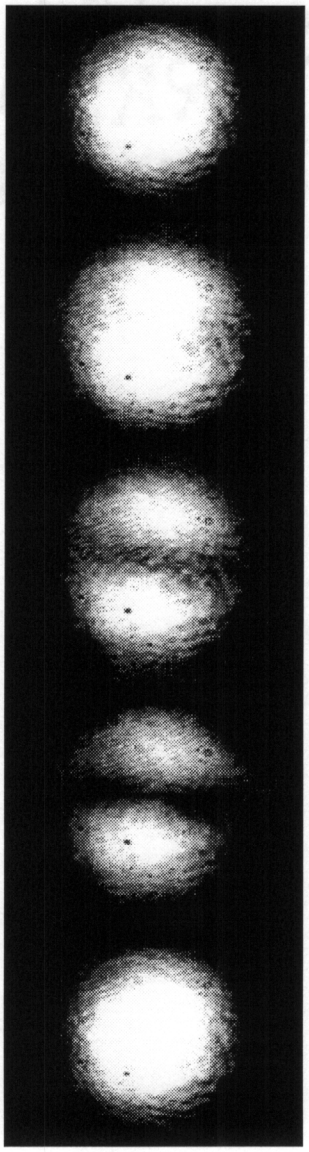

Figure 2.2: Sequence of snapshots of the cavity field at F≈2.0. The sequence covers one full period (about 15 seconds for this particular set). Time increases from the top to the bottom.

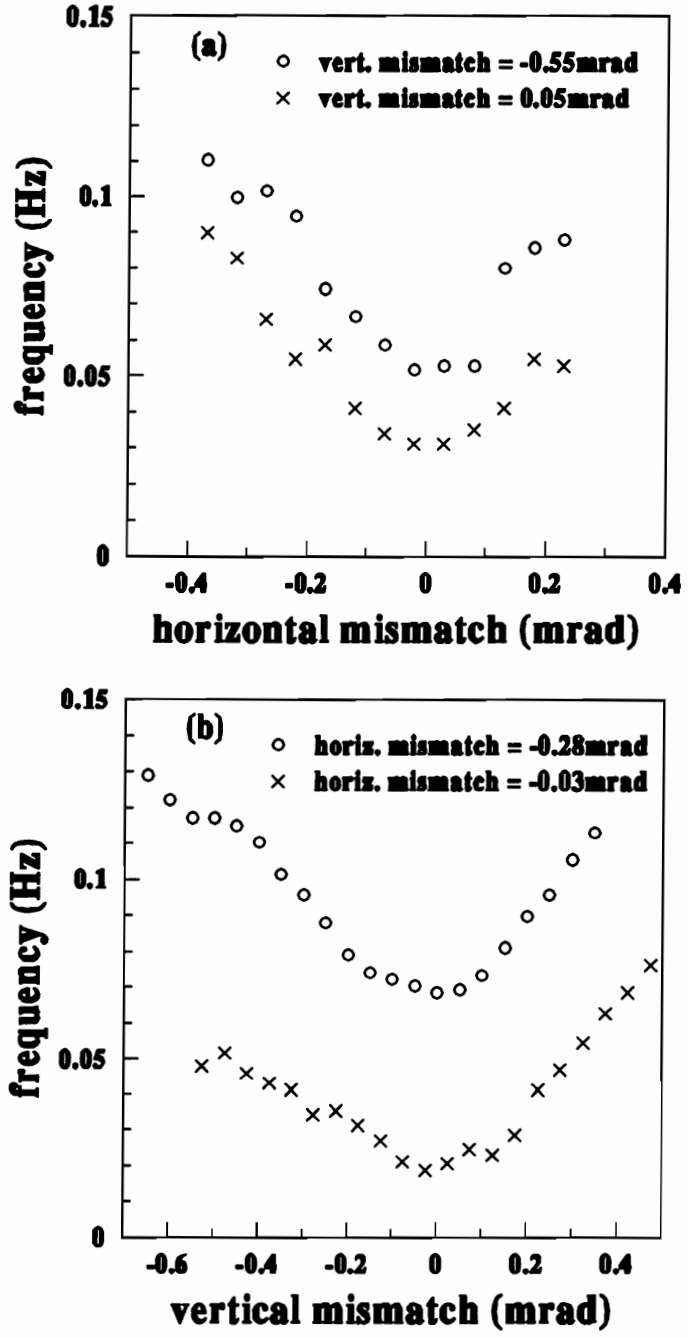

Figure 2.3: Oscillation frequency versus angular mismatch of pump 1. (a) Horizontal scan with fixed horizontal offset. (b) Vertical scan with horizontal offset.

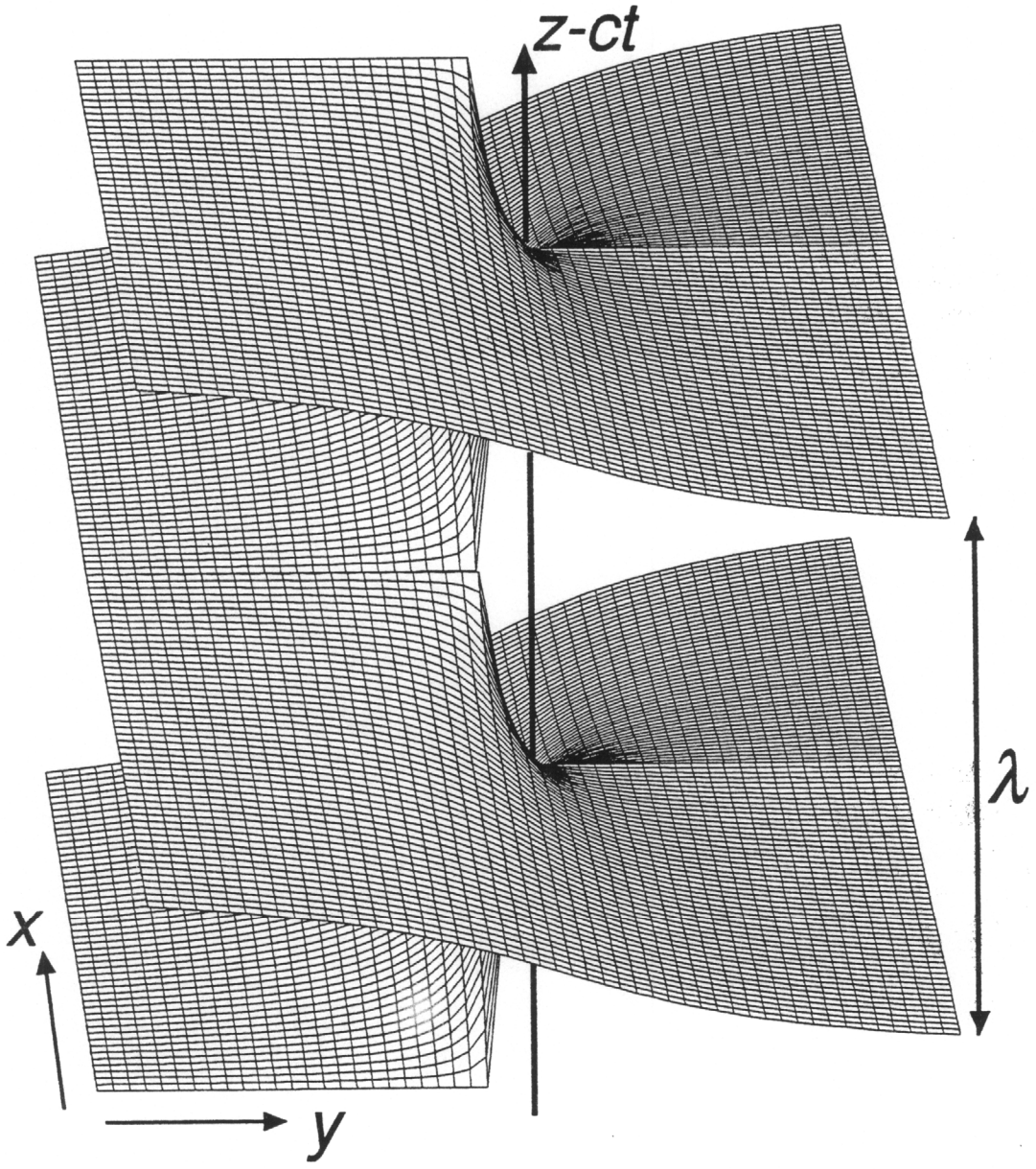

Figure 2.4: Screw dislocation in a traveling wave. The helical wavefront rotates clockwise around the dislocation which is along the axis of propagation. The clockwise rotation corresponds to a positive charge [46].

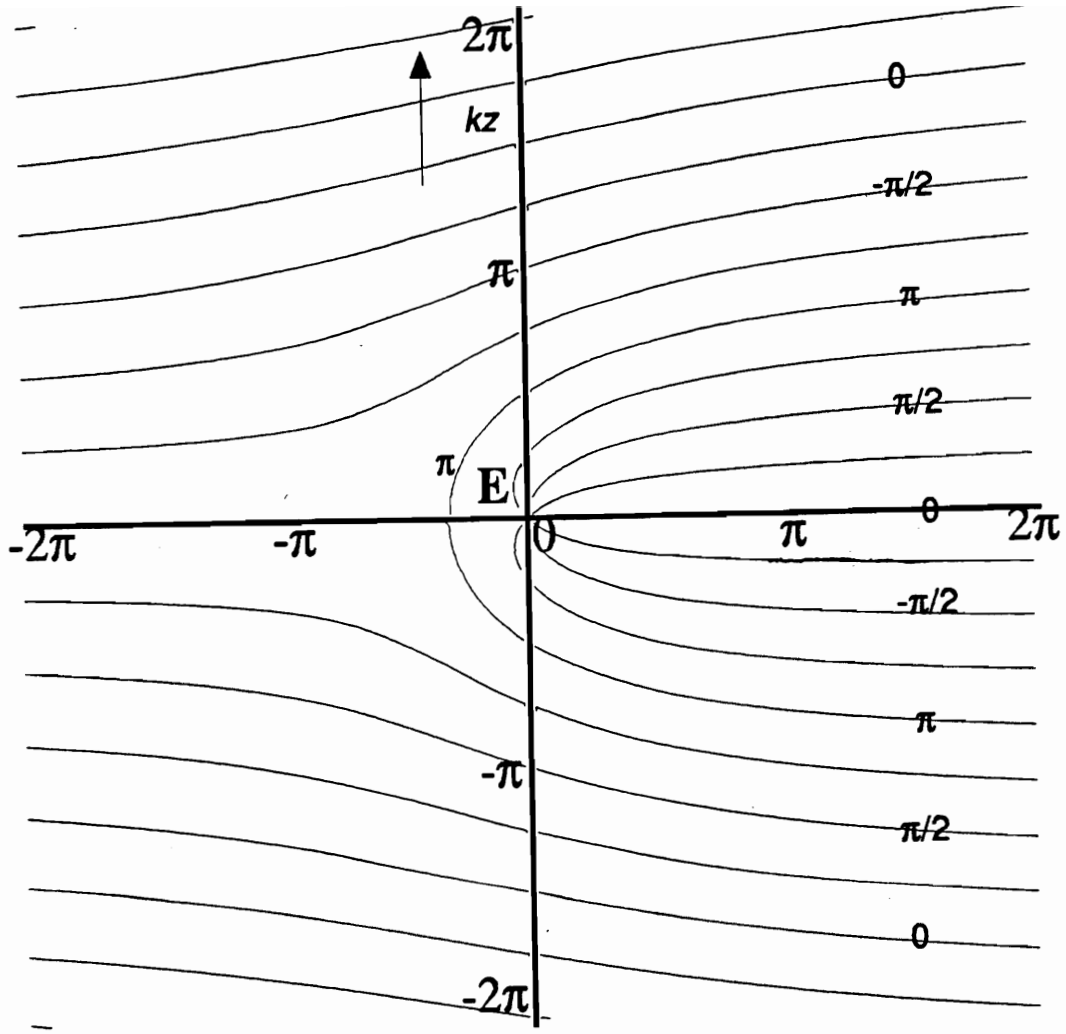

Figure 2.5: Contour plot of the phase of a travelling wave containing an edge dislocation. The wave travels upwards with the dislocation momentarily located on the horizontal axis [46].

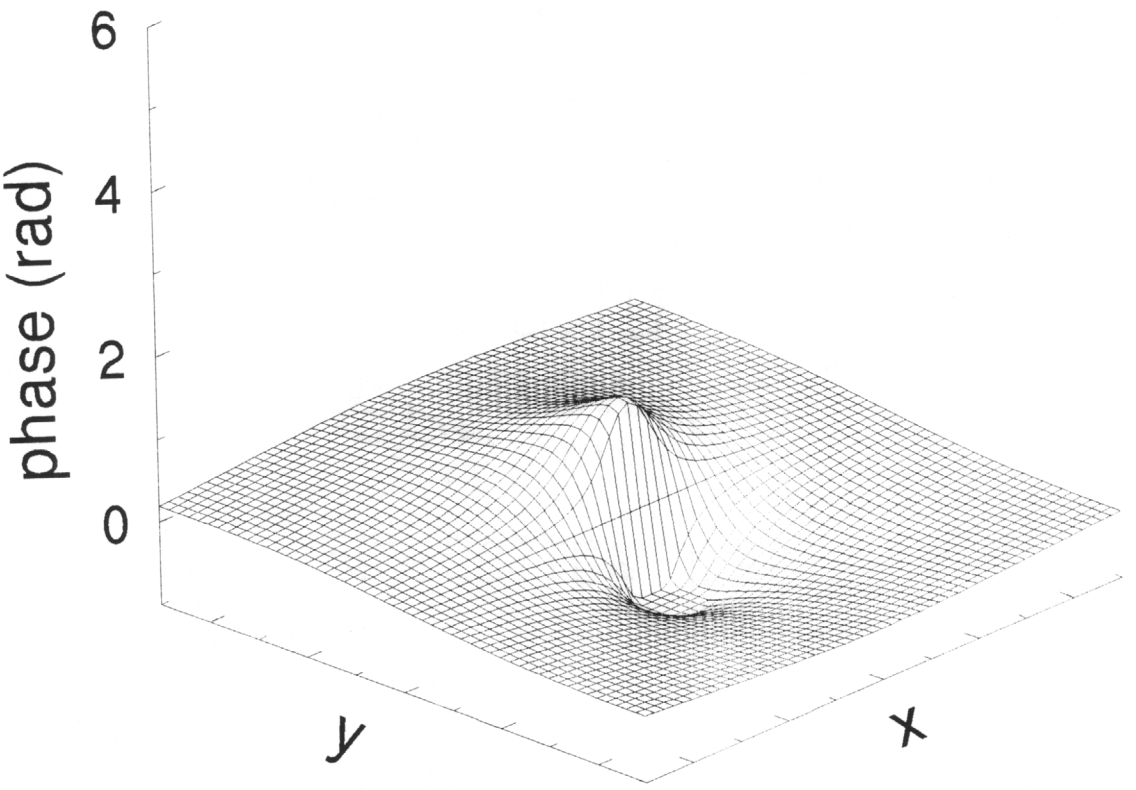

Figure 2.6: Wavefront in aperture A_1 predicted by the model when $a_{00}/a_{10} > 1$ and showing the build up of a phase gradient at the center of the beam.

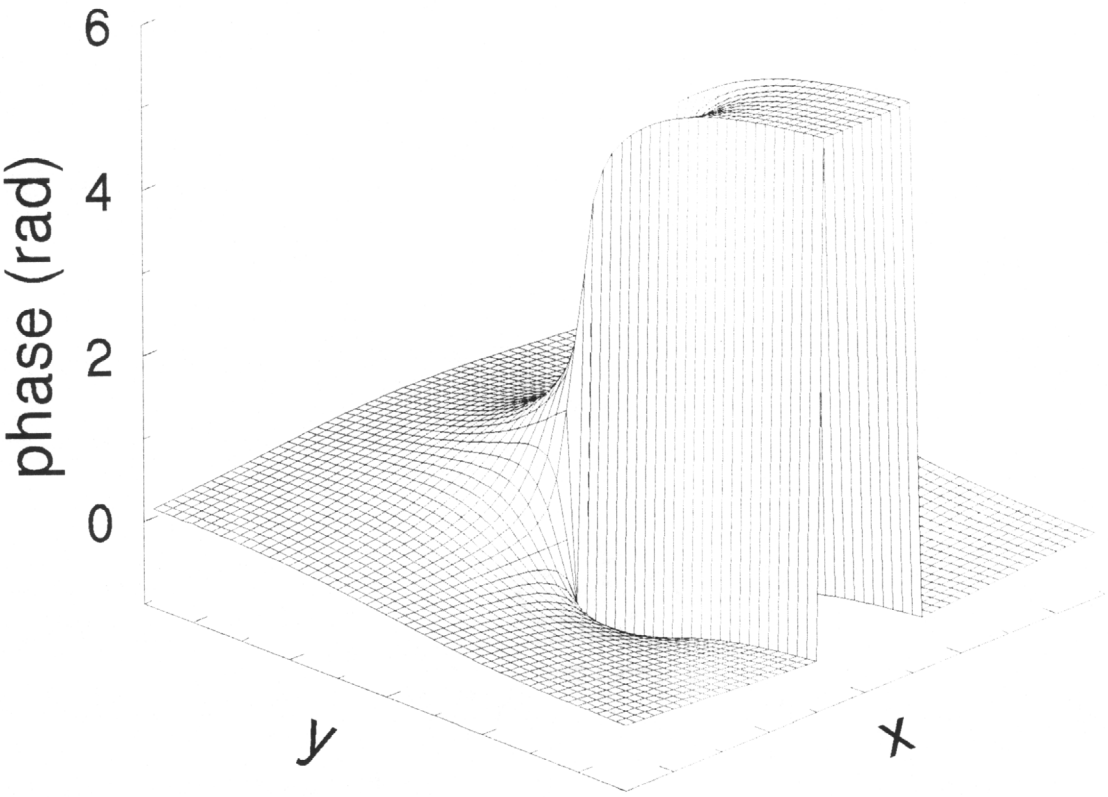

Figure 2.7: Wavefront containing a pair of vortices of opposite charge which nucleate at the center when $a_{00}/a_{10} = 1$ in the model.

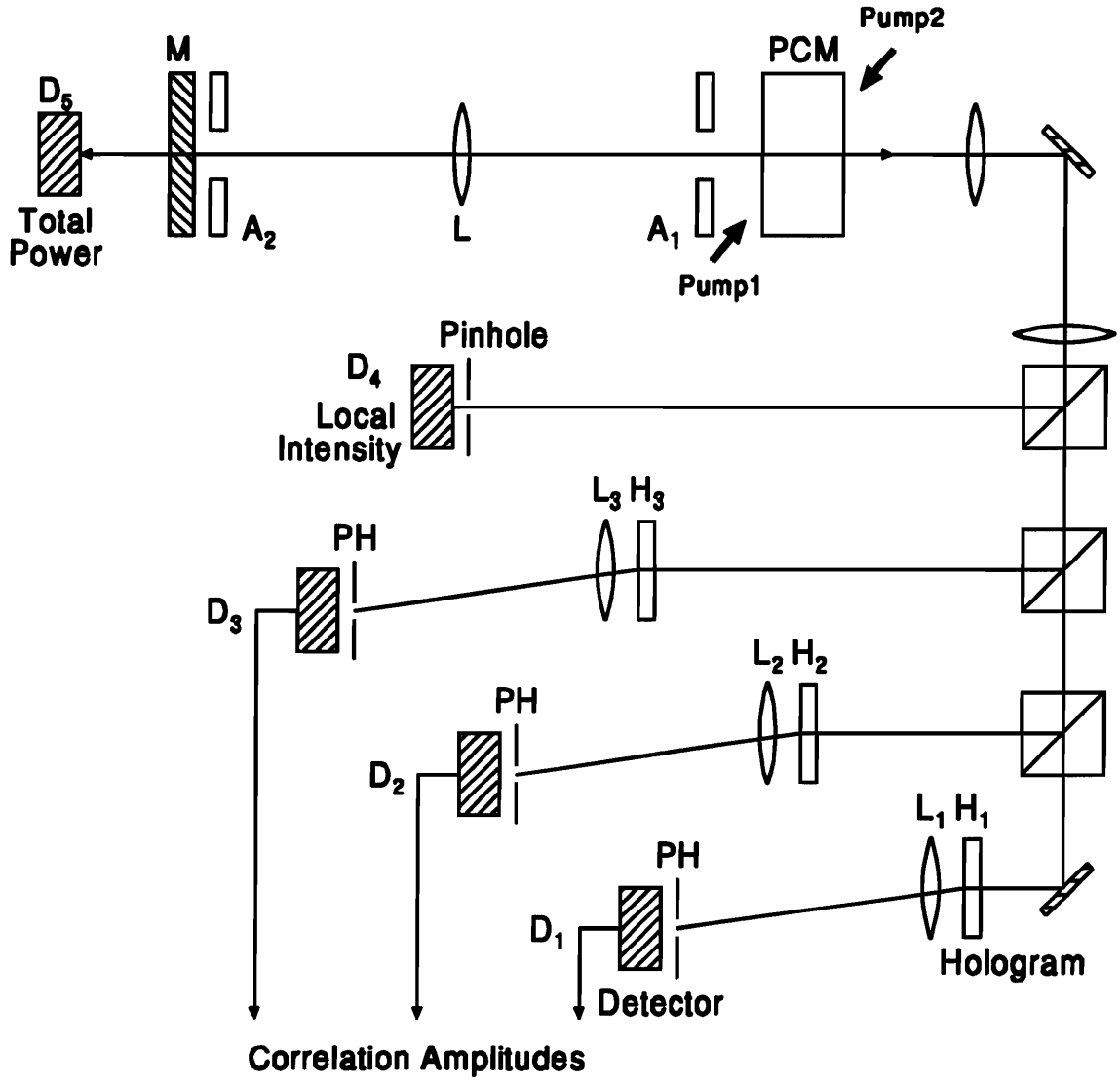

Figure 2.8: Schematic diagram of the holographic correlator. The cavity field at aperture A_1 is imaged onto the holograms H. The detectors D measure the correlation amplitude between the patterns stored in the holograms and the cavity field.

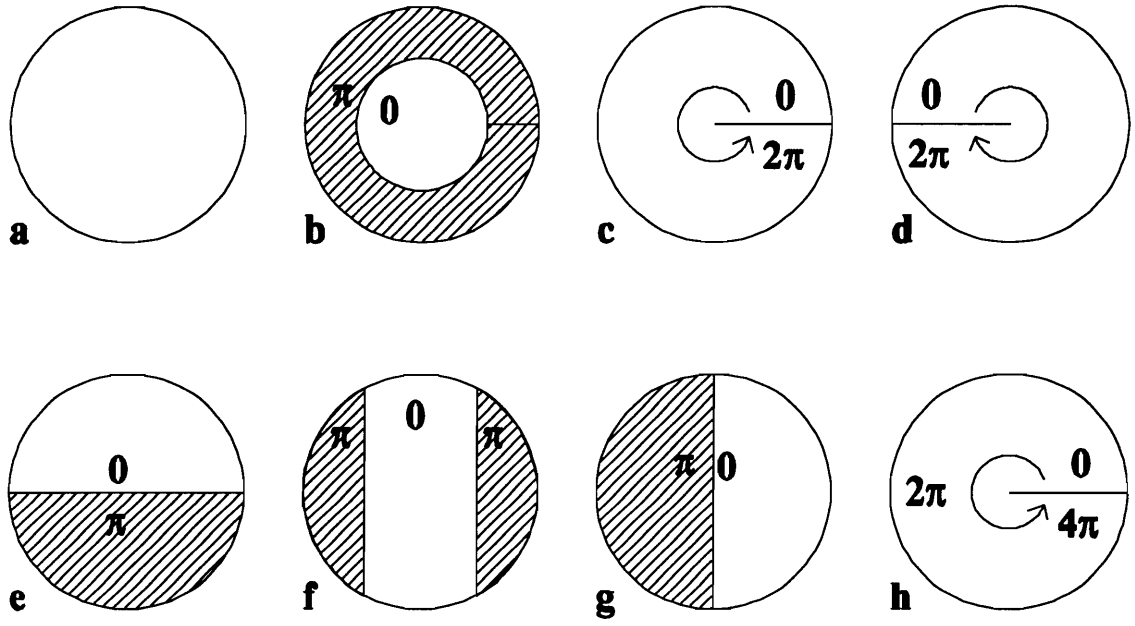

Figure 2.9: Phase patterns used as holographic matched filters. (a)-(d) identify the four modes of the model. (e) is used to check the phase locking of the two modes with angular momenta ±1. (f)-(h) are matched to other modes not present in the model.

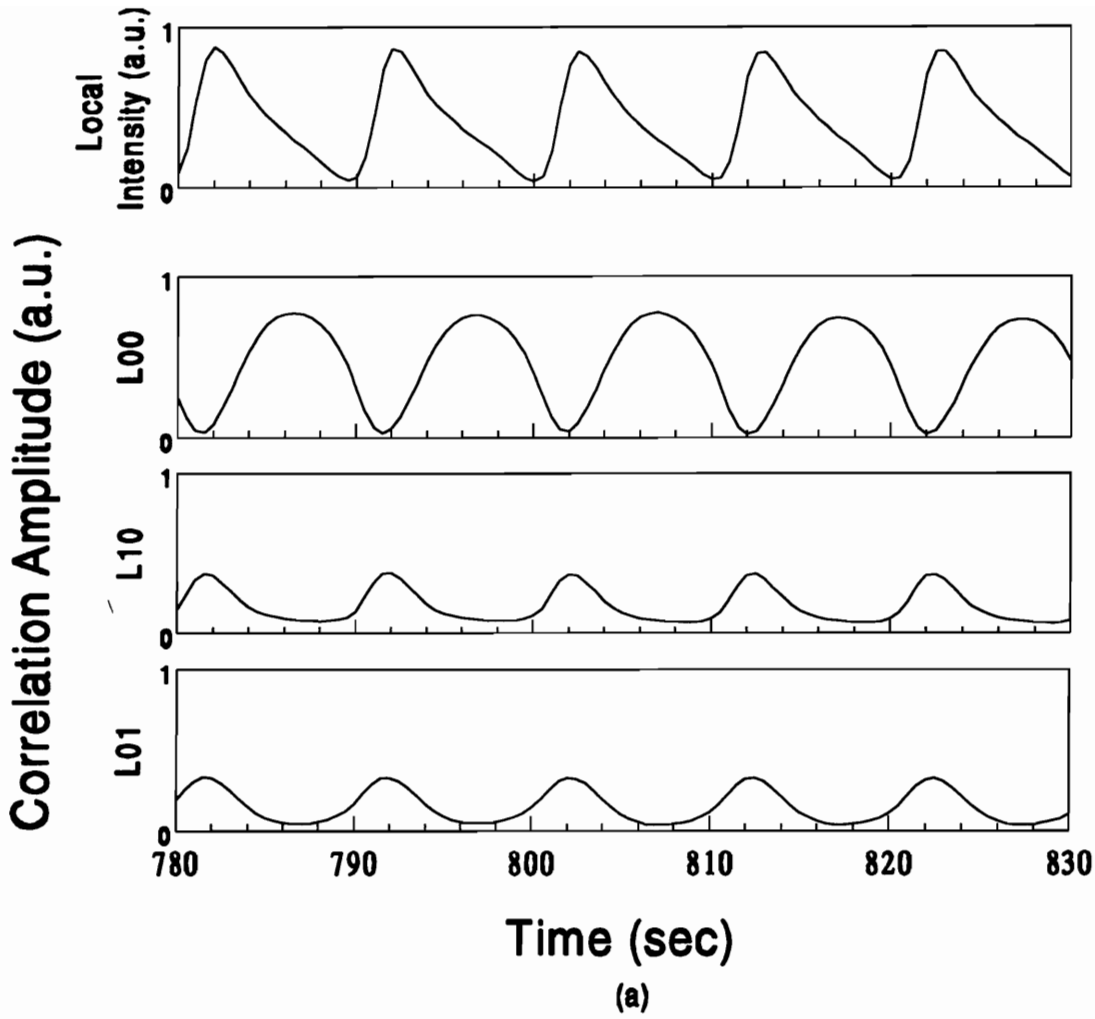

Figure 2.10: Measured correlation amplitudes, local intensities and total power. (a) local intensity at the center of aperture A_1 (trace 1) and correlation amplitudes with the homogeneous mode L_{00} (trace 2), the mode L_{10} with a phase shift on a ring (trace 3) and the mode L_{01} with angular momentum +1 (trace 4). Trace 2 and 3 indicate a periodic energy transfer between the two modes with circular symmetry.

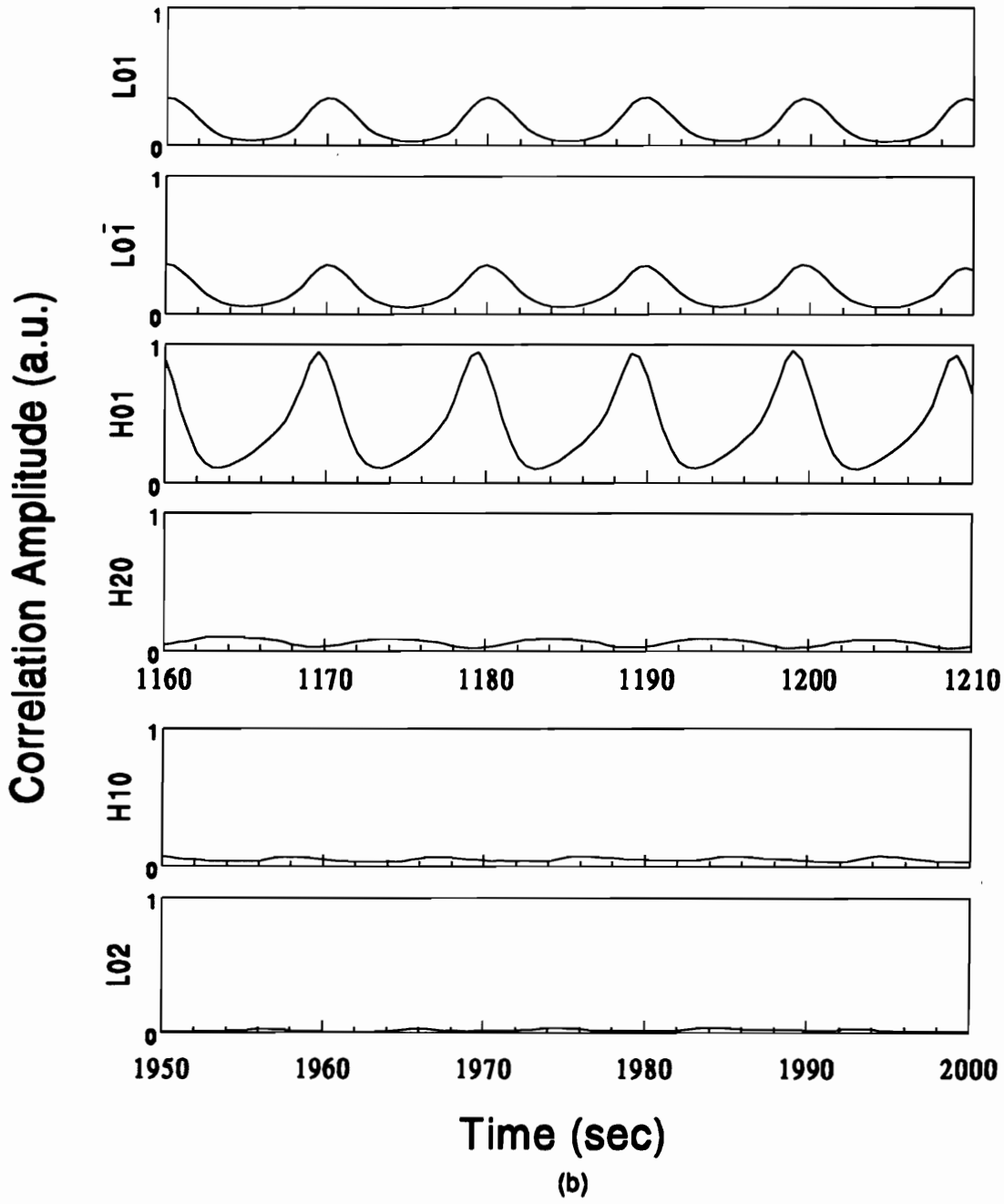

(b) correlation amplitudes with the two modes L_{01}, $L_{0\bar{1}}$ with angular momenta ±1 (traces 1, 2) and the mode H_{01} resulting from locking in phase opposition (trace 3). The three last traces are the correlation amplitudes with the three patterns not included in the model.

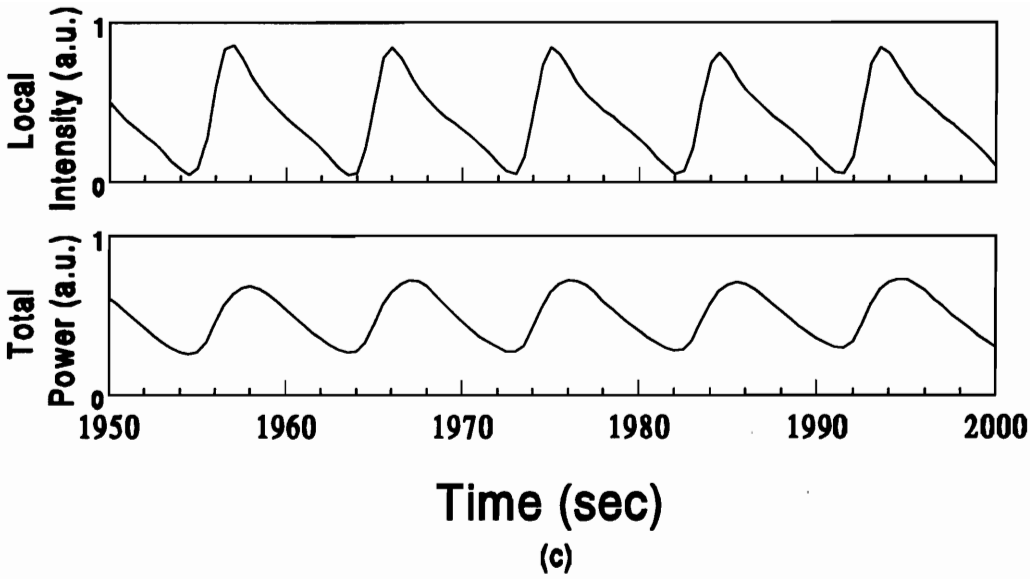

(c) local intensity at the center of aperture A_1 and total power output measured through the dielectric mirror

Chapter 3

Karhunen-Loève Decomposition

3.1 Introduction

In the previous chapter a simple model based on the competition of a few spatial patterns was proposed to predict the behavior of the PPCR in its first non stationary state. The model was verified by using a holographic correlator, but as pointed out in the conclusion of chapter two, this approach is difficult to implement at higher Fresnel numbers. Furthermore, it remains to be seen if the dynamics can in general be modeled in terms of mode competition. So far most work involving nonlinear optical resonators such as the photorefractive ring and lasers, has used the empty cavity modal approach to describe the observed phenomena in those systems. This is done either by using symmetry arguments or frequency shifts to guess the solution of the system [48-50], or by treating the nonlinearity of the gain medium as perturbing the empty cavity mode solutions [51,52]. In reference [50] for example, a photorefractive ring cavity that is pumped using two wave mixing is studied. The geometry of the ring cavity is chosen to be symmetric or antisymmetric depending on the number of mirrors it contains, which then imposes constraints on the symmetry of the modes the cavity can support. The dynamics experimentally observed in the cavity are then reproduced by considering the symmetry of these modes, their resonant frequency and the longitudinal cavity detuning from the pump frequency. On the other hand, in reference [51] a different approach is taken in which the field of a laser is decomposed into empty cavity modes multiplied by temporal coefficients. The decomposition is then inserted into the Maxwell-Bloch

equations describing the interaction of the field with the gain medium. These equations are then solved for the temporal coefficients.

Although it was perhaps fortuitous that the symmetry method worked for the simple state of the PPCR in the previous chapter, it is less justifiable to use such an approach for all parameter values. In a PPCR the phase-conjugate mirror is only active when the cavity field exists and it continuously adapts itself to this field. Therefore no empty cavity modes can be defined in principle, and a model based on mode competition becomes somewhat arbitrary.

In reality however, active cavity modes may exist. The problem is that there is no means to calculate such modes using standard techniques due to the experimentally observed temporally varying boundary conditions. That is, as the cavity field changes new gratings are always forming and contributing to the four wave mixing process. As a consequence it is difficult to implement pattern recognition schemes like the one described in [17] for example, because it is necessary to distinguish between the various transverse modes of the system. Also, if the system can be described by a small number of spatial modes competing for the gain in the crystal, then an analytical analysis of it would be more manageable than if one had to directly integrate the fully three dimensional photorefractive equations [53].

In this chapter we address this problem by studying the transverse intensity distribution of the resonator by employing the method of the Karhunen-Loève decomposition. The decomposition is a method whereby real space time measurements of the cavity intensity profile can be decomposed into a set of spatially orthogonal patterns multiplied by temporal coefficients. Thus without any prior knowledge of the geometry of the resonator nor of the four wave mixing process, one can determine its active intensity modal structure. In the next section a description of the algorithm for

implementing the Karhunen-Loève decomposition and the way in which it is applied to the PPCR is presented. The subsequent two sections show the results of this application as a function of both the Fresnel number and Bragg mismatch. This includes a comparison of the results of this method for the first non stationary state to those of the holographic correlator. A discussion of the results and concluding remarks are presented in the final section.

3.2 Setup and method

The experimental setup is shown in figure 3.1. The spatial patterns to be used in the decomposition were collected at discrete intervals in time by imaging the field at aperture 1 through aperture 2 and onto a CCD camera. This was done in order to avoid introducing more elements (i.e. a beamsplitter) into the cavity and to avoid amplification of noise via two wave mixing at the other output through the crystal. It should be noted that the same pattern behavior is observed throughout the entire cavity. The sensing area of the CCD array was 6.2mm by 4.6mm with the number of picture elements equal to 500 by 582. Each picture element has a size of 12.7μm by 8.3μm. Time series of the intensity fluctuations were recorded on a 15 by 15 equally spaced lattice, sampled from the picture elements taken from the CCD images and processed on a PC using the Karhunen-Loève algorithm.

The details of the Karhunen-Loève decomposition can be found in reference [54] for example and the method has recently been used to determine the spatial eigenmodes of magnetic fields emitted by the brain [55]. The Karhunen-Loève decomposition is a method of expanding a time varying image $\mathbf{H}(t)$ into spatially orthonormal "eigenpatterns" weighted by time dependent coefficients:

$$\mathbf{h}(t) = \sum_{k=1}^{N} \xi_k(t)\mathbf{v}^{(k)}, \tag{3.1}$$

where $h_i(t) = H_i(t) - \overline{H}_i$ with $\overline{H}_i = \frac{1}{T}\int_T H_i(t)dt$.

Here H_i is the time series recorded at the lattice point i and N is the number of lattice points (the dimension of $\mathbf{H}(t)$ equal to 225 in this experiment) and the temporal integration is taken over the length of the time series T. The main idea of the decomposition is that the eigenpatterns $\mathbf{v}^{(k)}$ are chosen as the eigenvectors of the covariance matrix i. e.,

$$R_{mn} = \frac{1}{\tau}\int_T h_m(t)h_n(t)dt, \tag{3.2}$$

where $\tau = \sum_{i=1}^{N}\int_T h_i^2(t)dt$ is the sum of the values of the zero time delay autocorrelations at each lattice point. This factor normalizes the matrix so that its trace is equal to unity.

The importance of this method is that this choice of eigenpatterns provides an optimally fast convergence to the original signal [54]. The expansion can then be truncated, with minimum error, to include only the patterns that correspond to the most significant spatial structures participating in the dynamics, which we term modes. For example, at F≈2.0 there should only be a few spatially orthogonal patterns allowed to oscillate in the cavity as was confirmed in chapter two. Therefore one would expect that this method should reveal only this same number of significant patterns while the rest of the eigenvectors could be attributed to noise and/or numerical round off errors.

These spatial structures or eigenpatterns are solutions of the eigenvalue problem

$$\tilde{\mathbf{R}}\mathbf{v}^{(k)} = \lambda_k\mathbf{v}^{(k)}, \tag{3.3}$$

where λ_k is the eigenvalue corresponding to the eigenvector $\mathbf{v}^{(k)}$. From (1), the time dependent coefficients are then given by

$$\xi_k(t) = \mathbf{v}^{(k)} \cdot \mathbf{h}(t). \tag{3.4}$$

Note that since the matrix $\ddot{\mathbf{R}}$ is real and symmetric, the eigenvalues are real and nonnegative and the eigenvectors orthogonal,

i.e. $$\mathbf{v}^{(k)} \cdot \mathbf{v}^{(k')} = \delta_{kk'}.$$

It is also important to point out that the eigenvalues λ_k are a measure of the significance of the corresponding eigenpattern $\mathbf{v}^{(k)}$ to the dynamics since

$$\frac{1}{\tau}\int_T \xi_k(t)\xi_{k'}(t)dt = \lambda_k \delta_{kk'}. \qquad (3.5)$$

The integral in equation 3.5 corresponds to the temporally averaged magnitude of the coefficients of the eigenvectors. Therefore a plot of $\log(\lambda_k)$ as a function of k can be used to determine the modes that constitute the most significant spatial structures participating in the dynamics and can be used to determine the truncation point of the significant eigenvectors. So again, at F≈2.0 it is expected that there would be only a few large eigenvalues corresponding to the modes that in some way represent the field patterns of the model presented in chapter two.

In order to avoid confusion, it is necessary to explicitly point out that the modes defined here as the significant eigenvectors of the covariance matrix should not be confused with the field eigenmodes of an empty cavity (e.g. Gauss-Laguerre or Gauss-Hermite modes in lasers), but instead they can be regarded as the active intensity eigenpatterns of the transverse intensity fluctuations in the resonator.

3.3 Dynamics versus Fresnel number

First the Bragg mismatch was held at a fixed, non-zero value and the Fresnel number was varied from a value of 2.0 to 4.8 by changing the size of aperture A_2. Examples of the most significant modes, their eigenvalues, and their coefficients are shown in figures 3.2 and 3.4-3.7. In the eigenvector plots, dark represents larger values

of the eigenvectors. It should be mentioned however that the polarity of the pattern is not a relevant parameter. The patterns are calculated from the intensity fluctuations about a mean and their polarity can be changed as long as the sign of the corresponding coefficient in the time series is also changed. The dynamics of the transverse intensity patterns is distinct for the three ranges of Fresnel number defined approximately as $2.0 \leq F \leq 3.0$, $3.0 \leq F \leq 4.0$, and $4.0 \leq F \leq 5.0$.

(a) $\underline{2.0 \leq F \leq 3.0}$

As described in chapter two, this region corresponds to a non stationary transverse pattern that consists of two phase defects of opposite charge periodically nucleating at the center of the pattern, traveling along a straight line, and vanishing at the boundary. The Karhunen-Loève decomposition reveals two modes with large eigenvalues (figure 3.2), one with circular symmetry resembling a lowest order Gauss-Laguerre (0,0) mode and the other, asymmetric mode, which can be interpreted as the superposition of a Gauss-Laguerre (1,0) and a Gauss-Hermite (1,0). Thus the two most significant eigenvectors derived from the Karhunen-Loève decomposition require at least three conventional Gauss-Laguerre or Hermite modes for their representation. Their coefficients oscillate in phase quadrature, which is in agreement with previous results obtained in chapter two, demonstrating the validity of this method. To further demonstrate this, the Gauss-Laguerre (0,0) and the superposition of a Gauss-Laguerre (1,0) and a Gauss-Hermite (1,0) were constructed from their functional forms in figure 3.3. The coefficients of the GL00 and GL10 are taken from their correlation amplitudes measured from the correlator. Although there are some slight differences between the coefficients of the decomposition in figure 3.2 and the correlation amplitudes in figure 3.3, clearly the phase relationship between the modes and their spatial structure are the same.

As the Fresnel number is increased, the value of the largest eigenvalue decreases while the second eigenvalue has a similarly large increase and the background of smaller eigenvalues increases. The ratio of the second largest eigenvalue to the largest increases from approximately 0.017 at F = 2.0 to 0.102 at F = 2.5. Presumably this occurs because as the transverse confinement is relaxed, the losses experienced by the higher order structures decrease.

(b) $\underline{3.0 \leq F \leq 4.0}$

A bifurcation takes place at F≈3.0 so that the pattern now contains two pairs of defects undergoing periodic motion. Again, as the Fresnel number increases the magnitude of the largest eigenvalue decreases while the lesser eigenvalues increase. At F ≈3.1 (figure 3.4) there is a group of three most significant modes followed by a pair of less significant ones, and their patterns map the motion of the defects. The defects move along the nodal lines of the modes. As the modes decrease in significance their spatial structure increases in complexity, with a corresponding decrease in spatial symmetry, and their coefficients tend to oscillate at higher harmonics of the characteristic frequency of the lowest three modes. This frequency change occurs between gaps in the corresponding eigenvalue spectrum. At F≈3.6 (figure 3.5) there is a group of four significant modes separated from a broad background by a large gap. Again the spatial structure increases for higher order modes and their coefficients oscillate at increasing harmonics of the fundamental frequency.

(c) $\underline{4.0 \leq F \leq 5.0}$

Here the dynamics undergoes another bifurcation to patterns that can contain up to three defect pairs. The largest eigenvalue continues to decrease through F≈4.2, an aperiodic state as shown in figure 3.6, and then increases by F≈4.8 where the dynamics locks to a periodic state (figure 3.7). The aperiodic nature of the state at F≈4.2 is

demonstrated by the local intensity fluctuations at a single point in the field (figure 3.6d) and by the broadband frequency spectrum of this local time series, which is a signature of possible chaos. Surprisingly, the spatial structures of the lower, most significant modes remain essentially unchanged between these two states despite the fact that they exhibit entirely different temporal behaviors.

At F≈4.2 there is a continuous spectrum of eigenvalues with a very large background suggesting that a large number of spatial modes participate in the dynamics. The lower order modes still appear to oscillate periodically with some irregularity, but the higher modes are aperiodic. For F≈4.8 only six modes may be considered significant, two of which have eigenvalues much larger than the others (figure 3.7). These two low order modes oscillate periodically in phase quadrature, while the other four oscillate irregularly with an average frequency twice that of the fundamental.

A decomposition in the frequency domain was also performed on these two states in order to identify which structures dominate the dynamics at a particular frequency. This decomposition is given by

$$\mathbf{h}(t) = \sum_{k=1}^{N} \int \eta_k(\omega)\mathbf{w}^{(k)}(\omega)e^{i\omega t}d\omega, \tag{3.6}$$

where the modes $\mathbf{w}^{(k)}$ with amplitudes η_k at each frequency ω, are chosen as the eigenvectors of the cross spectral density matrix

$$Q_{mn}(\omega) = \tilde{h}_m(\omega)\tilde{h}_n^*(\omega). \tag{3.7}$$

Here $\tilde{h}_m(\omega)$ is the Fourier transform of $h_m(t)$,

i.e. $$\tilde{h}_m(\omega) = \int h_m(t)e^{-i2\pi\omega t}.$$

. When the matrix is diagonalized, there is only one complex eigenvector at each frequency that represents the spatial structure oscillating at that frequency. For example, if this type of decomposition was performed on a typical single mode, steady state HeNe

laser, the results should reveal a single eigenvector oscillating at $\omega=0$ that resembles a Gauss-Laguerre (0,0) mode.

As expected the decomposition reveals that in the periodic state (F = 4.8) the real and imaginary parts of the eigenvector oscillating at the fundamental frequency are nearly identical to the two most significant eigenvectors oscillating in quadrature in the time domain. At twice this frequency one can still identify similarities between the real and imaginary parts of the eigenvector in the frequency domain with some of the less significant vectors in the time domain. In the aperiodic state (F = 4.2) there is a broadband eigenvalue spectrum in the time domain and only the most significant eigenvector exhibits some degree of periodicity. Consequently, its spatial structure in the time domain decomposition is similar to the real part of the eigenvector at the fundamental frequency. The next most significant eigenvector in the time domain only vaguely resembles the imaginary part of the fundamental frequency mode and eigenvectors oscillating at higher harmonics in frequency space no longer bear resemblance to the eigenvectors in the time domain. It appears then that in the aperiodic state the most significant mode in the time domain has a stable periodic oscillation. The other modes become unstable and are responsible for the complex dynamics observed in the local intensity. The reasons for this behavior are beyond the scope of this work.

3.4 Dynamics versus Bragg mismatch at F≈4.2

Next the dynamics was analyzed as a function of the Bragg mismatch. The angle between the pumps was held at a fixed small non-zero value in the direction perpendicular to the plane defined by the direction of the fixed pumps and the cavity axis (vertical mismatch), and was varied in this plane (horizontal mismatch b_x approximately

represented again by $n_b(\theta_1 - \theta_2)$ of figure 1.5 with x substituted for the y direction). The results presented here are for F = 4.2. In general, for large mismatch the dynamics is aperiodic, relatively fast and lacking spatial symmetry. As the mismatch decreases the system enters periodic states in which the spatial structure becomes increasingly rotationally symmetric. The dynamics is extremely slow when the Bragg mismatch is minimal (no horizontal mismatch, $b_x = 0$ but with the constant vertical mismatch). When the pumps are perfectly collinear (mismatch = 0 horizontally and vertically) the system enters a stationary state consisting of seven high intensity regions forming a centered hexagonal pattern shown in figure 3.11. As the horizontal mismatch is varied from -0.80 to -0.50mrad three characteristic ranges can be identified and described as follows.

(a) $\underline{-0.80 \leq b_x \leq -0.50 \text{ mrad}}$

At large mismatch the system is in an aperiodic state similar to the one shown in figure 3.6. There are many significant modes as indicated by a broad eigenvalue spectrum, and each of them oscillate irregularly. As the mismatch decreases a gap between a small number of significant eigenvalues and the background develops, revealing that the dynamics is becoming less turbulent. Despite the temporal complexity of the states many of the modes still have spatial structure with some degree of rotational symmetry.

(b) $\underline{-0.40 \leq b_x \leq -0.20 \text{ mrad}}$

In this range a bifurcation to periodic states takes place, in which the patterns are characterized by two defect pairs moving around four regions of high intensity. Although there are brief moments when the defects pass through one of these regions or do not exist at all in the pattern, the pattern most often resembles the snapshot shown in figure 3.8. The trajectories of the defects generally lie along the crossed lines separating the high intensity regions, and as the mismatch is varied their motion along this path varies.

As the mismatch is decreased from -0.4 to -0.2 mrad the frequency decreases from 0.14 Hz down to 0.06 Hz. Gaps in the eigenvalue spectra appear, and at b_x = -0.20 mrad the dynamics is dominated by only two significant modes (figure 3.9). In general, all of the modes in this range contain two or four local extrema as expected from figure 3.8, however more structure becomes apparent at b_x = -0.20 mrad which is just prior to the next bifurcation. In this state, the two most significant modes oscillate periodically in phase quadrature and the less significant ones have energy in higher harmonics of the fundamental frequency.

(c) $-0.10 \leq b_x \leq +0.10$ mrad

The next bifurcation is to another periodic state in which the pattern first contains a single defect pair slowly rotating in the central region. The pair then splits into two or three pairs that move around seven bright regions arranged in a centered hexagonal pattern, and eventually vanish at the boundaries. The frequency of the dynamics dramatically slows down to 0.01 Hz at b_x = 0.0 mrad (there is a small non zero vertical mismatch) and speeds up again to 0.06 Hz at b_x = 0.20 mrad. The eigenvalue spectra still have small gaps indicating that there are few significant modes despite the small number of periods contained in the scans. The modes have higher fold rotational symmetry than the ones in the previous range, as shown in figure 3.10 which is the state with b_x = -0.10 mrad. At exact Bragg match, the pattern converges to a stationary centered hexagonal figure (figure 3.11). As the Bragg mismatch is increased in the positive direction the system undergoes bifurcations to states similar to the ones described before for negative b_x.

3.5 Conclusion

The transverse patterns of a linear phase-conjugate resonator were studied experimentally as functions of the cavity Fresnel number and the Bragg mismatch using a Karhunen-Loève decomposition. The method allows one to define the most significant eigenvectors of the covariance matrix and of the cross spectral density matrix of the intensity fluctuations and to interpret them as the active eigenmodes of the resonator. It was tested on the first non stationary state at $F \approx 2.0$ with the results yielding two significant modes oscillating in phase quadrature. These modes are interpreted as the fundamental Gauss-Laguerre (0,0) mode and the superposition of a Gauss-Laguerre (1,0) and a Gauss-Hermite (1,0). This interpretation is in accord with the results of the holographic correlator, thus validating the method.

As the Fresnel number is increased the transverse pattern is expected to become more complex since spatial structures of smaller sizes can oscillate in the cavity. The decomposition supports this by showing an increase in the number of significant spatial modes. These modes exhibit similar structure in the same region of Fresnel number, however their temporal evolution can be quite different. In particular for $4.0 \leq F \leq 5.0$, states containing modes having the same spatial structure can be periodic or aperiodic, suggesting that the system may be described by a small number of coupled spatial modes.

The Bragg mismatch is shown to be responsible for the broken symmetry of the patterns and determines the speed of the dynamics of the system. It appears that with the cavity geometry used, a spatially non uniform stationary state exists only when the phase matching condition is exactly satisfied. These stationary states are not very stable and are destroyed by small external perturbations to the system (e.g. mechanical vibrations).

When there is some mismatch the system always enters a dynamical state except in the range of small Fresnel numbers ($F \leq 2.0$), where there are high losses for all complex spatial structures and only the lowest order stationary mode exists. This behavior can be

understood in terms of both the mismatch and the cavity geometry by considering the following scenario. A seed planar wavefront initially traveling along the cavity axis enters the interaction region of the crystal. The four-wave-mixing process generates a new wave propagating back into the cavity. Since momentum is not conserved with a non-zero mismatch, this wave propagates at some angle with respect to the cavity axis depending upon the magnitude and direction of the Bragg mismatch. After one round-trip in the cavity and an additional phase conjugation, this wave will in turn generate another plane wave traveling at an even larger angle. Therefore energy is exchanged from lower to higher order plane waves. However, this energy exchange cannot proceed without bound and the progressively higher order waves will experience cavity losses greater than their gain in the medium. At the same time the lower order waves are always building up from the scattered noise created by the pumps and cavity fields and from diffraction of the higher orders on the hard apertures. This interplay between the Bragg mismatch, which couples the different plane waves, and the cavity losses is thought to be responsible for the type of dynamics that occurs. A larger phase mismatch allows for faster energy exchange and leads to an increase in speed of the dynamics. The direction of the mismatch controls the direction of the energy exchange and relates to the way in which the rotational symmetry of the system is broken.

At low Fresnel numbers ($2.0 \leq F \leq 3.0$), this scenario leads to a coherent understanding of the observed behavior as described in the previous chapter and in reference [47]. With no phase mismatch and thus no coupling to higher order plane waves, a stationary solution with a planar wavefront prevails. With a phase mismatch momentum is transferred to the phase-conjugate beam. This effect, combined with diffraction on the cavity apertures, leads to the build up of structures having a transverse wave vector parallel to the mismatch and eventually to the nucleation of a defect pair.

At higher Fresnel numbers and with some phase mismatch, the cavity can accommodate several pairs of defects and their motion is more complex. The motion of a defect will depend on the orientation of the Bragg mismatch and the local slope of the wavefront in which it is imbedded. Complex interaction between the defects through the background field may take place, leading to their rotation, attraction, annihilation, and nucleation at various places in the field. With exact phase matching, stationary patterns containing no defects appear to be quasi stable. These patterns are easily destroyed by small external perturbations which break the phase matching condition and usually lead to the nucleation of defects which undergo motion and destabilize the pattern.

The scenario proposed here is based on heuristic arguments attempting to describe the interplay between the cavity losses, the gain of the medium, and the mode coupling. Although a more analytical treatment is necessary if the system is to be controlled and used for practical applications, the Karhunen-Loève decomposition has proven useful in demonstrating both mode competition and symmetry breaking in phase-conjugate resonators. It has also given some insight into the structural form of the modes and how they change, both spatially and temporally, for different dynamical states. If modified, it should prove to be an effective tool for studying the much faster transverse nonlinear systems such as the laser. In these systems there already exists knowledge as to the general possible mode structure of the cavity and this fact, combined with the knowledge gained through the application of the decomposition, should lead to a greater understanding of them.

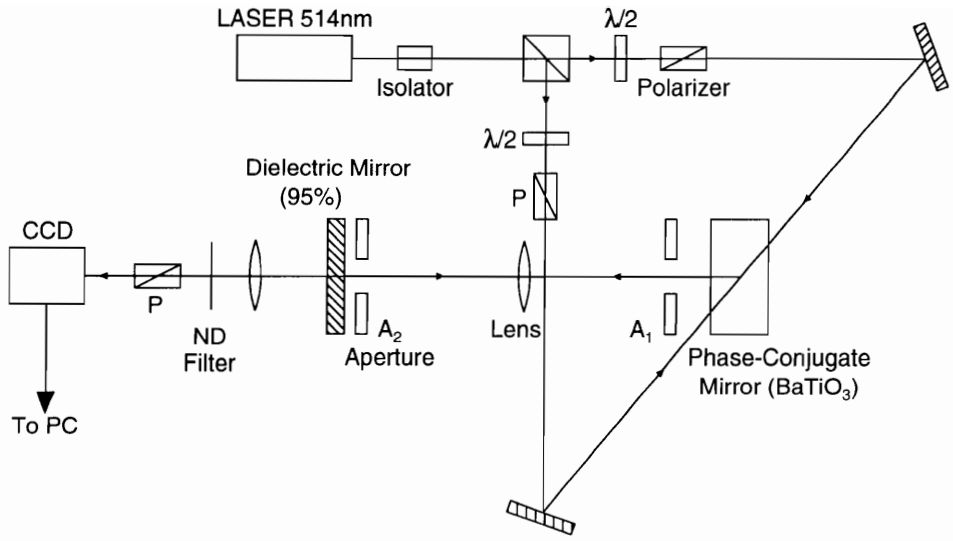

Figure 3.1: Photorefractive phase-conjugate resonator with a confocal cavity. The cavity field at aperture A_1 is imaged through the cavity mirror and onto the CCD array. The neutral density filter and the polarizer adjust the intensity of this field.

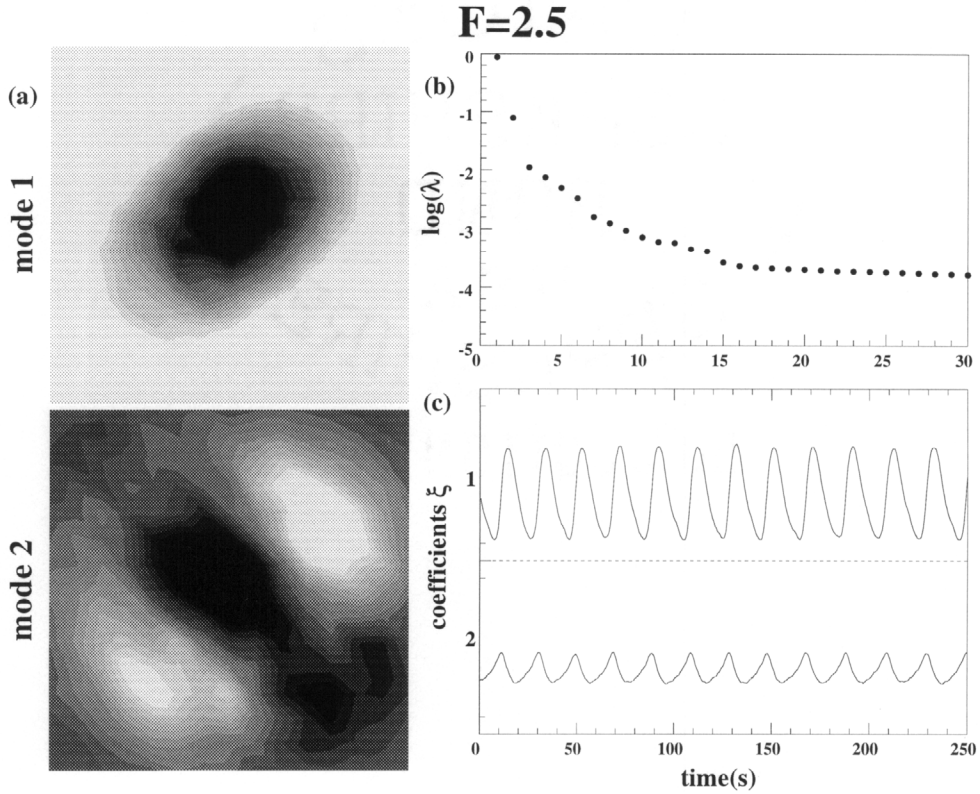

Figure 3.2: Karhunen-Loève decomposition of the resonator transverse pattern at F = 2.5 and non-zero Bragg mismatch. (a) the two most significant eigenvectors. (b) the eigenvalue spectrum. (c) their time dependent coefficients.

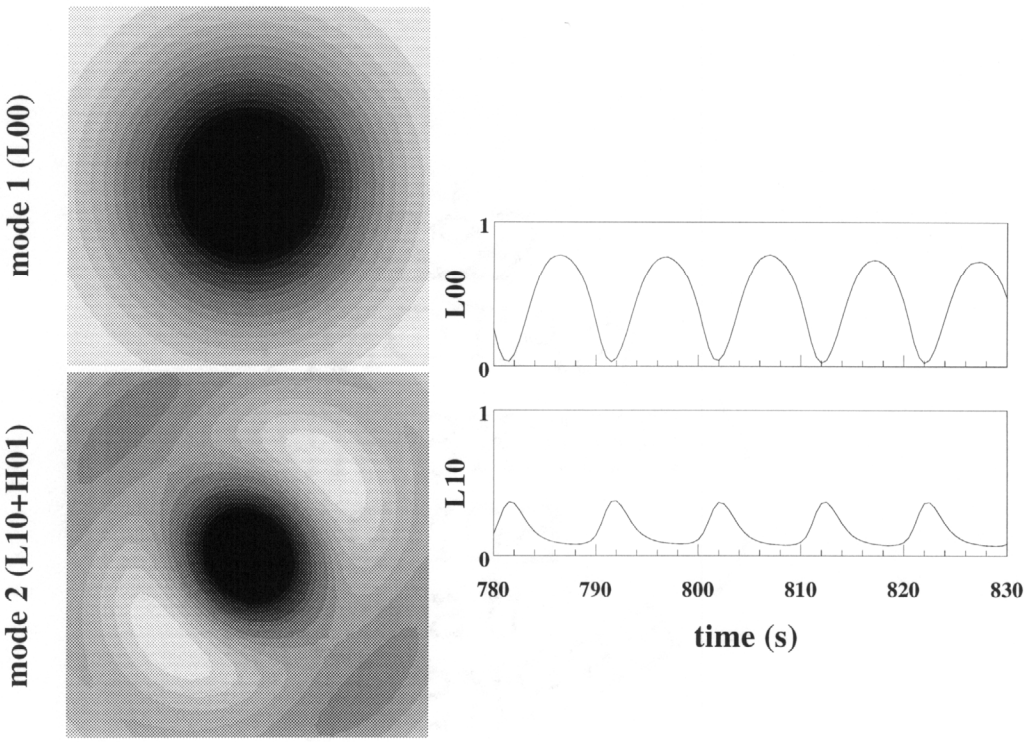

Figure 3.3: Simulation of transverse modes compatible with Karhunen-Loève decomposition results. Top: Gauss-Laguerre 00 mode. Below: Combination of Gauss-Laguerre 10 and Gauss-Hermite 01, the coordinate system is rotated 45° so as to be compatible with figure 3.2. Right: The correlation amplitudes of the GL00 and GL10 taken from the correlator data (see figure 2.10a).

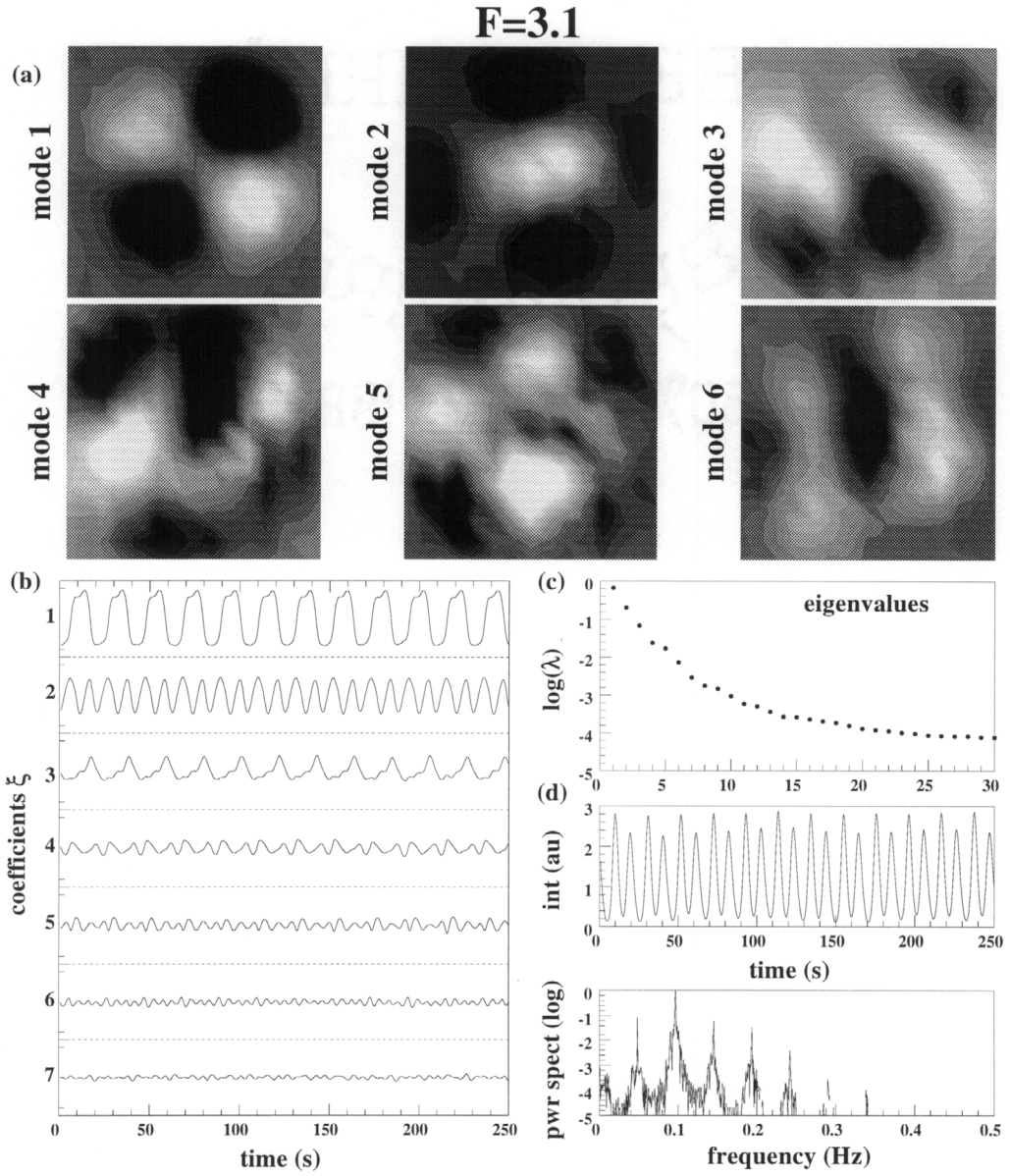

Figure 3.4: Karhunen-Loève decomposition of the resonator transverse pattern at F = 3.1 and non-zero Bragg mismatch. (a) the six most significant eigenvectors. (b) their time dependent coefficients. (c) the eigenvalue spectrum. (d) the local intensity measured at a single point in the transverse distribution and its power spectrum.

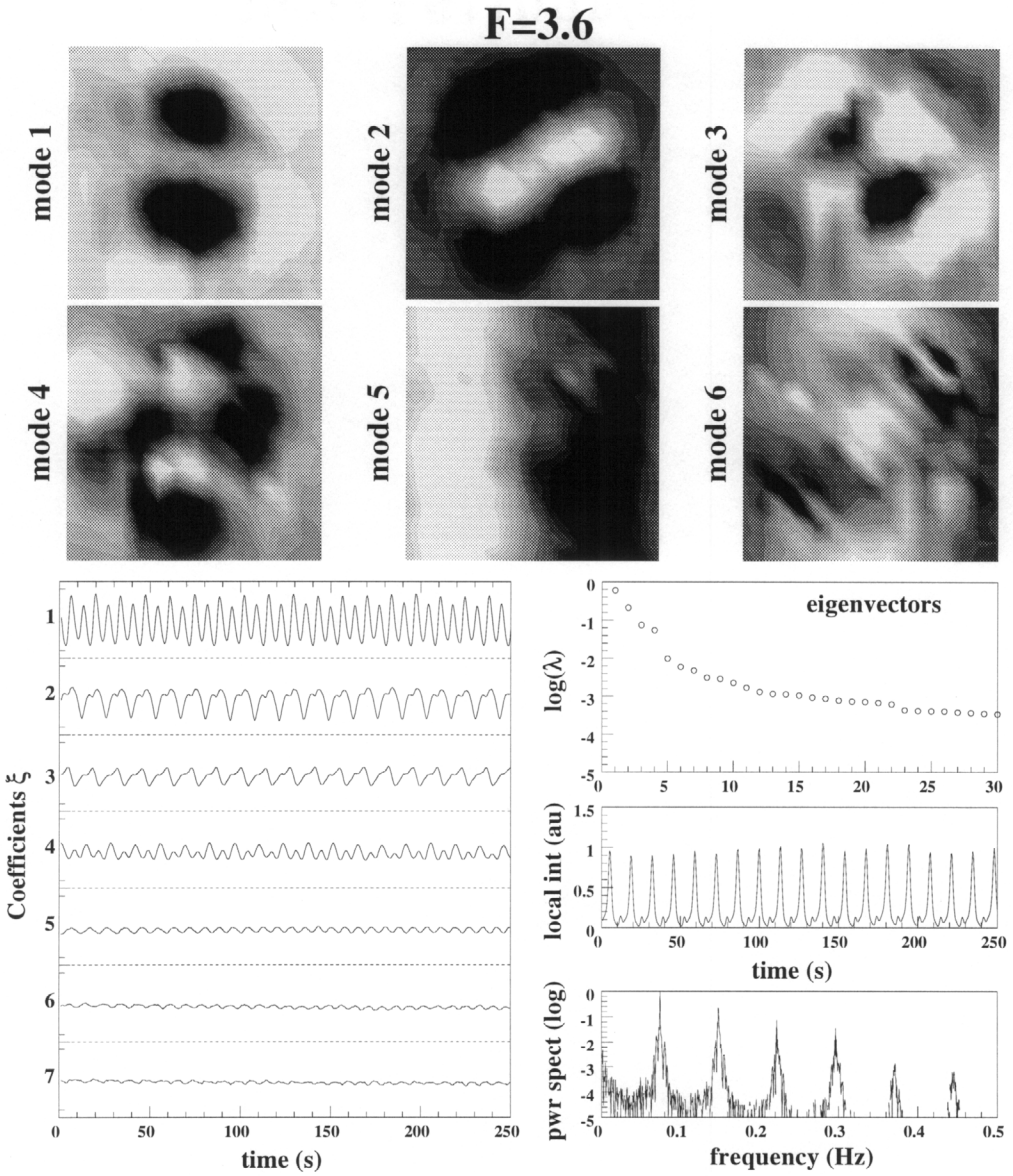

Figure 3.5: Karhunen-Loève decomposition of the resonator transverse pattern at F = 3.6 and non-zero Bragg mismatch. (a) the six most significant eigenvectors. (b) their time dependent coefficients. (c) the eigenvalue spectrum. (d) the local intensity measured at a single point in the transverse distribution and its power spectrum.

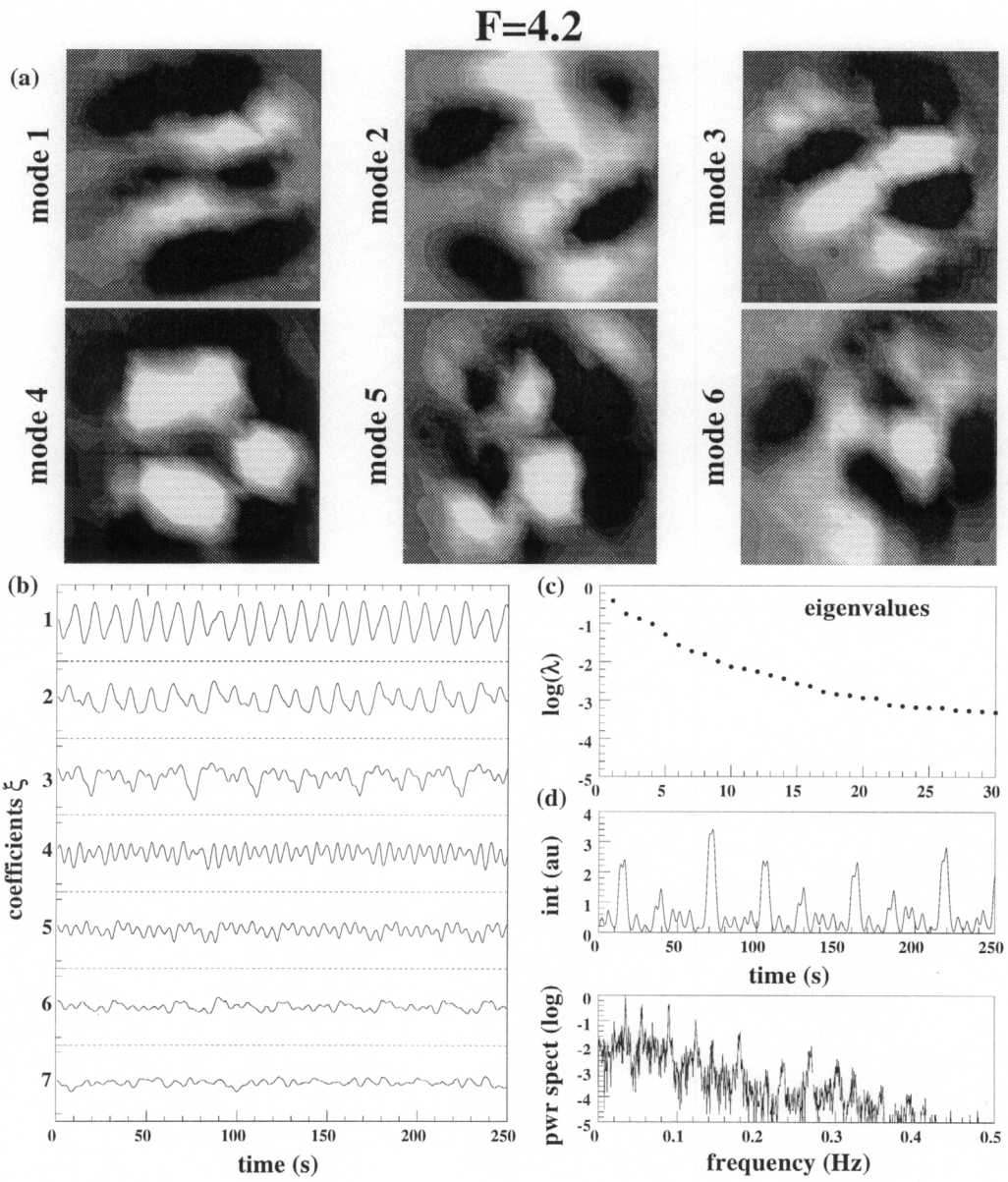

Figure 3.6: Karhunen-Loève decomposition of the resonator transverse pattern at F = 4.2 and non-zero Bragg mismatch. (a) the six most significant eigenvectors. (b) their time dependent coefficients. (c) the eigenvalue spectrum. (d) the local intensity measured at a single point in the transverse distribution and its power spectrum. This is an aperiodic state with a nearly continuous eigenvalue spectrum and a broadband power spectrum of the temporal evolution, indicative of chaos.

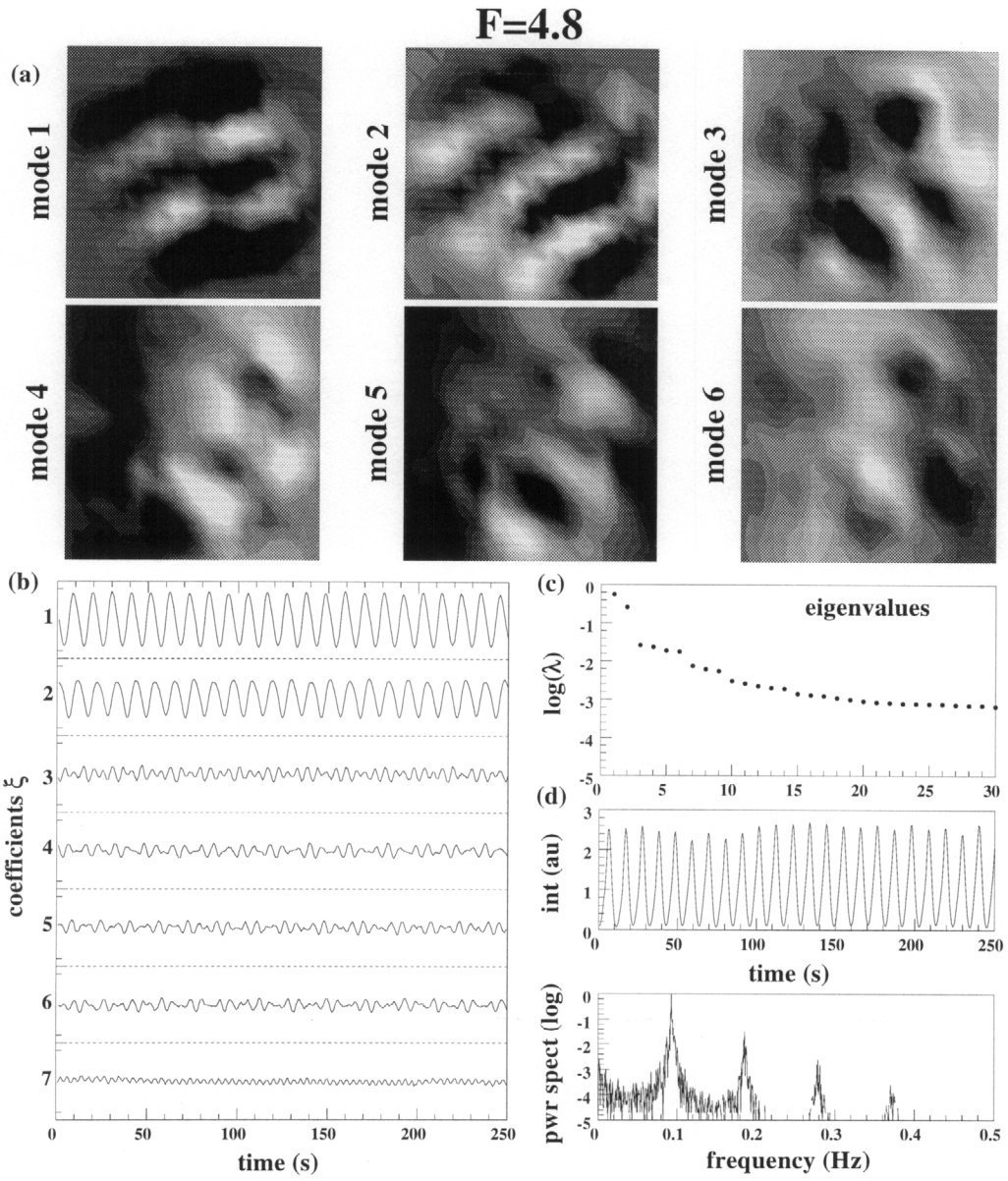

Figure 3.7: Karhunen-Loève decomposition of the resonator transverse pattern at F = 4.8 and non-zero Bragg mismatch. (a) the six most significant eigenvectors. (b) their time dependent coefficients. (c) the eigenvalue spectrum. (d) the local intensity measured at a single point in the transverse distribution and its power spectrum. Note there are now only two significant spatial modes nearly identical to the most significant mode of figure 3.6, but locked in frequency to give a periodic state.

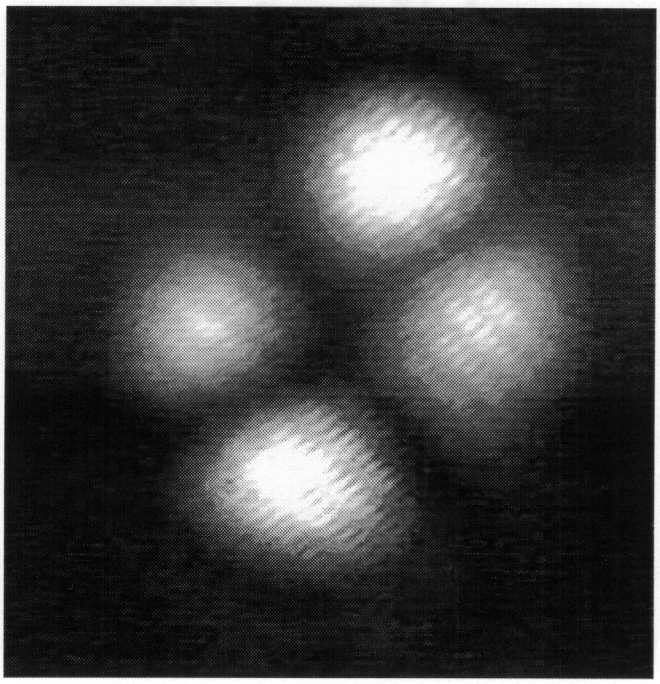

Figure 3.8: Snapshot of the state F = 4.2 and -0.40< b_x <-0.20mrad. Two defect pairs move around four regions of high intensity.

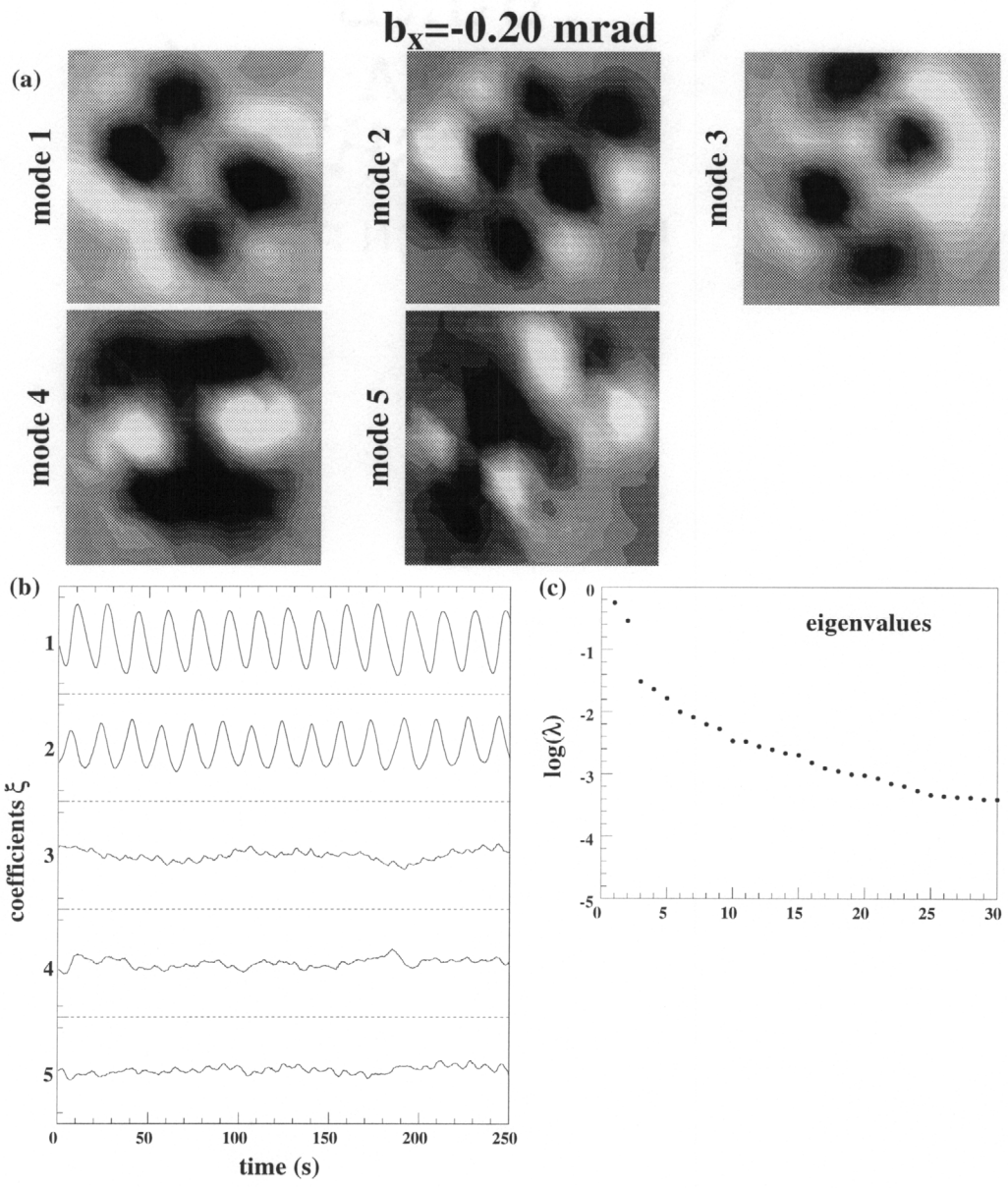

Figure 3.9: Karhunen-Loève decomposition of the resonator transverse pattern at F = 4.2 Bragg mismatch b_x = -0.20mrad. (a) the six most significant eigenvectors. (b) their time dependent coefficients. (c) the eigenvalue spectrum. The dynamics is periodic with defects moving around four regions of high intensity.

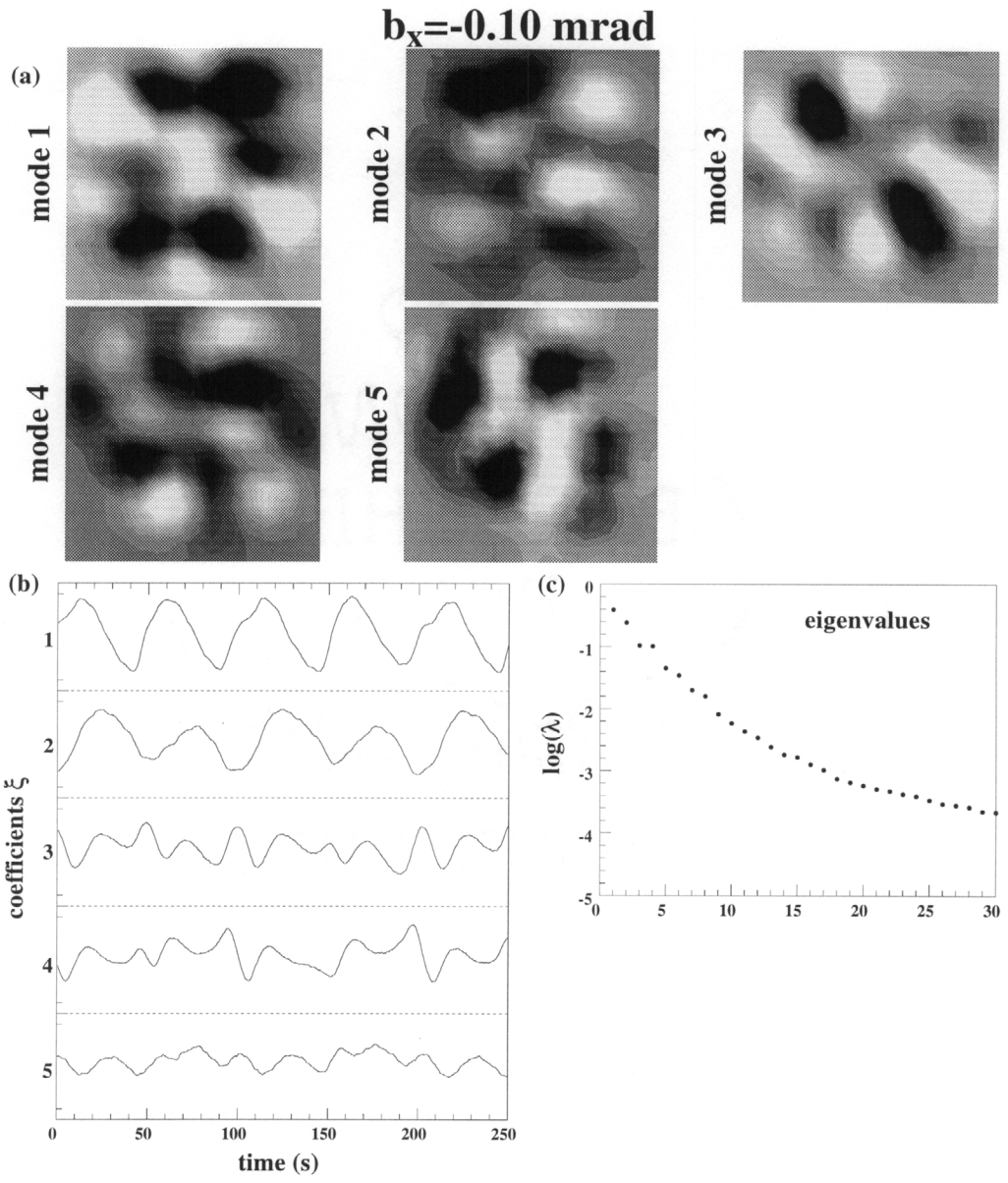

Figure 3.10: Karhunen-Loève decomposition of the resonator transverse pattern at F = 4.2 Bragg mismatch b_x = -0.10mrad. (a) the six most significant eigenvectors. (b) their time dependent coefficients. (c) the eigenvalue spectrum. This is a very slow periodic state exhibiting more rotational symmetry and susceptible to external perturbations, which leads to more irregular temporal behavior than at larger mismatch.

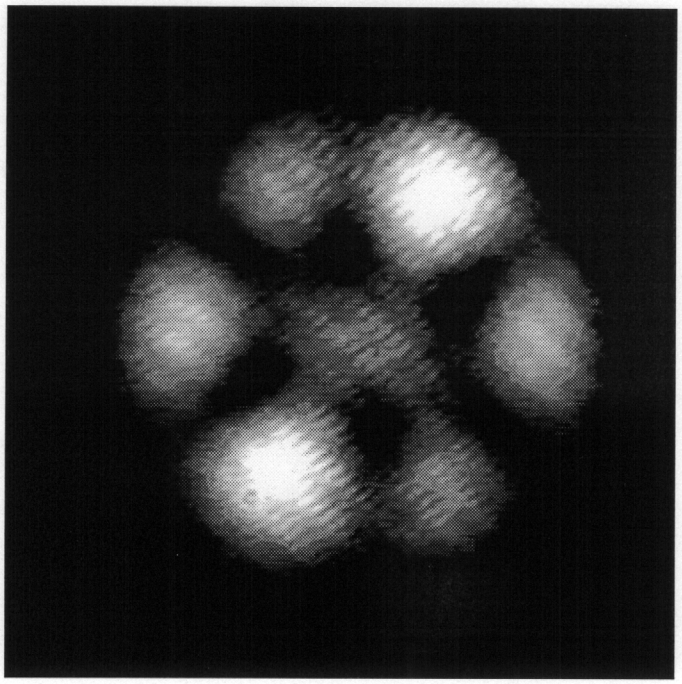

Figure 3.11: Stationary centered hexagonal pattern observed with exact phase matching at F = 4.2.

Chapter 4

Three dimensional plane wave model of the PPCR with Bragg mismatch

4.1 Introduction

So far the study of the PPCR has been limited to experimental observations and their subsequent interpretations. In this chapter we change directions and become more theoretical by modeling the dynamics starting from basic principles (i.e. the wave equation and Kukhtarev's material equations). This has already been attempted by using a truncated modal expansion of the cavity field [53], but this method was only partially successful in modeling the dynamics and could give only a qualitative description of them for moderate Fresnel number ($4.0<F<10.0$). However the work is extremely important because it pointed to the critical role played by the longitudinal component (along the cavity axis) of the Bragg mismatch. Unfortunately the approach failed to accurately predict the dynamics, particularly at low Fresnel number, because it did not include the effects resulting from the transverse component of the mismatch. As we have seen, the transverse mismatch is an essential control parameter of the PPCR because it promotes the build up of an additional phase to the phase conjugate field in the direction perpendicular to the cavity axis. This breaks the cylindrical symmetry of the system and couples the modes as was shown to be the case in the first non stationary state.

In the model developed here, the cavity field of the resonator is expanded as a sum of plane waves rather than Gauss-Hermite modes as in reference [53]. The plane wave expansion is the preferred approach because plane waves propagating in different

directions will be coupled to one another by the transverse mismatch in an intuitive and mathematically convenient manner. The method is similar to the plane wave decomposition model developed by Valley [56] to describe the spatiotemporal behavior of photorefractive backscattering and later used to describe the dynamics of double phase conjugators [57]. The assumption here is that the photorefractive four wave mixing process can be modeled in terms of a superposition of refractive index gratings. Each grating is formed by the interference of one Fourier component of the resonator cavity fields with the pump fields that are assumed to be uniform plane waves. This means that the modulation of the gratings must be small so that the higher order terms in equations 1.18 can be neglected for each grating. The formalism is adapted to our resonator geometry and both the transverse and longitudinal phase mismatch are included. Recently, other theoretical formalisms have been developed in order to explain a variety of spatial beam propagation effects in photorefractive media [58-61] and they may prove to be better suited to our system than the formalism used here. However, the present analysis is restricted to a plane wave decomposition model which, as will be seen, predicts the resonator's dynamics at low Fresnel numbers with accuracy.

The results of the numerical solutions of the model are in quantitative agreement with the dynamics experimentally observed even at low Fresnel numbers. With the aid of the model, it also becomes possible to identify the different roles played by the longitudinal and the transverse mismatches. The longitudinal mismatch is seen to promote a phase transfer along the direction of propagation between the four waves mixed in the photorefractive phase-conjugate mirror and thus destabilizes the oscillation even in the case of a single transverse mode operation. On the other hand, the transverse mismatch forces the build up of a transverse phase, resulting in a shift of the cavity field's transverse wave vector. This, together with the higher losses associated with the shift, is

responsible for the dynamical behavior observed at F≈2, as was shown experimentally in the previous chapters. A description of the theoretical model is given in the next section. Numerical results are presented in section three and compared to experimental data. Comments on the validity of the approximations made in deriving the model and on the role of the longitudinal and transverse mismatch are given in section four. A summary and concluding remarks are given in section five.

4.2 Analytical model and derivation

The scalar wave equation for non parametric photorefractive processes with negligible absorption and weakly inhomogeneous refractive index can be written as (equation 1.8)

$$\nabla^2 E(\vec{r},t) - (\varepsilon_0 \mu_0 n_b^2 + 2\varepsilon_0 \mu_0 n_b \Delta n(\vec{r},t)) \frac{\partial^2 E(\vec{r},t)}{\partial t^2} = 0, \qquad (4.1)$$

where n_b is the effective refractive index of the medium and $\Delta n(\vec{r},t)$ is the small index modulation due to the photorefractive effect. ε_0 and μ_0 are the permittivity and permeability of free space, respectively. The optical electric field in the medium is the sum of the four interacting fields:

$$E(\vec{r},t) = \tfrac{1}{2} \sum_{j=1}^{4} (A_j(\vec{r},t) e^{-i\omega t} + c.c), \qquad (4.2)$$

where the $A_j(\vec{r},t)$ are slowly varying in time.

Under the assumption that the pumps are much broader than the resonator fields and in the paraxial regime, the amplitudes of the four fields can be expanded as

$$A_j(\vec{r},t) = A_j(z,t) e^{i\vec{k}_j \cdot \vec{r}} \quad j = 1,2, \qquad (4.3)$$

for the pump fields and

$$A_3(\vec{r},t) = e^{-ikz}\sum_{m,n} a_{3mn}(z,t)\exp[ik(m\alpha x + n\beta y) + ik(m^2\alpha^2 + n^2\beta^2)\frac{z}{2}]$$

$$A_4(\vec{r},t) = e^{ikz}\sum_{m,n} a_{4mn}(z,t)\exp[-ik(m\alpha x + n\beta y) - ik(m^2\alpha^2 + n^2\beta^2)\frac{z}{2}], \qquad (4.4)$$

for the resonator fields. In the above equations m and n are integers and α and β are the angular separations of the plane waves in the transverse x and y directions. k is the magnitude of each wave vector and is equal to $2\pi/\lambda$, where λ is the wavelength measured in the medium. The resonator axis is chosen as the central direction of propagation or z axis as shown in figure 4.1.

As noted in the introduction, the refractive index modulation Δn is modeled as a superposition of the photorefractive gratings formed by the interference of each Fourier component of A_4 with A_1 and each Fourier component of A_3 with A_2. The geometry is configured so that only transmission gratings are considered. Justification for neglecting the gratings formed by the interference of pairs of Fourier components of the resonator fields is discussed in section three. With these assumptions the refractive index modulation takes the form

$$\Delta n(\vec{r},t) = \tfrac{1}{2}\sum_{pq}(\eta_{pq}(z,t)e^{i\vec{k}_{pq}\cdot\vec{r}} + c.c), \qquad (4.5)$$

where the η_{pq} are the complex amplitudes of the gratings and their wave vectors $\vec{k}_{pq}$ are given by

$$\vec{k}_{pq} = \vec{k}_1 - \vec{k}_{4pq} = \vec{k}_{3pq} - \vec{k}_2 + \vec{b}. \qquad (4.6)$$

The parameter $\vec{b} = (b_x, b_y, b_z)$ is the Bragg mismatch and is caused by an angular misalignment of the pump beams as shown in figure 4.2.

Substituting eqs. (4.2-4.5) into eq. (4.1) and separating the phase matched terms using eq. (4.6) leads to the following four field equations:

$$\frac{\partial A_1(z,t)}{\partial z} - \frac{ik}{2n_b \cos\theta} \sum_{mn} \eta_{mn}(z,t) a_{4mn}(z,t) = 0$$

$$\frac{\partial a_{4mn}(z,t)}{\partial z} - \frac{ik}{2n_b} \eta^*_{mn}(z,t) A_1(z,t) = 0$$

$$\frac{\partial A_2(z,t)}{\partial z} + \frac{ik}{2n_b \cos\theta} \sum_{mn} \eta^*_{mn}(z,t) a_{3m'n'}(z,t) e^{-ib_z z} = 0$$

$$\frac{\partial a_{3m'n'}(z,t)}{\partial z} + \frac{ik}{2n_b} \eta_{mn}(z,t) A_2(z,t) e^{ib_z z} = 0, \qquad (4.7)$$

where $m' = m + \frac{b_x}{k\alpha}$ and $n' = n + \frac{b_y}{k\beta}$ and $\theta \approx \theta_1 \approx \theta_2$ is the angle between the pumps and the cavity axis. Equations (4.7) are derived using the small angle approximation and the adiabatic approximation, where the time derivatives of the fields are eliminated due to the slow medium response. Since it is convenient to choose m' and n' as integers in the following numerical simulation, the transverse wave vector separations of the plane waves, $k\alpha$ and $k\beta$, are chosen as integral dividers of the mismatch b_x and b_y, respectively.

The equations describing the temporal evolutions of the grating amplitudes are derived by solving Kukhtarev's material equations (1.14-1.17)

$$\vec{J}(\vec{r},t) = e\mu n(\vec{r},t)\vec{E}_a(\vec{r},t) + K_B T \mu \nabla n(\vec{r},t),$$

$$\frac{\partial N_D^+(\vec{r},t)}{\partial t} = (\beta + SI(\vec{r},t))(N_D - N_D^+(\vec{r},t)) - \gamma_R n(\vec{r},t) N_D^+(\vec{r},t),$$

$$\nabla \cdot (\vec{E}_a(\vec{r},t)) = -\frac{e}{\varepsilon_0 \varepsilon}(n(\vec{r},t) + N_A - N_D^+(\vec{r},t)),$$

$$e\frac{\partial N_D^+(\vec{r},t)}{\partial t} = e\frac{\partial n(\vec{r},t)}{\partial t} - \nabla \cdot \vec{J}(\vec{r},t).$$

As described in the introduction, this system of equations is solved using a perturbative approach by treating the variables as following the forms of the individual interference terms of the intensities. Thus for this case equation 1.18 can be rewritten in the form,

$$I(\vec{r},t) = I_0 + \tfrac{1}{2}\sum_{mn}\{I_{mn}(z,t)e^{i\vec{k}_{mn}\cdot\vec{r}} + c.c.\}$$

$$n(\vec{r},t) = n_0 + \tfrac{1}{2}\sum_{mn}\{n_{mn}(z,t)e^{i\vec{k}_{mn}\cdot\vec{r}} + c.c.\}$$

$$N_D^+(\vec{r},t) = N_{D0}^+ + \tfrac{1}{2}\sum_{mn}\{N_{Dmn}^+(z,t)e^{i\vec{k}_{mn}\cdot\vec{r}} + c.c.\}$$

$$E_a(\vec{r},t) = E_0 + \tfrac{1}{2}\sum_{mn}\{E_{mn}(z,t)e^{i\vec{k}_{mn}\cdot\vec{r}} + c.c.\}. \qquad (4.8)$$

In equation 4.8 all of the coefficients of the exponential are treated as small perturbations of the spatially and temporally averaged terms with zero subscript. Following the derivation presented in the introduction and in reference [57] the equations for the grating amplitudes become

$$\frac{\partial \eta_{mn}}{\partial t}\tau_{mn} + \eta_{mn} = i\gamma_{mn}\frac{I_{mn}}{I_0}. \qquad (4.9)$$

In reference [57], it was necessary to add a "dark intensity" to the total average intensity I_0 because that intensity could vanish. In our system, the presence of the strong uniform pump beams ensures that the total intensity is large everywhere and consequently the dark intensity is neglected. The coupling constants are given by

$$\gamma_{mn} = \frac{n_b^3 r_{mn}}{2}\frac{E_{Dmn}}{1 + E_{Dmn}/E_{Qmn}} \qquad (4.10)$$

(typically this constant is written in the form $\gamma_{mn}\,\pi/\lambda$ in most of the literature),

and the characteristic time constants are given by

$$\tau_{mn} = \tau_{die}(1 + \tau_{Re}/\tau_{Dmn})(1 + E_{Dmn}/E_{Qmn})^{-1}. \qquad (4.11)$$

Furthermore,

$$I_{mn} = A_1 a^*_{4mn} + A^*_2 a_{3m'n'} e^{-ib_z z}$$

is the interference pattern creating the grating of indices m, n, and

$$I_0 = |A_1|^2 + |A_2|^2 + \sum_{mn} (|a_{3mn}|^2 + |a_{4mn}|^2)$$

is the total intensity, where the interference terms are averaged spatially. The assumption that each grating must be a small perturbation of the bulk refractive index, and thus also each of the variables in Kukhtarev's material equations, can be explicitly expressed as $I_{mn} << I_0$, which is true in practice. r_{mn} is the effective electrooptic coefficient for the grating of indices m, n, which depends on geometry, and τ_{die} is the dielectric relaxation time of the medium. The characteristic fields and diffusion times are given by

$$\tau_{Dmn} = \text{ diffusion time } \equiv \frac{e}{k_{mn}^2 K_B T \mu} \approx 10^{-9} \text{s}$$

$$E_{Dmn} = \frac{k_{mn} K_B T}{e}$$

$$E_{Qmn} = \frac{eN_A}{\varepsilon_0 \varepsilon k_{mn}}. \qquad (4.12)$$

These constants are different for each grating because of their explicit dependence on the grating vectors k_{mn}.

The boundary conditions at the entrance and exit faces of the crystal are given by $A_1(0,t)=A_1=\text{const}$, $A_2(l,t)=A_2=\text{const}$, $A_3(l,t)=0$, and using Fourier optics to describe the round trip propagation in the cavity, the field $A_4(0,t)$ entering the crystal is related to the field $A_3(0,t)$ exiting the crystal by the linear transformation [53]

$$A_4(0,\vec{r}_\perp,t) = (-Rp_2^2/\lambda^2 f^2) \int A_3(0,\vec{r}'_\perp,t)\,\text{rect}(\vec{r}'_\perp/p_1)\,\text{sinc}(p_2(\vec{r}_\perp + \vec{r}'_\perp)/\lambda f)\,d\vec{r}'_\perp, \qquad (4.13)$$

where a constant phase factor has been ignored. R is the reflection coefficient of the dielectric mirror, f is the focal length of the intracavity lens, λ is the wavelength in vacuum, and $\vec{r}_\perp$ is the transverse coordinate vector (x,y). p_1 and p_2 are the lengths of the sides of square apertures located at the phase conjugate mirror and the dielectric mirror, respectively. The rect and sinc functions are defined as in Goodman [62] and reference [53],

$$\text{i.e.} \qquad \text{rect} = \begin{cases} 1 & |x| \le \frac{1}{2} \\ 0 & \text{otherwise} \end{cases}$$

$$\text{sinc}(x) = \frac{\sin \pi x}{\pi x}.$$

Equation 4.13 is derived by operating on the exiting field $A_3(0,t)$ in the following way:

1. Truncation by the hard aperture P_1,
2. Fourier transformation by the lens, evaluated in the plane of aperture P_2,
3. Truncation by the hard aperture P_2 and reflection by the cavity mirror,
4. Fourier transformation again, evaluated in the plane of aperture P_1.

It was also assumed that the round-trip time in the cavity is much shorter than the response time of the medium. Thus in equation 4.13 the temporal lag between $a_3(t)$ and $a_4(t+2L/c)$, where L is the length of the cavity, is neglected. For numerical purpose equation 4.13 can be rewritten in its discrete form as

$$a_{4mn} = -R\pi^{-2}\text{rect}\left(\frac{k_m \lambda f}{2\pi p_2}\right)\text{rect}\left(\frac{k_n \lambda f}{2\pi p_2}\right)\sum_{pq} \Delta k_x \Delta k_y \frac{\sin(\frac{1}{2} p_1 (k_m - k_p))}{(k_m - k_p)} \frac{\sin(\frac{1}{2} p_1 (k_m - k_q))}{(k_m - k_q)} a_{3pq}, \tag{4.14}$$

where the integral spacing is taken to be the same as the plane wave spacing so that $\Delta k_x = k\alpha$, $\Delta k_y = k\beta$, $k_m = \Delta k_x m$, and $k_n = \Delta k_x n$. The rect functions of equation 4.14 are

represent the sharp spatial frequency cutoff due to the aperture p_2 located at the dielectric mirror.

4.3 Results

The field equations (4.7) and the grating equations (4.9) together with the boundary conditions were solved using the method described in ref. [63]. A second order Runge-Kutta algorithm was used for the temporal integration and a fourth order for the spatial integrations. This is also known as the time split-step method in which the field equations are integrated at both the full and half time steps of the grating equations. The results were checked by decreasing the step sizes until changes in the solutions were smaller than 1%. Time was normalized to $\tau_{mn} \approx \tau_{00}$ (see below for justification) which is approximately 1s for intensities on the order of $4W/cm^2$ in $BaTiO_2$. The longitudinal direction (z) was normalized to the interaction length l in the crystal and intensities were normalized to the total incident pump intensity $|A_1|^2 + |A_2|^2$, which is about 70mW with a beam diameter of 3mm in the experiment. Parameter values were chosen to be compatible with experimental conditions: $|A_1(0,t)|^2 = |A_2(l,t)|^2 = 0.5$, R = 0.95, l = 0.5cm, and $\gamma_{mn} l \approx \gamma_{00} l = 5.0 \times 10^{-4}$cm. The coupling parameter and response time were assumed constant for all grating components since the angular cutoff of the resonator for Fresnel numbers of interest, 0<F<10, is very small (on the order of 1° so that $|k_{mn}| \approx |k_{00}|$). The two control parameters were the Fresnel number ($F = p_1 p_2 / \lambda f$) and the off-Bragg parameter $\vec{b}$. For the calculations presented in figures 4.3 and 4.5, F=2.0 and b_y was varied with b_x set to zero while, as dictated by the geometry, $b_z \approx b_y/10$. For these values of the control parameters the cavity fields were sampled on a 3 by 17 lattice in wave vector space. In all calculations each component was built up from a small seed

$\mathrm{Re}\{a_{4mn}(0,0)\} = \mathrm{Im}\{a_{4mn}(0,0)\} = 10^{-5}$ corresponding to the initial light scattered in the direction of the cavity when the pumps are turned on in the experiment.

The simulation was carried out for different values of the control parameters and the results agree well with experimental observations. For small F (F<2.0) only homogeneous stationary states are achieved. As F is increased and for no mismatch, the dynamics remains stationary and the transverse patterns have a corresponding increase in structure. As both F and the mismatch increase, the system exhibits a wide variety of dynamical behaviors which include periodic states, period doubling and aperiodic states as observed experimentally [35,36].

At F≈2.0 the truncated modal decomposition described in previous work [53], and which did not include the transverse mismatch, was unable to accurately model the dynamics observed experimentally. The plane wave model developed in this chapter with the vectorial mismatch included does however, as shown in figure 4.3. Figure 4.3a is the same as figure 2.2 and shows a typical experimental sequence of snapshots of this state when there is a vertical mismatch. Figure 4.3b shows the results of the simulation under the same conditions. Keeping in mind that these figures show only the intensity of the field and not the field itself, the correct periodic sequence of vortices nucleation and repulsion is appears be produced by the simulation.

Figure 4.4 was constructed in order to check that the complex field amplitude obtained from the simulation does accurately model the real field in both amplitude and phase. The intensity (or just the amplitude squared) patterns of figure 4.3 cannot show that the dark areas are actually vortices because they contain no phase information about the field. Figure 4.4 shows a snapshot interferogram obtained by interfering the field, reconstructed from a discrete set of Fourier components included in the simulation, with a tilted reference plane wave. To generate this interferogram, the transverse Bragg

mismatch was set at 45 degrees from the square boundaries of the system. The position of the two singularities are revealed by dislocations in the interference fringes as indicated by the two arrows in the figure, thus demonstrating the accuracy of the model.

The reason for choosing a Bragg mismatch at an angle with respect to the transverse boundaries is to be able to identify the singularities as two localized screw dislocations with opposite signs. If the Bragg angle is chosen parallel to a side of the square boundaries of the system, the simulation leads to a situation where the two lines Re{E}=0 and Im{E}=0 (where E is the cavity optical field and Re, Im are its real and imaginary part, respectively), are also parallel to that boundary. As time evolves, the two parallel lines move toward each other. When they cross, an edge dislocation is created that disappears instantly, leaving no time to observe localized point dislocations. When the Bragg mismatch is not parallel to the boundary, the lines Re{E}=Im{E}=0 are curved and cross at two localized points where the dislocations are located. These dislocations appear at the center of the pattern and move toward the boundary along a line normal to the transverse Bragg mismatch, exactly as observed experimentally. The peculiarity observed in the simulation is an artifact produced by the choice of transverse square boundaries for the cavity and the decomposition in plane waves along these directions. It does not appear in the experiment where circular apertures are used to confine the transverse dimension of the cavity (see figure 2.1).

Figure 4.5 shows the frequency of the periodic state versus the amount of mismatch. For the experiment (figure 4.5a) the measured mismatch is approximately given by the expression $n_b(\theta_1 - \theta_2)$, which is the amount of angular misalignment between the pumps measured outside the crystal (see figure 4.2). In the experiment, the angle was varied in one transverse direction by tilting a mirror, while a constant mismatch was maintained in the perpendicular direction in order to avoid the very slow dynamics

near $|\vec{b}| = 0$. For the simulation (figure 4.5b) the mismatch is given by the expression $n_b(\sin\theta_1 - \sin\theta_2)$. A best-fit curve to the simulation data shows that the frequency is nearly proportional to the square of the mismatch as defined.

4.4 Comments

Although the model described in the previous section predicts accurately the observed dynamics, a number of assumptions were made in its derivation that need some clarification and justification. The standard approximations of negligible absorption, slowly varying envelopes, paraxial fields, and adiabatic elimination of the time derivatives in the field equations need no commentary (see for example [22], [53]. and [57]). A less obvious approximation is the assumption that the coupling coefficients γ_{mn} and characteristic time scales τ_{mn} in all the grating amplitude equations are equal. In reality these parameters depend on the magnitude and orientation with respect to the crystal axis of the grating wave vectors associated with them, and the effective electrooptic coefficient in accordance with equations 4.10 and 4.11. In our system however, the angular spread of the cavity beam will only reach values on the order of one degree outside the crystal even for Fresnel numbers as large as 100. Such angular variations would change the grating wave vectors and the effective electrooptic coefficient by less than one percent. This will reflect in a similar change in the coupling coefficients and characteristic scales thereby justifying the approximation.

The other major assumption was that the mixing between pairs of plane waves components could be neglected in the determination of the index modulation. Since the cavity field is expanded in terms of plane waves, each pair should create its own grating via two wave mixing. The effect by itself is known to be responsible for beam fanning

[64], double phase conjugation [57] and the formation of photorefractive solitons [15]. However, in our four wave mixing geometry these effects can be ignored because the gratings formed by the strong pumps and the cavity fields erase and suppress the formation of other gratings, a behavior which was verified experimentally.

An important feature of the model is the identification of the separate roles played by the longitudinal and the transverse mismatch components. At small Fresnel numbers, the transverse component is primarily responsible for the non stationary behavior. This was confirmed by calculations made with the longitudinal component of the mismatch set to zero, which give results identical to those shown in figures 4.3-4.5. This behavior occurs because the transverse mismatch adds a transverse linear phase to each Fourier component a_{4mn}, so that the corresponding Fourier component a_{3mn} of the "phase conjugate" beam acquires a tilt. This tilt is compounded by the inversion in the cavity and therefore builds up. However the cavity losses increase for components traveling at increasing angles with respect to its axis. The dynamic balance between the tilt, which is driven by the transverse mismatch, and the cavity losses results in the periodic behavior observed at low Fresnel number.

At higher Fresnel numbers, the role of the longitudinal component of the mismatch becomes apparent. When it is set to zero in the model only stationary or periodic solutions are found, despite the inherent nonlinearity of the system due to the inclusion of pump depletion. For $F \approx 4.0$, inclusion of the longitudinal mismatch in the model is necessary in order to obtain aperiodic and chaotic states such as those observed in experiments [53,36]. This behavior occurs because the longitudinal component of the mismatch causes a phase lag between the gratings and the field components forming them, thus causing a phase transfer between the beams. The effect is similar to the creation of a complex coupling constant, which in other known systems occurs either

because of the presence of a photovoltaic field in the medium or the application of an external electric field. Work by other groups has shown that a complex coupling constant is a necessary condition leading to the occurrence of complex dynamics in photorefractive media [60,65] even in the case of a single mode.

4.5 Summary and conclusion

In this chapter a model of the photorefractive phase-conjugate resonator with Bragg mismatch has been developed and was demonstrated to give an accurate representation of the dynamics observed experimentally. The different roles played by the transverse and the longitudinal mismatch in two different ranges of Fresnel number values have been described, understood and checked against experimental observation. We have also given some insight into the effects of the boundary conditions on the creation of dislocations in the cavity field and their relation to the transverse mismatch. It appears that with square apertures at $F \approx 2.0$, a mismatch parallel to the edge of the apertures will lead to the creation of edge dislocations, while a mismatch at some angle to the edges will produce mixed screw/edge dislocations. It is expected that the circular apertures used in the laboratory are responsible for the observed pure screw dislocations.

Unfortunately the model was not solved for larger Fresnel numbers because of restrictions on our computational budget. This is an error due to the disk operating system in which the simulation was performed because it does not allow easy access to the entire memory of the hardware. A modification of the program code to access all of the hardware memory or the use of another operating system would fix this problem.

It is also an unfortunate artifact of the model that very small mismatches cannot be tested. Because the plane waves are coupled by the mismatch, it was necessary to

make the plane wave spacing equal to the size of the mismatch. Therefore as the mismatch goes to zero the number of plane waves needed to represent the cavity field diverges. Fortunately this is not a problem at zero mismatch since the waves decouple and consequently the simulation can be performed by simply using enough plane waves to ensure the field is not under sampled.

In the future this problem may be averted if a slightly different approach is taken in the derivation of the model. One could use the orthogonality of the plane waves to decouple the fields in the wave equation instead of simply using phase matching. This would lead to a coupling overlap integral due to the added transverse phase factor of the mismatch. In this way any suitable basis set could be used (not just plane waves) and perhaps even the truncated Gauss-Hermite modal decomposition of reference [53] would correctly model the system.

Despite these problems this model was extremely useful in understanding the PPCR. It establishes the necessary assumptions needed to accurately depict the dynamics experimentally observed in the system. It also demonstrates the critical importance of the transverse mismatch as it applies to symmetry breaking and dynamical states.

Although the details of the model are unimportant to describe qualitatively the dynamics at large Fresnel numbers, an accurate model is needed to obtain a quantitative agreement between numerical simulations and experimental data at low Fresnel numbers. The different roles played by the transverse and the longitudinal mismatch in these two different ranges of Fresnel number values has also been discussed. It is hoped that an understanding of the roles played by the various parameters of the system in the resonator's dynamical behavior may lead to some insights into the possible means of controlling the system. This understanding is critical if practical uses, such as in image storage and associative recall, are to be found for photorefractive resonators.

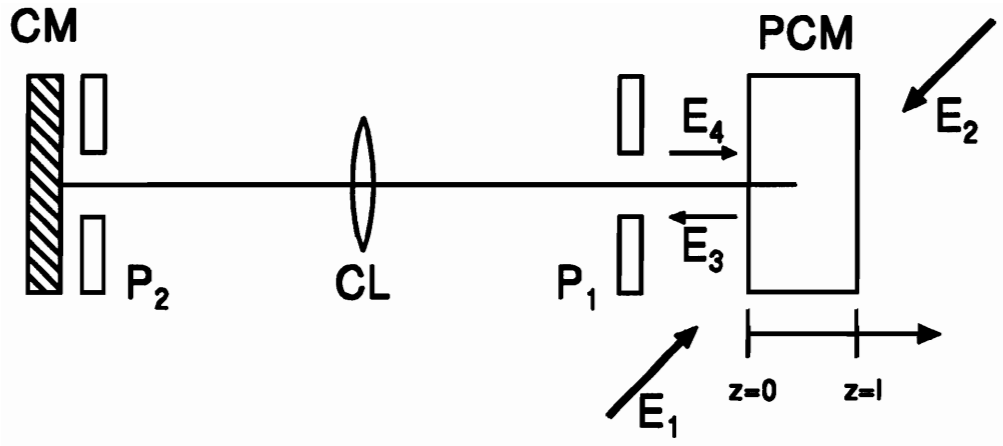

Figure 4.1: Photorefractive phase-conjugate confocal resonator. P_1, P_2: circular apertures (diameters ~0.43mm). CL: cavity lens (focal length 16cm) placed one focal length from P_1 and P_2. CM: planar, 95% reflecting dielectric mirror. PCM: phase-conjugate mirror ($BaTiO_3$ crystal in four-wave mixing geometry with external pumps E_1, E_2).

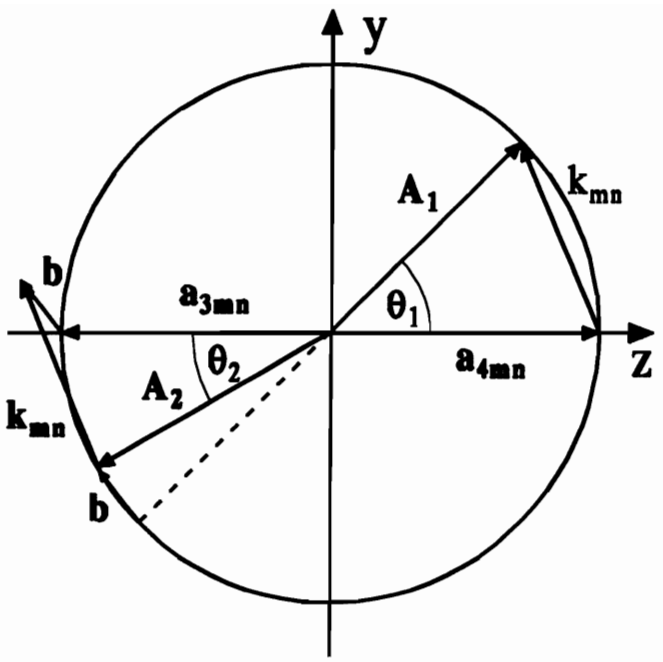

Figure 4.2: Wave mixing geometry with slightly tilted pump beams in order to introduce a Bragg mismatch. $\vec{b}$: wave vector mismatch (the mismatch equals $n_b(\sin\theta_1 - \sin\theta_2)$ where the angles are measured outside the crystal).

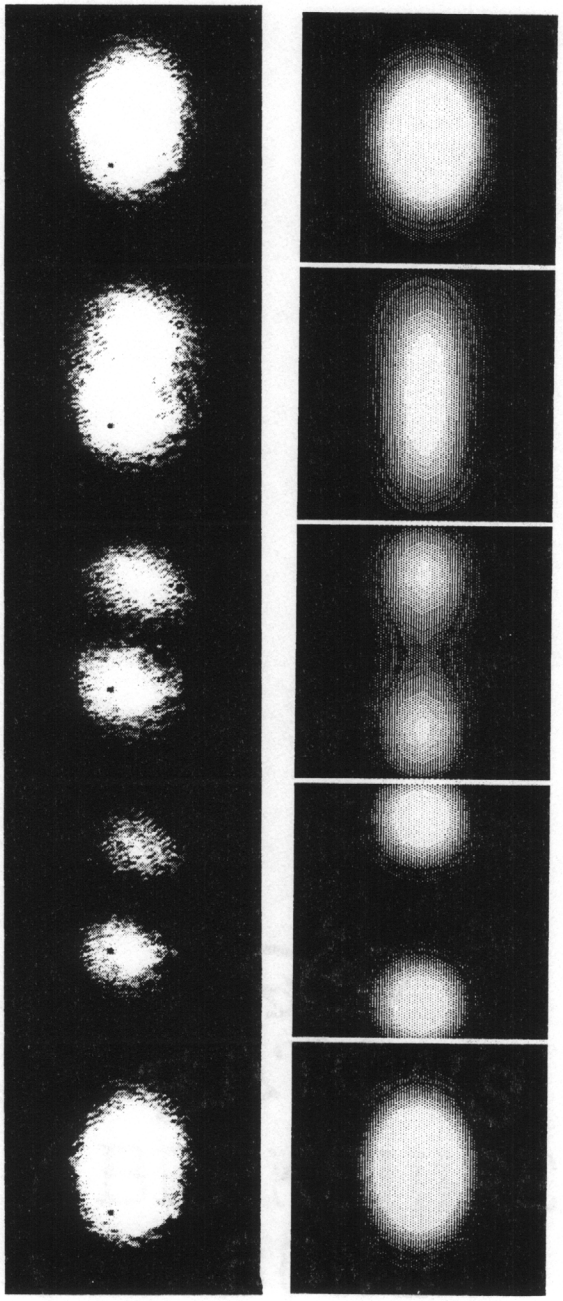

(a) (b)

Figure 4.3: Sequence of snapshots of the transverse intensity distribution at aperture P_1 for the periodic state at F≈2.0. The mismatch is in the vertical direction leading to the motion of a pair of defects along the horizontal direction: (a) experiment, (b) numerical simulation. The snapshots are reconstructed from an array of 3x17 Fourier components.

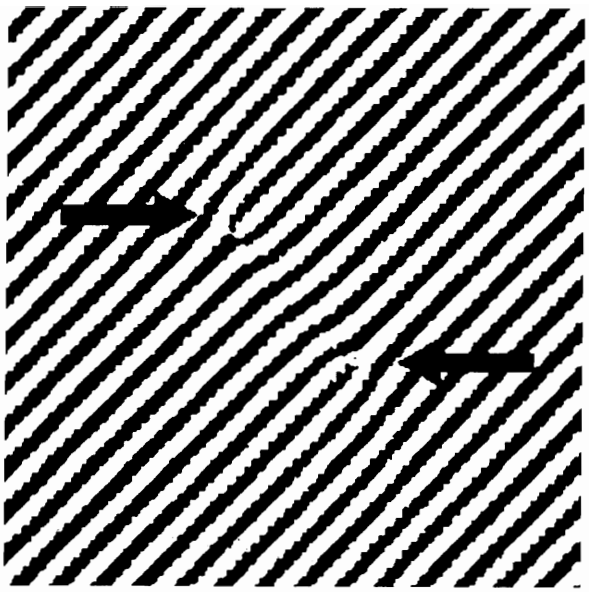

Figure 4.4: Simulated snapshot interferogram of the field reconstructed from the 3x17 Fourier components with a tilted reference plane wave. The mismatch is at 45° from the boundary (see text for details) and the two singularities are identified by arrows.

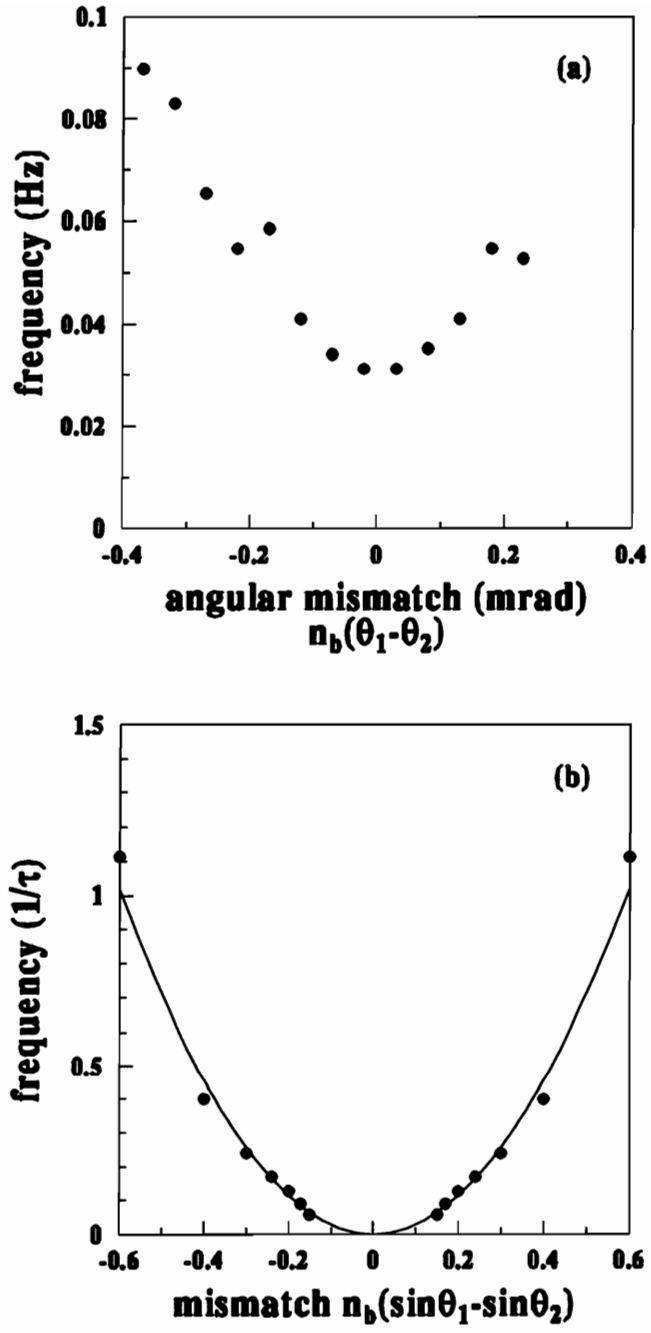

Figure 4.5: Frequency of the periodic state versus mismatch at F≈2.0. (a) experiment, where the vertical mismatch is varied for a fixed non zero horizontal mismatch, (b) numerical simulation where the vertical mismatch is varied for a zero horizontal mismatch (the definition of the angles refer to figure 4.2).

Chapter 5

Conclusion

5.1 Summary and Discussion

The work presented in this dissertation is the result of an investigation into the spatiotemporal dynamics of a photorefractive phase-conjugate resonator (PPCR). The study was motivated by the PPCR's special attributes in the general field of transverse nonlinear optical systems. It exhibits relatively slow dynamics compared to similar systems in the field which are usually only theoretically studied because of their high speed dynamics (e.g. lasers). Therefore the PPCR provides a means for characterizing the generic dynamics of these systems using convenient and accessible experimental methods. In addition, this work is motivated by the specific properties of a PPCR which could possibly make it ideal for use in optical image processing and storage devices. To this end, chapters two and three of this dissertation presented the validation of two novel experimental techniques, a holographic correlator and the Karhunen-Loève decomposition, for use in characterizing the dynamics of transverse optical systems. The results of the application of these two techniques to the PPCR were also presented. The culmination of the investigation was the development of an analytical model of the PPCR in terms of the fundamental equations governing photorefractive phenomena and is presented in chapter four. In this section we give a brief review of the dissertation and highlight its major results.

First, the PPCRs control parameters were identified and their effects on the system dynamics were initially characterized. The first parameter is the cavity Fresnel number

which is a measure of the transverse confinement of the cavity and has the effect of increasing the spatial and temporal complexity of the dynamics as it is increased. The other parameter is the Bragg mismatch which breaks the cylindrical symmetry of the cavity and increases the speed of the dynamics as it is increased. It was demonstrated that for the first non stationary state at F≈2.0 the mismatch caused the periodic nucleation and repulsion of optical defects in the direction perpendicular to the direction of the transverse mismatch. As the mismatch was decreased the frequency of the nucleation and repulsion decreased until a spatially uniform, stationary state was observed at no mismatch.

In order to gain some initial insight into the system this first non stationary state was modeled in terms of the superposition of a few spatial patterns (also termed modes) that compete for the gain in the photorefractive medium. The model was developed by considering the mathematical description of a field containing two defects exhibiting the periodic behavior observed experimentally. It was tested using a holographic correlator that optically measures the correlation between the spatial patterns in the cavity field and individual spatial patterns stored in holograms that were matched to the patterns in the model. The results of the experiment confirmed the validity of the model by detecting directly the presence of the presumed patterns in the cavity beam and measuring their individual temporal behavior.

The interpretation of the model in terms of the control parameters of the system is as follows. At very low Fresnel numbers only a fundamental Gauss-Laguerre mode can be sustained by the cavity of the system. At F≈2.0, since the mismatch adds an additional transverse phase to the fundamental mode after each round trip, it excites modes with more structure. The direction of the mismatch is responsible for the broken symmetry of the system and dictates the form of the asymmetric mode. Due to the cavity confinement

however, diffraction losses are larger for these excited modes and it is the interplay between these losses and the mismatch that leads to the observed dynamics.

In terms of the effectiveness of the correlator technique, it was demonstrated to work very well for the relatively simple dynamics of this state, because it can be modeled in terms of the superposition of a very small number of modes. It is an ideal method for use on much faster systems because each hologram requires only a single detector, which can have very fast response times. Unfortunately the technique loses its utility at larger Fresnel numbers because of the more complicated spatial dynamics. More complex patterns require a large number of modes for their representation and consequently the number of holograms and their complexity must increase. While it was a simple matter to create holograms corresponding to simple orthogonal patterns in order to test the model at low Fresnel number, complicated holograms would be more difficult to create. Not only does the number of holograms and their different complexities lead to practical problems in terms of their production, it will also lead to problems in terms of their implementation and interpretation of experimental results. It would be difficult to create the many perfectly orthogonal holograms required, and this lack of orthogonality would eventually lead to spurious correlation data.

Another experimental technique was applied to the system partly in order to address the complications of the correlator and also to further investigate the dynamics of the PPCR using an independent method. The technique, known as the Karhunen-Loève decomposition, is a method that decomposes the cavity field into orthogonal spatial patterns called active cavity modes. The patterns are the eigenvectors of the covariance matrix. The implementation of this method involves the collection of a sequence of images of the transverse intensity profile of the cavity field and then processing them using the Karhunen-Loève algorithm. The method was shown to be an effective tool for

studying the systems spatiotemporal dynamics as was demonstrated by its application to the first non stationary state. The results of the Karhunen-Loève analysis support the aforementioned model and agree with the results obtained by the correlator technique. For this first non stationary state, two modes were revealed to oscillate in the cavity. The first was interpreted as the fundamental Gauss-Laguerre mode of the modal decomposition model and the second as the combination of the two excited modes of the model- a Gauss-Laguerre (10) and a Gauss-Hermite (01).

The application of this technique at larger Fresnel numbers revealed important information on the number and spatial structure of active modes oscillating in the cavity, which would be difficult to obtain by other means. It provided evidence for the inverse relationship between the size of the Bragg mismatch and the level of cylindrical symmetry of the patterns emitted by the system. It also showed the interesting feature that states exhibiting periodic behavior can share the same modal structure as aperiodic states, despite their vastly different temporal behavior.

The drawback of the Karhunen-Loève decomposition is that it is based on the diagonalization of the covariance matrix of the intensity fluctuations and therefore does not contain information of the phase of the modal structure. This is less of a problem in laser systems since a laser cavity has a complete set of empty cavity modes that give insight into the active cavity behavior. Unfortunately, its application to laser dynamics is difficult because of the short time scales involved. The method is computer intensive and requires the use of a CCD array, which slows down the data acquisition process. Recent technological advances may eventually eliminate these problems. CCD arrays operating in the Megabytes/sec range are now commercially available. This is just at the lower limit typical phenomena observed in laser systems.

In the third part of this thesis, chapter 4, an accurate analytical model of the system was developed for the first time. The model is based on a plane wave expansion of the cavity field and the variables in Kukhtarev's material equations and includes the vector Bragg mismatch. A similar model including only the longitudinal mismatch has been studied, but did not accurately depict the observed dynamics. The results of the complete model shows that the transverse component of the Bragg mismatch couples some of the plane waves traveling in different directions because they must share the same refractive index gratings. The numerical solution of this model matched accurately the experimental observations. Stationary states were observed only with no mismatch and arbitrary Fresnel numbers, or at very low Fresnel numbers and arbitrary mismatch. For a finite mismatch, as the Fresnel number is increased the periodic states, period doubling, and aperiodic states experimentally observed were simulated.

In the derivation of the model key assumptions were identified. Inclusion of two wave mixing between pairs of plane waves and the angular dependence of the coupling and temporal coefficients of the plane waves were shown to be unnecessary. These two factors would have severely complicated a numerical simulation. Also it showed the necessity of the inclusion of pump depletion. With this model, it became feasible to identify the roles played by the directional components of the vector mismatch. The longitudinal mismatch was shown to lead to a complex coupling constant which in turn destabilizes periodic states. The transverse mismatch was shown to break the cylindrical symmetry of the system and thus to destabalize stationary states. In the case of a mode competition model, the transverse mismatch is responsible for coupling the modes together.

The model also gave some insight into the effects of the boundary on the formation of defects. It appears that the shape of the apertures in the system and the

direction of the mismatch determine the type of dislocation (screw or edge) created in the cavity field. Experimental observations with circular apertures yield pure screw dislocations, while using square apertures in the model lead to edge and mixed screw/edge types.

5.2 Recommendations for future work

In conclusion, this work has demonstrated the value of two novel experimental techniques that can be used to study transverse nonlinear optical systems, namely a holographic correlator and the Karhunen-Loève decomposition. More importantly, the application of these techniques to the PPCR and the development of an accurate analytical model, have led to a better understanding of the underlying physics governing its dynamics. It is hoped that this understanding will lead to its possible control and practical implementation in, for example, image processing systems.

As it stands now, the analytical model requires some more tests and, despite its accuracy, can perhaps be modified to ease the computational effort involved in its solution. First, the model needs to be solved for a broader range of parameter values at larger Fresnel numbers before we can be sure that it is complete. Also absorption, which has been shown to modify other temporal effects in photorefractive media [65], has so far been ignored. Its effect in the PPCR should be determined. Lastly, the model could possibly be redeveloped using coupling integrals created by the mismatch, rather than the simple shared-grating approach employed here. This could greatly reduce the complexity involved in the numerical solutions and even possibly lead to analytical solutions.

Another parameter affecting the dynamics of the system is the geometry of the cavity. Thus far no systematic investigation has been performed on effects related to the

cavity geometry, either in terms of defect formation or spatiotemporal dynamics in general. In the course of this investigation the cavity was modified using two lenses in a 4f arrangement so that the field was not inverted after a cavity round-trip. Preliminary results show that the dynamics becomes much quieter even as the Bragg mismatch is changed. This could be crucial in practical applications where, in general, non stationary states are considered to be a hindrance.

References

1. T. H. Maiman, Nature 187, 493 (1960).
2. P. A. Franken, A. E. Hill, C. W. Peters, and G. Weinreich, Phys. Rev. Lett. 7, 118 (1961).
3. W. Kaiser and C. G. B. Garret, Phys. Rev. Lett. 7, 229 (1961).
4. J. A. Armstrong, N. Bloembergen, J. Ducuing, and P. S. Pershan, Phys. Rev. 127, 1918 (1962).
5. D. A. Kleinman, Phys. Rev. 126, 1977 (1962).
6. W. W. Rigrod, Appl. Phys. Lett. 2, 51 (1963).
7. J. P. Goldsborough, Appl. Opt. 3, 267 (1964).
8. V. E. Zakharov and A. B. Shabat, Soviet Phys. JETP 34, 62 (1972).
9. J. E. Bjorkholm and A. Ashkin, Phys. Rev. Lett. 32, 129 (1974).
10. N. B. Abraham and W. J. Firth, J. Opt. Soc. Am. B 7, 951 (1990).
11. L. A. Lugiato, Chaos, Solitons, and Fractals 4, 1251 (1994).
12. H. Haken, Phys. Lett. 53A, 77 (1975).
13. C. O. Weiss, A. Godone, and A. Olafsson, Phys. Rev. A 28, 892 (1983).
14. U. Efron ed., *Spatial Light Modulator Technology* (Marcel Dekker, Inc., NY, 1995).
15. M. Segev, B. Crosignani, A. Yariv, and B. Fischer, Phys. Rev. Lett. 68, 923 (1992).
16. D. Z. Anderson, Opt. Lett. 11, 56 (1986).
17. L. A. Brambilla, L. A. Lugiato, M. B. Pinna, F. Prati, P. Pagani, P. Vanotti, M. Y. Li, and C. O. Weiss, Opt. Commun. 92, 145 (1992).

18. M. Cronin-Golomb, B. Fischer, J. O. White and A. Yariv, IEEE J. Quantum Electron. QE-20, 12 (1984).

19. A. Ashkin, G. D. Boyd, J. M. Dziedzic, R. G. Smith, A. A. Ballman, J. J. Levinstein, and K. Nassau, Appl. Phys. Lett. 9, 72 (1966).

20. F. S. Chen, J. Appl. Phys. 38, 3418 (1967).

21. F. S. Chen, J. T. LaMacchia, D. B. Fraser, Appl. Phys. Lett. 13, 223 (1968).

22. A. Yariv, *Optoelectronics* (Holt Rinehart and Winston, Inc. 1991).

23. A. Yariv, Opt. Commun. 25, 23 (1978).

24. J. Feinberg, D. Heiman, A. R. Tanguay Jr., and R. W. Hellwarth, J. Appl. Phys. 51, 1297 (1980).

25. N. V. Kukhtarev, V. B. Markov, S. G. Odulov, M. S. Soskin, and V. L. Vinetskii, Ferroelectrics 22, 949 (1979).

26. P. Yeh, *Introduction to Photorefractive Nonlinear Optics* (John Wiley and Sons, NY, 1993).

27. H. Kogelnik, Bell. Syst. Tech. J. 48, 2909 (1969).

28. R. W. Boyd, *Nonlinear Optics* (Academic Press, Inc., San Diego, CA, 1992).

29. P. Günter and J. P. Huignard, *Photorefractive Materials and Their Applications I and II* (Springer-Verlag, 1988).

30. B. Y. Zeldovich, V. L. Popovichev, B. B. Ragulskii, and F. S. Faisullov, Sov. Phys. 15, 109 (1972).

31. A. Yariv and D. M. Pepper, Opt. Lett. 1, 16 (1977).

32. J. P. Huignard, J. P. Herriau, P. Aubourg, and E. Spitz, Opt. Lett. 4, 21 (1979).

33. M. Cronin-Golomb, B. Fischer, J. Nilsen, J. O. White, and A. Yariv, Appl. Phys. Lett. 41, 219 (1982).

34. G. Indebetouw and S. R. Liu, Opt. Commun. 91, 321 (1992).

35. S. R. Liu and G. Indebetouw, J. Opt. Soc. Am. B 9, 1507 (1992).

36. D. R. Korwan and G. Indebetouw, "Experimental modal analysis of the spatiotemporal dynamics of a linear photorefractive phase-conjugate resonator," (accepted by J. Opt. Soc. Am. B 1995).

37. F. T. Arecchi, S. Boccaletti, P. L. Ramazza, and S. Residori, Phys. Rev. Lett. 70, 2277 (1993).

38. C. Denz, J. Goltz, and T. Tschudi, Opt. Commun. 72, 129 (1989).

39. K. D. Shaw, Opt. Commun. 97, 148 (1993).

40. L. E. Adams and R. S. Bondurant, Opt. Lett. 18, 226 (1993).

41. G. J. Dunning, S. W. McCahon, M. B. Klein, and D. M. Pepper, J. Opt. Soc. Am. B 11, 339 (1994).

42. L. A. Lugiato, C. Oldano, and L. M. Narducci, J. Opt. Soc. Am. B 5, 879 (1988).

43. M. Brambilla, M. Cattaneo, L. A. Lugiato, R. Pirovano, F. Prati, A. J. Kent, G. L. Oppo, A. B. Coates, C. O. Weiss, C. Green, E. J. D'Angelo, and J. R. Tredicce, Phys. Rev. A 49, 1427 (1994).

44. J. F. Nye and M. V. Berry, Proc. R. Soc. Lond. A. 336, 165 (1974).

45. F. T. Arecchi, G. Giacomelli, P. L. Ramazza, and S. Residori, Phys. Rev. Lett. 65, 2531 (1990).

46. S. R. Liu, *Spatiotemporal Behavior and Nonlinear Dynamics in a Phase Conjugate Resonator* (Ph. D. dissertation, Virginia Tech 1993).

47. D. R. Korwan and G. Indebetouw, Opt. Commun. 119, 305 (1995).

48. C. Green, G. B. Mindlin, E. J. D'Angelo, H. G. Solari, and J. R. Tredicce, Phys. Rev. Lett. 65, 3124 (1990).

49. F. T. Arecchi, S. Boccaletti, G. B. Mindlin, and C. P. Garcia, Phys. Rev. Lett. 69, 3723 (1992).

50. D. Hennequin, L. Dambly, D. Dangoisse, and P. Glorieux, J. Opt. Soc. Am. B 11, 676 (1994).

51. L. A. Lugiato and C. O. Weiss, Phys. Rep. 219, 293 (1992).

52. G. D'Alessandro, Phys. Rev. A 46, 2791 (1992).

53. S. R. Liu and G. Indebetouw, Opt. Commun. 101, 442 (1993).

54. S. Watanabe, *Pattern Recognition* (John Wiley and Sons, NY, 1985).

55. A. Fuchs, J. A. S. Kelso, and H. Haken, Int. J. Bifurcation and Chaos 2, 917 (1992).

56. G. C. Valley, J. Opt. Soc. Am. B 9, 1440 (1992).

57. D. Engin, M. Segev, S. Orlov, A. Yariv and G. C. Valley, J. Opt. Soc. Am. B 11, 1708 (1994).

58. M. Cronin-Golomb, Optics Comm. 89 (1992) 276; M. Cronin-Golomb, Optics Lett. 20, 2075 (1995).

59. A. A. Zozulya, M. Saffman and D. Z. Anderson, Phys. Rev. Lett. 73, 818 (1994).

60. M. R. Belic, J. Leonardy, D. Timotijevic and F. Kaiser, J. Opt. Soc. Am. B 12, 1602 (1995).

61. K. D. Shaw, Optics Lett. 20, 1610 (1995).

62. J. W. Goodman, *Introduction to Fourier Optics* (McGraw-Hill, USA, 1988).

63. V. Kalinin and L. Solymar, Appl. Phys B 45, 129 (1988).

64. M. Segev, Y. Ophir and B. Fischer, Optics Comm. 77, 265 (1990).

65. W. Krolikowski, M. R. Belic, M. Cronin-Golomb and A. Bledowski, J. Opt. Soc. Am. B 7, 1204 (1990).

VITA

Daniel Richard Korwan was born in Long Island, New York on July 19, 1966. He is the son of William S. Korwan and Elaine L. Korwan and has four siblings, William C., Janet S., David J. and Annette M.

He graduated from Warwick Valley High School in Warwick, New York in 1984 and entered the University of Rochester in the fall of the same year. After graduating from Rochester in 1988 with a BS degree in Optics, he enrolled in the Virginia Tech Department of Physics. He received his MS in Physics in 1991 and Ph.D. in Physics in 1996.